AD-A054 464 BENDIX CORP SOUTH BEND IND ENERGY CONTROLS DIV F/G 21/5
FLUIDIC PRESSURE RATIO SENSOR.(U)
FEB 78 D C THOMAN, J M EASTMAN F33615-74-C-2068
UNCLASSIFIED ECD-866-19292-R AFAPL-TR-78-7 NL

| OF |
AD
A054464

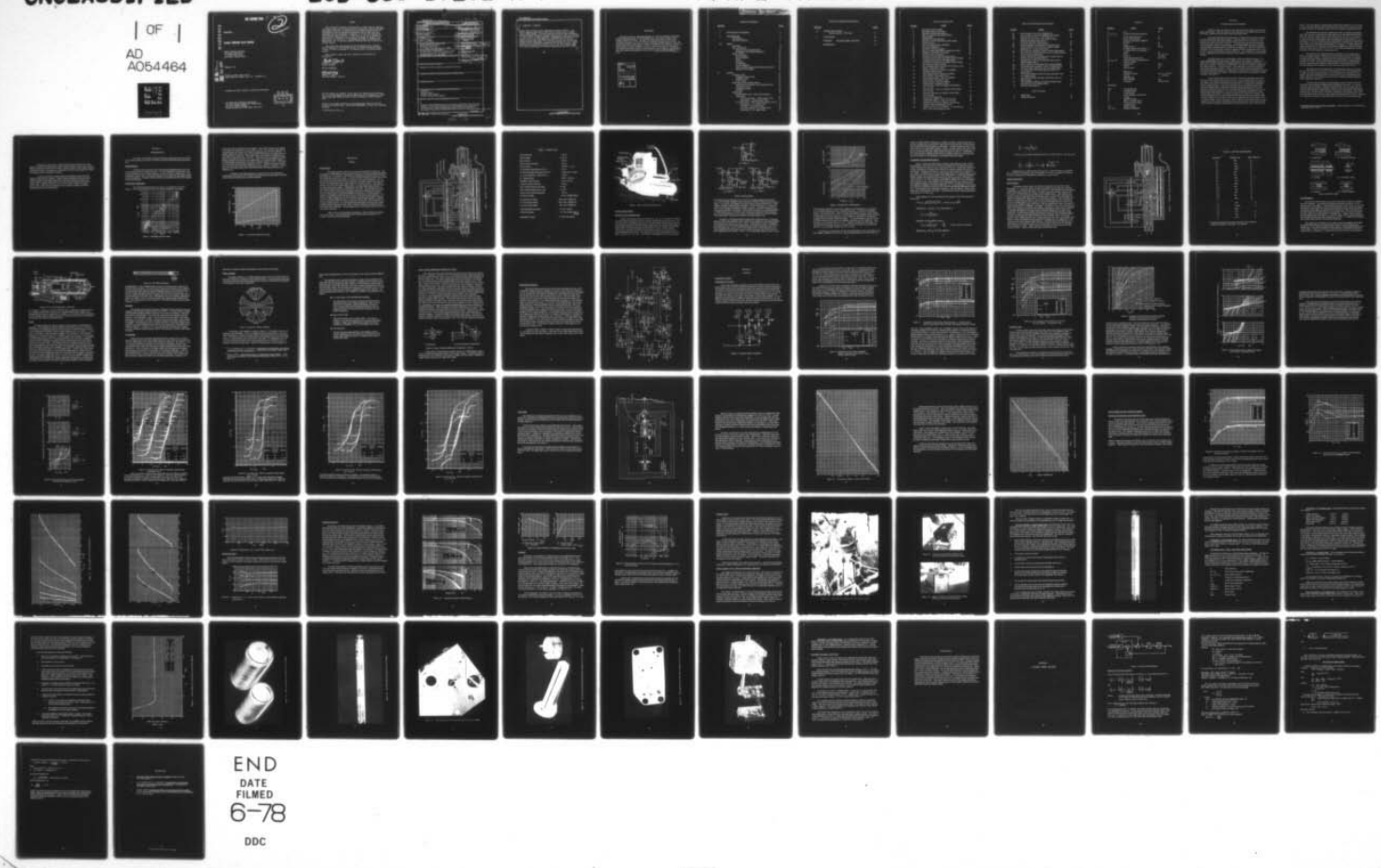

END
DATE
FILMED
6-78
DDC

AFAPL-TR-78-7

FLUIDIC PRESSURE RATIO SENSOR

ENERGY CONTROLS DIVISION
THE BENDIX CORPORATION
717 NORTH BENDIX DRIVE
SOUTH BEND, INDIANA 46620

FEBRUARY 1978

TECHNICAL REPORT AFAPL-TR-78-7
FINAL REPORT FOR PERIOD JUNE 1974 - DECEMBER 1977

AIR FORCE AERO PROPULSION LABORATORY
AIR FORCE WRIGHT AERONAUTICAL LABORATORIES
AIR FORCE SYSTEMS COMMAND
WRIGHT-PATTERSON AIR FORCE BASE, OHIO 45433

NOTICE

When Government drawings, specifications, or other data are used for any purpose other than in connection with a definitely related Government procurement operation, the United States Government thereby incurs no responsibility nor any obligation whatsoever; and the fact that the Government may have formulated, furnished, or in any way supplied the said drawings, specifications, or other data, is not to be regarded by implication or otherwise as in any manner licensing the holder or any other person or corporation, or conveying any rights or permission to manufacture, use, or sell any patented invention that may in any way be related thereto.

This report has been reviewed by the Information Office (ASD/OI) and is releasable to the National Technical Information Service (NTIS). At NTIS, it will be available to the general public, including foreign nations.

This technical report has been reviewed and is approved for publication.

Charles E. Ryan, Jr.

CHARLES E. RYAN, JR.
Project Engineer

FOR THE COMMANDER

Charles E. Bentz

CHARLES E. BENTZ
Tech Area Manager, Controls

"If your address has changed, if you wish to be removed from our mailing list, or if the address is no longer employed by your organization, please notify AFAPL/TBC, WPAFB OH 45433 to help us maintain a current mailing list."

Copies of this report should not be returned unless return is required by security considerations, contractual obligations, or notice on a specific document.

AIR FORCE/56780/31 March 1978 — 150

(9) Final rept. 17 Jun 74-15 Dec 77,

UNCLASSIFIED

SECURITY CLASSIFICATION OF THIS PAGE (When Data Entered)

(19) **REPORT DOCUMENTATION PAGE**

READ INSTRUCTIONS BEFORE COMPLETING FORM

(18) 1. REPORT NUMBER: AFAPL-TR-78-7	2. GOVT ACCESSION NO.
(11) 3. RECIPIENT'S CATALOG NUMBER: 17 Feb 78	
(6) 4. TITLE (and Subtitle): FLUIDIC PRESSURE RATIO SENSOR.	5. TYPE OF REPORT & PERIOD COVERED: Technical Report (Final) June 1974 - December 1977
(14) 6. PERFORMING ORG. REPORT NUMBER: ECD-866-19292-R	
(10) 7. AUTHOR(s): David C. Thoman, James M. Eastman	(15) 8. CONTRACT OR GRANT NUMBER(s): F33615-74-C-2068 (Part I)
9. PERFORMING ORGANIZATION NAME AND ADDRESS: Energy Controls Division, The Bendix Corporation, 717 N. Bendix Dr. South Bend, IN 46620	(16) 10. PROGRAM ELEMENT, PROJECT, TASK AREA & WORK UNIT NUMBERS: Program Element 62203F, Project 3066, Task 306603, W.U. 30660367 (17) 03
11. CONTROLLING OFFICE NAME AND ADDRESS: Air Force Aero - Propulsion Laboratory (TBC), AF Wright Aeronautical Laboratories, AFSC, Wright-Patterson AFB OH 45433	12. REPORT DATE: February 17, 1978
	13. NUMBER OF PAGES: ix + 74
14. MONITORING AGENCY NAME & ADDRESS (if different from Controlling Office)	15. SECURITY CLASS. (of this report): UNCLASSIFIED (12) 84p.
	15a. DECLASSIFICATION/DOWNGRADING SCHEDULE: N/A

16. DISTRIBUTION STATEMENT (of this Report)

Approved for Public Release; distribution unlimited

17. DISTRIBUTION STATEMENT (of the abstract entered in Block 20, if different from Report)

18. SUPPLEMENTARY NOTES

19. KEY WORDS (Continue on reverse side if necessary and identify by block number)

"Fluidics"
"Pressure Ratio"
"Pressure Ratio Sensors"
"Fluidic Pressure Ratio Sensors"

20. ABSTRACT (Continue on reverse side if necessary and identify by block number)

Pressure ratio measurements are used to monitor and control core engine and by-pass air flow rates, compressor and fan performance, and engine thrust. The wide range of required operating pressure levels plus the severe environment (vibration and temperature) makes the use of discrete pressure

→ over

Continued.

DD FORM 1 JAN 73 1473 EDITION OF 1 NOV 65 IS OBSOLETE

UNCLASSIFIED

SECURITY CLASSIFICATION OF THIS PAGE (When Data Entered)

402 286

20. ABSTRACT (Continued)

sensors (with electronic ratio computation) extremely difficult. The fluidic approach avoids much of this difficulty and provides a simple, rugged, compact design. The design features, operation, bench evaluation testing and engine testing of a fluidic pressure ratio sensor are described. The sensor design is readily adaptable to measurement of any engine related pressure ratio, but it was specifically configured and developed for measuring burner inlet mach number (corrected air flow) for the Pratt and Whitney Aircraft ATEGG engine. The sensor was designed for direct engine mounting and uses compressor discharge air for the flow circuits. Sensor operation was tested for the range of burner inlet total pressures from 6.6 to 500 psia and sensor environmental temperatures from -65 to 750°F.

FOREWORD

This final report was submitted December 16, 1977 by the Bendix Corporation, Energy Controls Division, 717 North Bendix Drive, South Bend, Indiana, under Contract F33615-74-C-2068. The effort was sponsored by the Air Force Aero Propulsion Laboratory, Air Force Systems Command, Wright-Patterson AFB, Ohio under Project 3066, Task 306603, and Work Unit 30660367 with Charles E. Ryan, Jr., AFAPL/TBC, as Project Engineer. David C. Thoman and James M. Eastman of The Bendix Corporation, Energy Controls Division, were technically responsible for the work, which was executed over the period from June 17, 1974 to December 15, 1977.

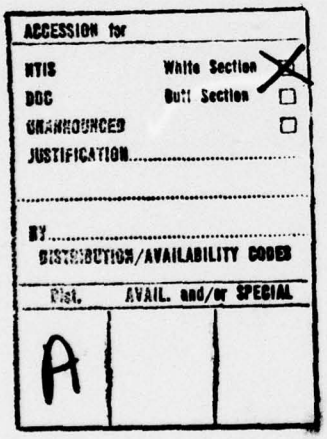

TABLE OF CONTENTS

TABLE OF CONTENTS (CONCLUDED)

LIST OF ILLUSTRATIONS

LIST OF ILLUSTRATIONS (CONCLUDED)

LIST OF TABLES

SYMBOLS

SYMBOL	NAME	UNITS
A	Area	in^2
A_1, A_2, etc.	Numbered Threaded Restrictors	
b	Piston Radial Clearance	in.
c	Piston Circumference	in.
C	Restrictor Discharge Coefficient	
D	Diameter	in.
F	Force	lb.
H	Feedback Gain	psi/in.
k	Adiabatic Specific Heat Ratio (1.4)	
K	A constant Term in an Equation	
L	Length	in.
m	Mass	lb. $sec.^2$/in.
P	Pressure	psi, psia
Q	Piston Displacement Rate	$in.^3$ / sec.
R_1, R_2, etc.	Numbered Shim Plate Restrictors	
S	Laplace Variable	
T	Temperature	deg F
V	Volume	$in.^3$
x	Piston Travel	in.
Δ	Difference	
μ	Absolute Viscosity	lb. wt. -$sec/in.^2$
μ	Microns	~ .00004 in.
ζ	Damping Ratio	
τ	Time Constant	Sec.
ω	Frequency	rad/sec or Hz

Subscripts :

ABV	Air Bearing Vent
as	Amplifier Supply
B	At the Burner
C	At the Amplifier Control Port
n	Natural
O	Amplifier Output
s	Static (at Burner Inlet)
t	Total (at Burner Inlet)
v	Amplifier Vent
vac	Ejector Vacuum
1, 2, etc.	Sequence Designation

SECTION I

INTRODUCTION AND SUMMARY

Pressure ratios are among the more important measurements of gas turbine engine performance. They are used to monitor and control core engine and by pass air flow rates, compressor and fan performance and engine thrust.

This report describes the development of a fluidic pressure ratio transducer for sensing the burner inlet Mach number. This Mach number is a measure of compressor corrected air flow and is indicated by the ratio $(P_t - P_s)/P_t$ where P_t is the total pressure and P_s the static pressure. The design requirements were predicated on direct engine mounting of the transducer on an advanced high performance engine, with the fluidic circuits powered by compressor discharge air. The unit would thus be subjected to the environmental extremes of engine vibration, temperatures from -65°F to 750°F, and the contaminants present in engine air. It was designed to require neither thermal conditioning nor pressure regulation of the engine air used to power the fluidic circuits.

The fluidic approach is an alternative to the use of discrete sensors. It's major appealing feature is its compact, rugged and low cost design. In addition, a single unit is readily adaptable to all engine pressure ratio sensing requirements. The unit can be mounted at the point of measurement to enhance its response to changes in the sensed pressures. Discrete sensors, on the other hand, are severely affected by temperature and engine vibration. They must be mounted in vibration isolated and thermally conditioned housings. Normally they are housed with the electronic controller forward of the burner on the engine. The length of sense lines may degrade the output response of the sensors.

If discrete pressure sensors are used, electronic computation can extract the ratio of their outputs with extreme precision. But if pressure levels vary over a wide range, even sensors having good accuracy in percent of full scale can exhibit low percent of point accuracy at the lowest pressure level -- resulting in low indicated pressure ratio accuracy. For burner inlet pressure Mach number sensing on the Pratt and Whitney ATEGG (Advanced Technology Engine Gas Generator), the total pressure P_t will vary from 12.6 psia to 510 psia (40:1) and $\Delta P/P_t$ ratios of .05 to .10 must be accurately determined. To meet Pratt and Whitney objectives for ATEGG turbine stator vane control, a net target accuracy of ±1% of point was selected. For discrete pressure sensors, this requires the individual sensors to be accurate within .00063% of full scale. If ΔP and P_t sensors are employed, then the ΔP sensor must be accurate within .0125% of full scale. These accuracy requirements present a major challenge even in a closely controlled laboratory environment. All precision discrete sensors employ electronic compensation for temperature level and/or pressure level

effects. The large degree of compensation required and variations from one sensor to other supposedly identical sensors generally require not only very accurate compensation but that each individual sensor must have a different compensation table.

By bucking the two pressures against each other in a nulling arrangement, wide range pressure transducing accuracy problems are alleviated with the fluidic approach. Since the output pressure ratio signal varies over only a 2:1 range (.05 to .10), its accuracy requirement in percent of full scale is more modest (± .5%). The fluidic circuits are essentially self-compensating for temperature and pressure level effects. As a result the temperature sensitivity is much less than that for discrete sensors and the pressure level sensitivity is minimal. To achieve indicated output accuracies of ± 1% requires less electronic compensation, even with the unit exposed to temperatures from -65° to 750°F. The required compensation can thus be simpler than that required for discrete sensors.

The Model PRA-A1 fluidic pressure ratio sensor was first developed in 1969 as an engine duct Mach number sensor for application to duct nozzle control for the B-1 (AMSA) engine. It underwent extensive testing and later was adapted to burner inlet Mach number sensing on the J-85 engine under Air Force Contract F-33615-70-C-1503. An improved fluidic pressure ratio sensor, Bendix Model PRA-A2, featuring faster response, better filtration, and reduced size and cost, was also tested on the J-85 under Air Force contract F-33615-72-C-1716.

The objectives for the Model PRA-A3 development program are to adapt the PRA-A2 sensor for (1) lower $\Delta P/P$ sensing range (.050 to .100 instead of .100 to .200), (2) more accurate sensing (± 1% of point target for full range), and (3) higher temperature capability (750°F instead of 450°F), and to demonstrate satisfactory operation of the resulting unit on the Pratt & Whitney advanced technology turbine engine gas generator.[1]

The basic PRA-A2 design was substantially revised to meet the PRA-A3 objectives, after extensive breadboard type computing circuit tests. Two sensors were fabricated for testing. Following component tests, the first sensor was assembled, calibrated and bench tested for static accuracy with varying temperature, pressure, and vibration, and the frequency response was determined. Test results indicated that a small amount of electronic compensation for temperature and pressure level effects will correct the output signal to the desired ±1% accuracy. The form of compensation required is relatively simple and should be easily programmable.

[1] Advanced Turbine Engine Control Components, Bendix Proposal No. ECD-863-591 P, September 1973, p. C1-1.

Vibration Test showed that, with the unit properly mounted on the engine (piston axis parallel to engine axis), engine vibration should not affect sensor output. Dynamic response exceeded 20 Hz except at extreme altitude, where engine responses would also be slower. Response was considered to be more than adequate for closed loop engine fuel flow and geometry control.

A total of 313 hours of engine testing was performed on the Pratt and Whitney ATEGG and J-57 engines. Engine testing substantiated design integrity, with the exception of the high temperature LVDT which failed after 85 hours of engine running. Higher temperature rated windings and bobbin insulation should correct this. Otherwise the sensor proved to be a highly reliable and rugged device, able to meet the requirements for direct engine mounting on advanced high performance gas turbine engines.

SECTION II

REQUIREMENTS

The sensor is designed to meet the functional requirements for burner inlet mach number sensing on the Pratt and Whitney advanced technology engine gas generator.

PERFORMANCE

The sensor must sense the ratio of the pressure differential (P_t-P_s) or ΔP to the total pressure P_t at the burner inlet. It is to be calibrated to indicate the value of this parameter ($\Delta P/P_t$) between values of .05 and .10 with a nominal value of .075 (equivalent to Mach .335). The target accuracy is ±1% of point for the range of engine operating conditions. Transient response should be compatible with closed loop engine control requirements.

OPERATING CONDITIONS

The required operating range of P_t and $P_t - P_s$ pressures is shown in Figure 1. The cross-hatched areas are only entered transiently and sensing

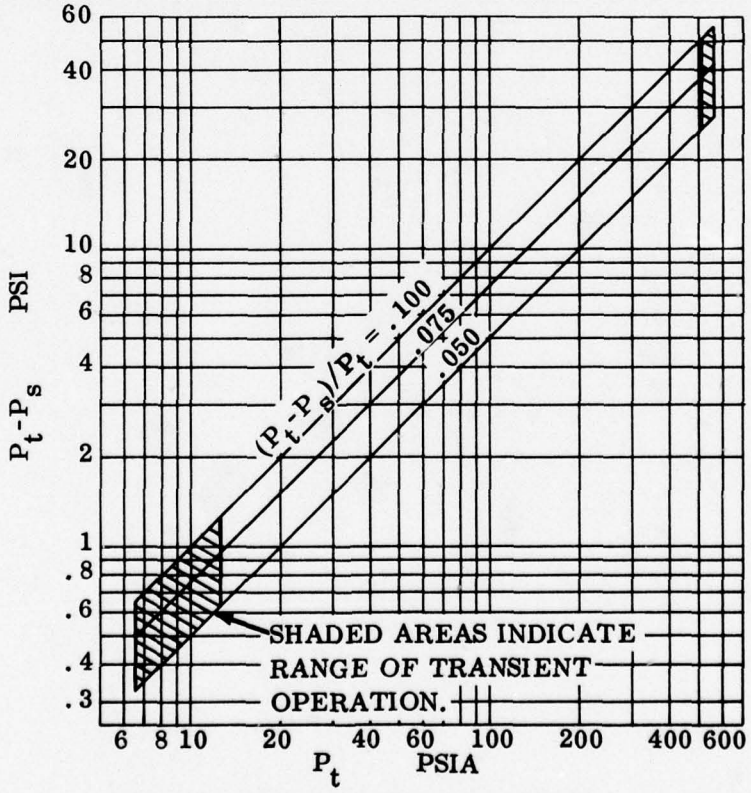

Figure 1 Operating Pressure Range

accuracy for these operation areas is relaxed. Thus the ±1% accuracy goal applies to the range of P_t between 12.6 and 510 psia (~40:1). The accuracy target applies to engine speeds and compression ratios exceeding those for the idle condition. At engine speeds above idle the ratio of burner inlet total pressure to nacelle pressure will range from 3 to about 25. The sensor must be insensitive to nacelle pressure levels in the range from 1/25 to 1/3 of P_t. The sensor must be designed for direct engine mounting in the vicinity of the burner inlet. On advanced turbine engines, it is estimated that temperatures at the sensor could be as high as 750°F. The sensor is to be designed for operational capability to 750°F. Maximum operating temperature will occur when burner input total pressure P_t is also at a maximum. Figure 2 shows the estimated maximum and minimum effective operating temperatures in relation to P_t.

In addition to the high temperature, the sensor must meet operational requirements when subject to the vibration and maneuvering accelerations associated with aircraft gas turbine engine mounted equipment.

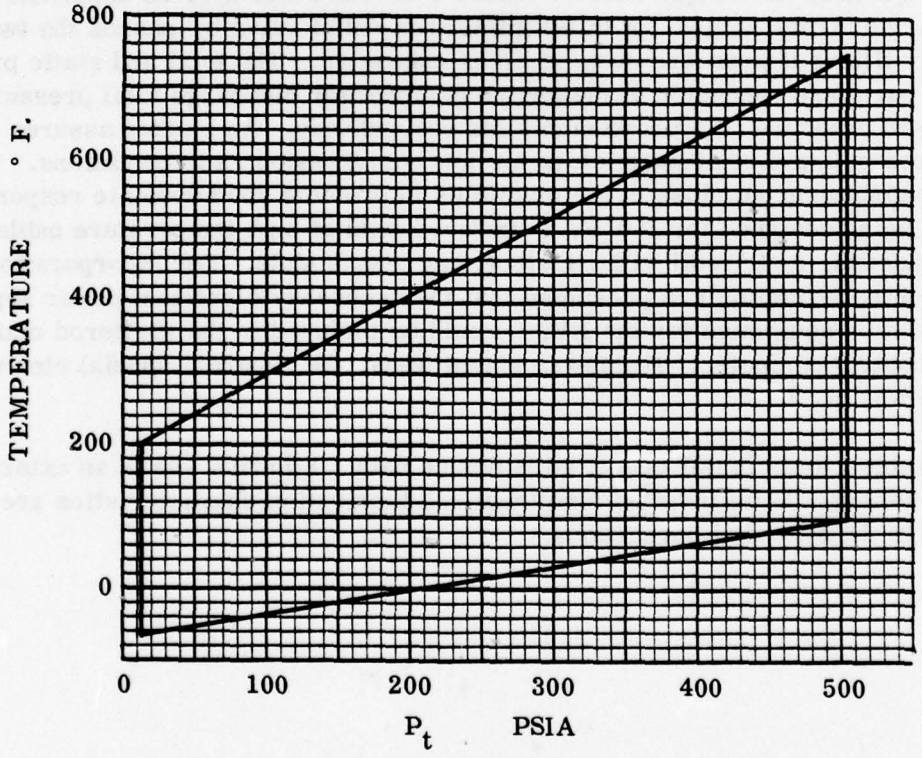

Figure 2 Operating Temperature Range

SECTION III

DESIGN

DESCRIPTION

The fluidic pressure ratio sensor is shown schematically in Figure 3. The unit employs a lightweight air bearing supported piston, having an attached magnetically permeable core, or armature. The piston is positioned as a function of $\Delta P/P_t$ by fluidic computation and power circuits. A linear variable differential transformer (LVDT) provides an electrical output signal proportional to the armature position. Air at burner inlet wall static pressure P_B is supplied to the fluidic amplifier and the critical flow circuits through a four stage progressive filtration system. This system consists of a coarse first stage barrier filter, a second stage cyclone separator and two final barrier filter stages. A differential area relief valve by-passes the two final barrier filters if pressure drop becomes excessive. The total and static pressure sense ports are connected to the engine compressor discharge total pressure (P_t) and static pressure (P_s) probe manifolds respectively. An ejector assures choking of computing circuit restrictors for low compression ratio conditions. The sensor is engine mounted close to the manifolds to promote good dynamic response. The sensor being designed for 750°F, a six foot length of high temperature cable is used to connect the LVDT coil with its electronic test module. For incorporation in an engine control system, it is presumed that the necessary electrical power supply and demodulation equipment for the LVDT would be included in the sheltered main electronic control computer. For development tests, the separate special electronic test module was used.

Table 1 lists major quantitative design data. Figure 4 shows an external view of the sensor. More detailed functional and fabrication characteristics are brought out in the following paragraphs.

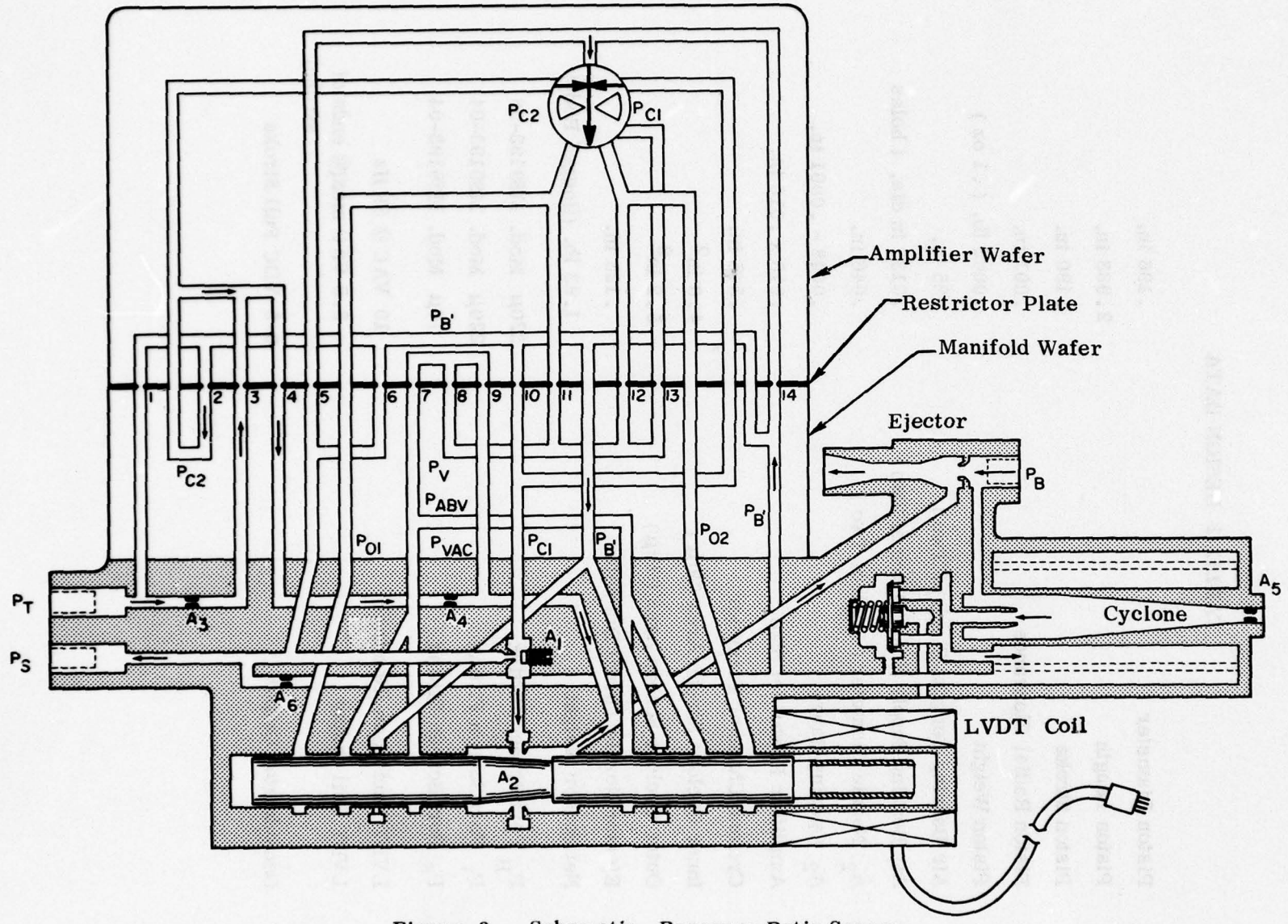

Figure 3 Schematic, Pressure Ratio Sensor

TABLE 1 DESIGN DATA

Piston Diameter	.196 in.
Piston Length	2.983 in.
Piston Stroke	.190 in.
Piston Radial Clearance	.001 in.
Piston Weight	.0062 lb. (.1 oz)
Air Bearing Lengths (Each of Two)	.25 in.
Air Bearing Supply Holes (Each of Two)	.0135 in dia, 4 holes
A_2 Nozzle Diameter (Each of Two)	.046 in.
A_2 Opening Range	.0048 - .0061 in.
Amplifier Power Jet Size	.015 x .016 in.
Cyclone Chamber Diameter	.345 in.
Inner Cyclone Screen Area (20μ)	4.0 in^2
Outer Cyclone Screen Area (10μ)	5.2 in^2
Ejector Nozzle Throat Diameter	.125 in.
Net Sensor Weight	1.93 lb. (Hogged Body)
P_B Port Screen Fitting	220μ Mod. MS9193-06
P_t Port Screen Fitting	220μ Mod. MS9193-04
P_s Port Screen Fitting	70μ Mod. MS9193-04
LVDT Excitation (Nominal)	10 VAC @ 5K Hz
LVDT Coil Output	3.5 VAC max(@ ends of stroke)
Demodulator Output	0-5 VDC Full Stroke

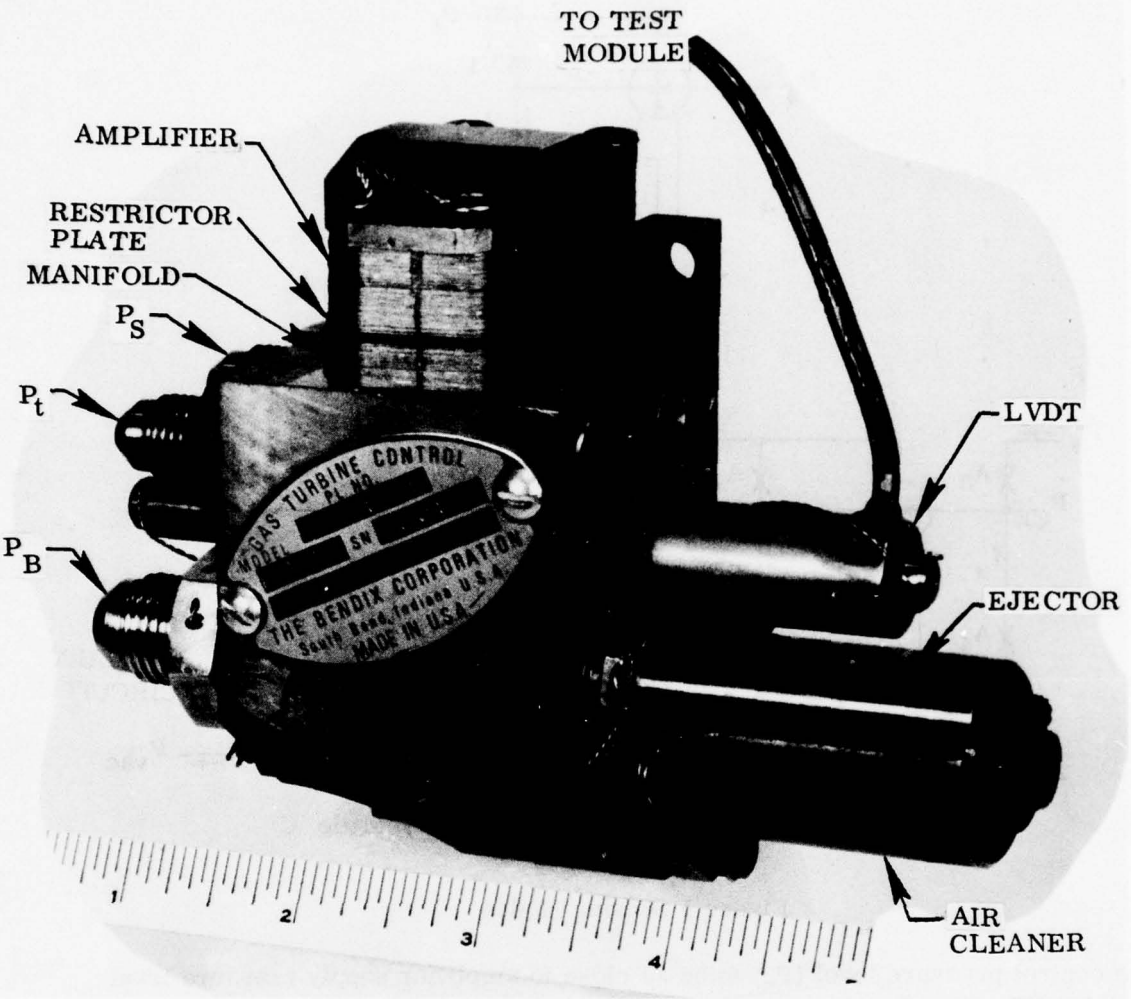

Figure 4 PRA-A3 Pressure Ratio Sensor

RATIO COMPUTATION

Selection of the Computing Mode

Figure 5 shows three modes of sensing $(P_t - P_s)/P_t$. The first one, Mode A, was used in the earlier pressure ratio sensors, Models PRA-A1 and PRA-A2. The lack of a source of amplifier supply air at a pressure higher than the P_t pressure to be sensed for the PRA-A3 plus the smaller sensed values of $\Delta P/P_t$ and the required wider range of operating pressures prompted the search for a better sensing mode. Mode A flows air from P_t through a fixed restrictor A_1 and a choked variable restrictor A_2 adjusted to balance the intermediate pressure P_{C1} against P_s by a fluidic amplifier driven piston. The position of A_2 is then an indication of the ratio of $P_t - P_{C1}$ (or $P_t - P_s$) to P_t. For the PRA-A3 application, this mode requires

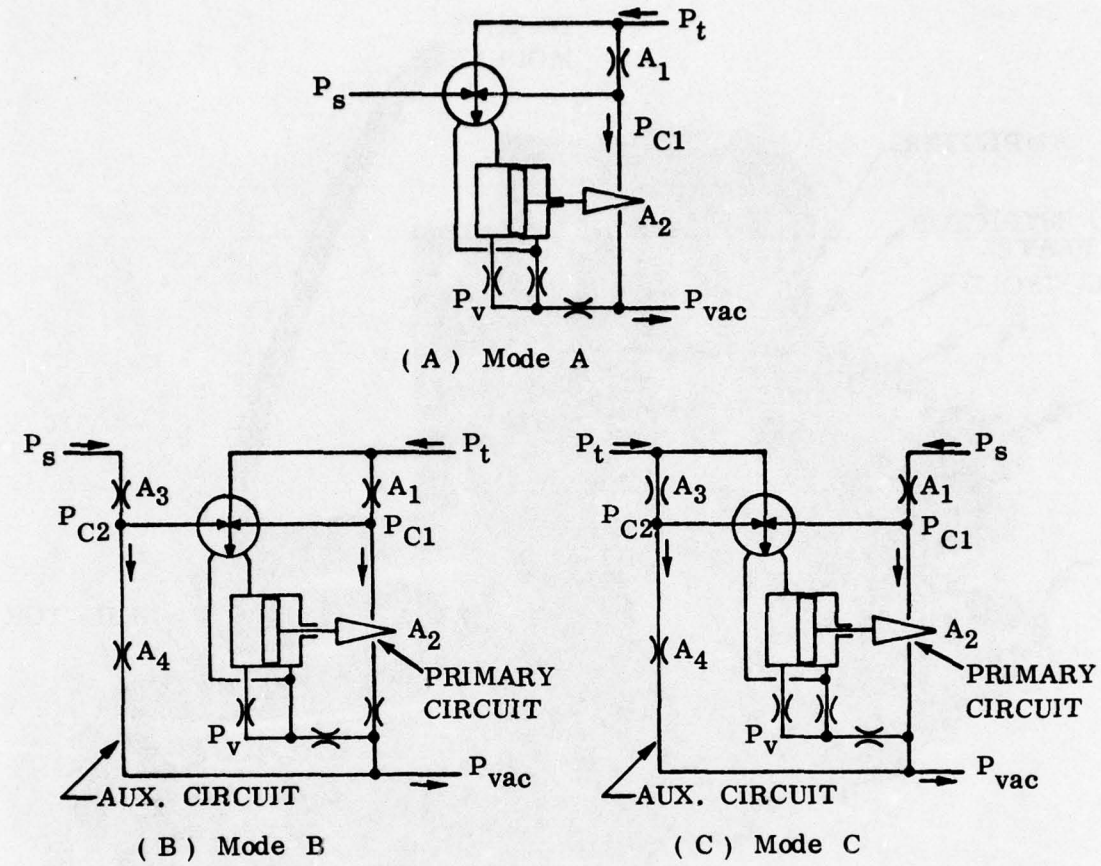

Figure 5 Sensing Modes

the control pressure level (P_s) to be so close to amplifier supply pressure level ($\sim P_t$) that available amplifier styles must operate outside of their best performance range. As a result, the amplifier vent level must be a higher fraction of P_t, which reduces available saturated pressure output. In Mode B of Figure 5, control pressure level is lowered by bleeding down both P_s and P_t, using fixed restrictors A_3 and A_4 in the auxiliary (P_s) circuit, so that a fixed fraction of P_s is balanced against a varying fraction of P_t. In Mode C, the circuits are switched so that the primary A_1 to A_2 circuit generates a P_{C1} equal to a varying fraction of P_s and the auxiliary circuit generates a P_{C2} which is a smaller but fixed fraction of P_t.

In Figure 6, the characteristics of these three sensing modes are compared. Figure 6A shows the calculated ratio of maximum to minimum A_2 area plotted against the nominal P_c/P_t ratio (for $P_s/P_t = .925$). It shows that the more the amplifier control pressure is lowered (by bleeding down in the auxiliary circuit), the lower is the required A_2 max $/A_2$ min ratio for full piston stroke. Reduction in this ratio makes machining the piston cone and any variation in second order effects (such as flow coefficients) more critical. Mode "C" has substantially higher A_2 max $/A_2$ min.

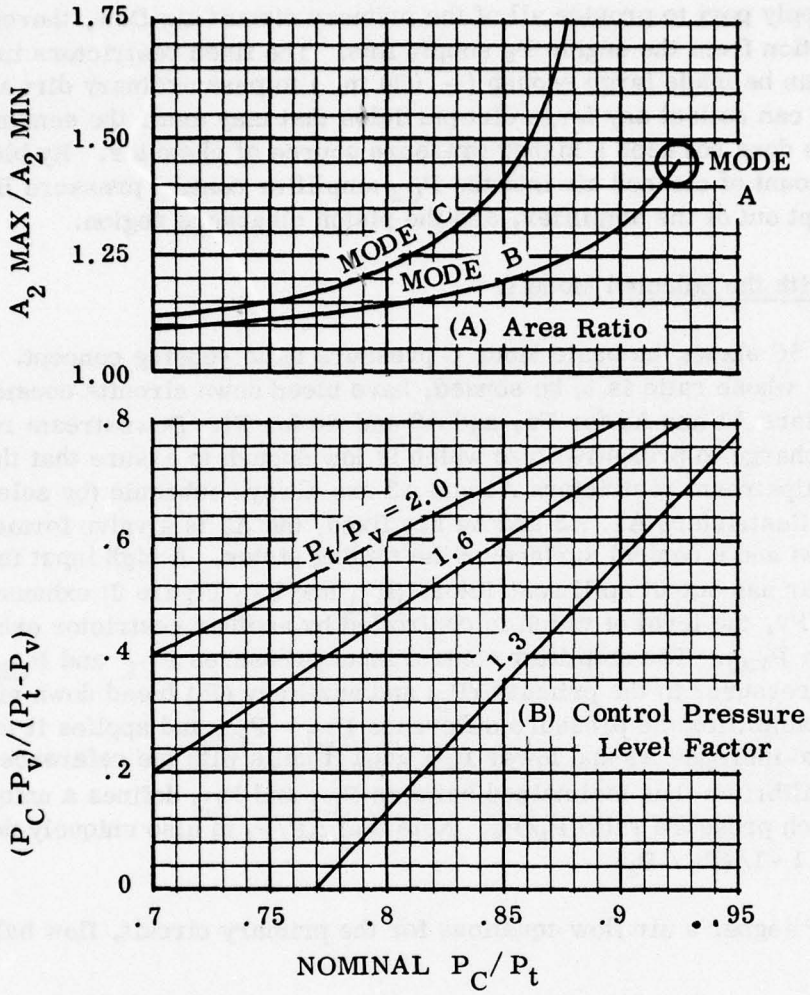

Figure 6 Sensing Mode Considerations

At the limiting condition for mode B (no auxiliary circuit bleed down), P_c becomes P_s, and mode B becomes mode A, with the nominal P_c / P_t equal to the nominal P_s/P_t = .925 (circled point). Figure 6B shows the influence of P_c/P_t on the control pressure level factor $(P_c - P_v)/P_t - P_v)$ assuming P_t is the amplifier supply pressure. It is desirable to operate at high P_t/P_v (low amplifier vent levels) to provide good amplifier pressure output at extreme altitude. It is also desirable to operate at lower control pressure level factors for amplifier operation nearer to optimum. These both favor a low nominal value of P_c / P_t. Figure 6A makes clear that mode C is best because for the same A_2 max / A2 min it has lower nominal P_c/P_t and for the same P_c / P_t it has higher nominal A_2 max / A_2 min.

By using P_s in the primary circuit, the selected Mode C also contributes to the dirt handling capability of the sensor. P_B (which approximates P_t) can be used as a

source for higher pressure cleaned air, making it possible to bleed enough clean air into the P_s supply port to provide all of the primary circuit air flow, thereby preventing dirt ingestion from the engine P_s supply line. The fixed restrictors in the auxiliary circuit can be made large enough (~.030 in.) to pass ordinary dirt and a small coarse screen can collect any large dirt particles that may enter the sensing line, so that the P_t line does not need a higher pressure source of clean air. By bleeding a very small amount of cleaned air into the P_{C2} amplifier control pressure line, dirt can also be kept out of the amplifier, and the piston clearance region.

Computation with the Selected Mode C

Figure 5C shows the basic Mode C pressure ratio sensing concept. Both of the pressures, whose ratio is to be sensed, have bleed down circuits consisting of series restrictors A1 and A2 for Ps, and A3 and A4 for Pt. Downstream restrictors A2 and A4 discharge to pressure Pvac which is low enough to assure that they are both choked. Upstream restrictors A1 and A3 are always subsonic (by selection of area ratios). Restrictors A1, A3 and A4 are fixed, but A2 is a valve formed by a gap between nozzles and a conical surface on the sliding piston. A high input impedance fluidic amplifier has output spill restrictors (R_{11} and R_{12} Figure 3) exhausting to a vent pressure Pv, the level of which is controlled by another restrictor exhausting to ejector vacuum P_{vac}. The amplifier control input pressures P_{C1} and P_{C2} are the intermediate pressures in the primary (P_s) and auxiliary (P_t) bleed down circuits. The amplifier amplifies the pressure difference $P_{C1} - P_{C2}$ and applies it to the piston in a direction to increase A2 and lower P_{C1} until it nulls with the reference pressure P_{C2}. The equilibrium thus maintained between P_{C1} and P_{C2} defines a unique piston position for each pressure ratio P_t/P_s. Note that $\Delta P/P_t$ is also uniquely determined, since $\Delta P/P_t = 1 - 1/(P_t / P_s)$.

Using Fliegner's air flow equations for the primary circuit, flow balance requires that :

$$1.06\, C_1 A_1 \sqrt{P_{C1}(P_S - P_{C1})/T_1} = .53\, C_2 A_2 P_{C1} / \sqrt{T_2}$$

Assuming $C_1 = C_2$ and $T_1 = T_2$, this reduces to :

$$P_{C1} = \frac{P_s}{1 + (A_2 / 2A_1)^2}$$

Similarly, for the auxiliary circuit :

$$P_{C2} = \frac{P_t}{1 + (A_4 / 2A_3)^2} = \frac{P_t}{K_1} \quad \text{(since } A_3 \text{ and } A_4 \text{ are fixed)}$$

Equating P_{C1} and P_{C2} (the null condition) :

$$\frac{P_t}{P_s} = \frac{K_1}{1 + (A_2 / 2A_1)^2}$$

If valve A_2 has a linear characteristic and A_1 is fixed, then $A_2 / 2A_1 = K_2 x$ and:

$$\frac{P_t}{P_s} = \frac{K_1}{1 + K_2^2 x^2} \quad \text{or } x = \frac{1}{K_2} \sqrt{\frac{K_1}{P_t / P_s} - 1}$$

Adjustment of A_1 relative to the mean A_2 and / or the area ratio A_3/A_4 selects the mean value of the pressure ratio to be sensed. The ratio of maximum to minimum $\Delta P/P_t$ to be sensed can be adjusted by variation of A_2 max/A_2 min.

DESIGN FEATURES

Flow Passages

The fluidic circuits employ two diffusion bonded photo-etched shim wafers (See Figure 3). One of the wafers contains the amplifier and the other has extensive manifolding. A restrictor shim plate (.006" thick) is sandwiched between these wafers. Photo etched copper gaskets are used for sealing between the restrictor plate and the two wafers, as well as between the body and the manifold wafer. Since pattern complexity is easily provided with photo-etched fabrication, considerable manifolding versatility was designed into these wafers, as indicated by Figure 3. This versatility provides (1) simpler body machining -- holes at the manifold interface may be drilled at the most convenient place, (2) a number of choices in arrangements for control of the pressures for amplifier supply and vent (P_v) and air bearing vent (P_{ABV}), (3) choice of either thin plate style or threaded (convergent - divergent or long L/D) restrictors, or both, at the A_3 and A_4 locations in the auxiliary computing air circuit and (4) capability for bleeding cleaned air at pressure P_B, into selected pressure lines to reduce dirt sensitivity. In addition to providing convenient means of altering computing circuit restrictor styles for minimizing Reynolds number sensitivity, this passaging flexibility permits easy alteration for optional sensing of other pressure ratios (compressor pressure ratio, engine pressure ratio, turbine pressure ratio, duct mach number, etc.). Figure 7 shows the complete sensor schematic in simpler form as configured for only the burner inlet mach number sensing function. Passages that are blocked (as by undrilled holes at the restrictor plate) are not shown and no restrictors are indicated where openings are large. Table 2 shows the selected restrictor sizes used to calibrate the sensor. Figure 8 shows the styles of restrictors used.

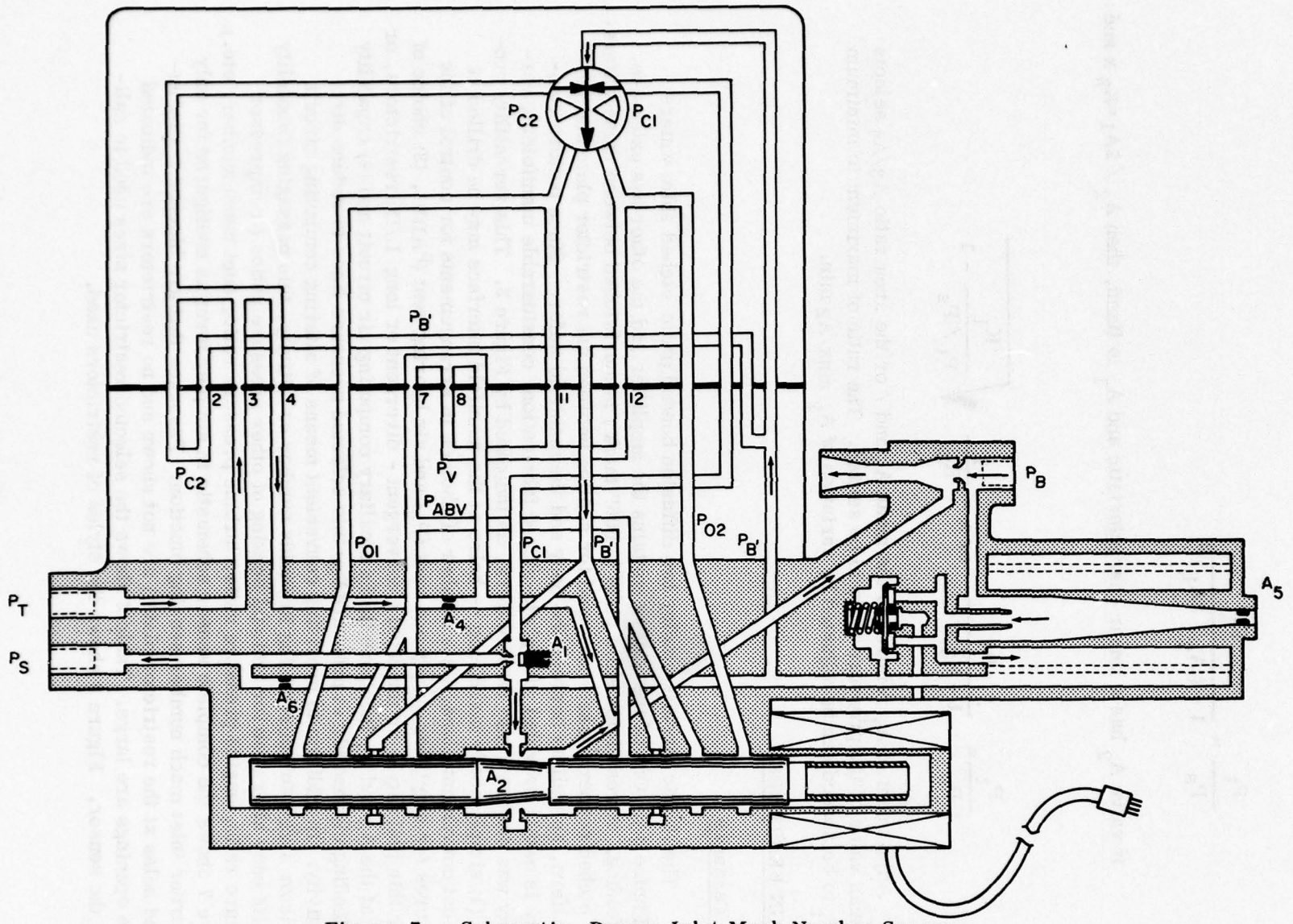

Figure 7 Schematic, Burner Inlet Mach Number Sensor

TABLE 2 SETTING RESTRICTORS

Restrictor*	Diameter (in)	Style (Figure 8)
R_1	Blk	
R_2	.006	
R_3	.0312	
R_4	.0305	
R_5	Blk	
R_6	Blk	
R_7	.023	D
R_8	.0175	
R_9	Open	
R_{10}	Blk	
R_{11}	.020	
R_{12}	.020	
R_{13}	Blk	
R_{14}	Open	
A_1	.082	B
A_2	.046 (2)	C
A_3	Open	
A_4	.055	F
A_5	.020	E
A_6	.055	F

* R indicates numbered shim plate restrictors and A indicates numbered restrictors in the body. See Figure 3.

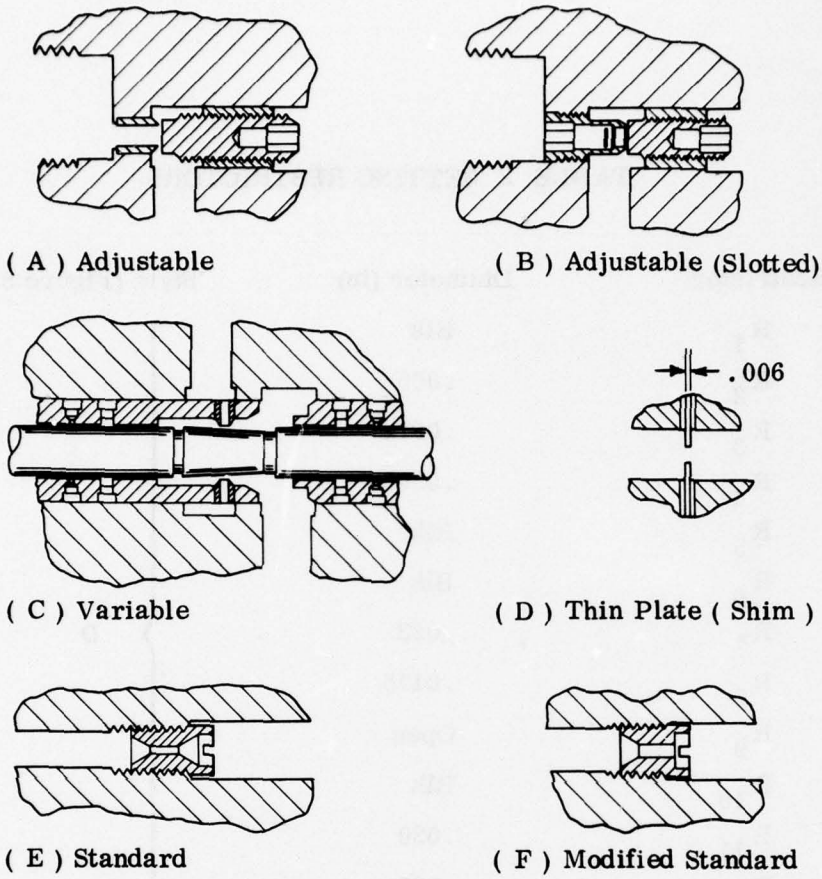

Figure 8 Restrictor Styles

Dirt Management

Air at burner inlet pressure P_B is used to power the air ejector and supply a source of clean air. P_B pressure is assumed to be within a percent or so of P_t pressure and to vary with it. After passing through the coarse screen, air for ratio computation, piston actuation, and the air bearings goes to the cyclone air cleaner. The same cyclone design was tested earlier at Bendix and found to separate 99% of AC Spark Plug Fine test dust with about 1% pressure drop. The dirt is discharged from the cyclone by a small quantity of scavenge flow. Figure 9 shows the basic chamber design used in the PRA-A3. From the cyclone, the air passes through the two concentric final barrier filter stages (20μ and 10μ). A relief valve by-passes the screens if their pressure drop becomes excessive.

This cleaned air at pressure P_B' is used to power the amplifier and to bleed air into flowing passages as needed to assure that no large dirt particles pass through A_1 or A_2 or into the piston clearance regions. Adequate protection for the rather large (.030 in dia) auxiliary circuit restrictors is provided by the 220μ screen in the P_t supply port. To assure that no coarse dirt gets to the piston via

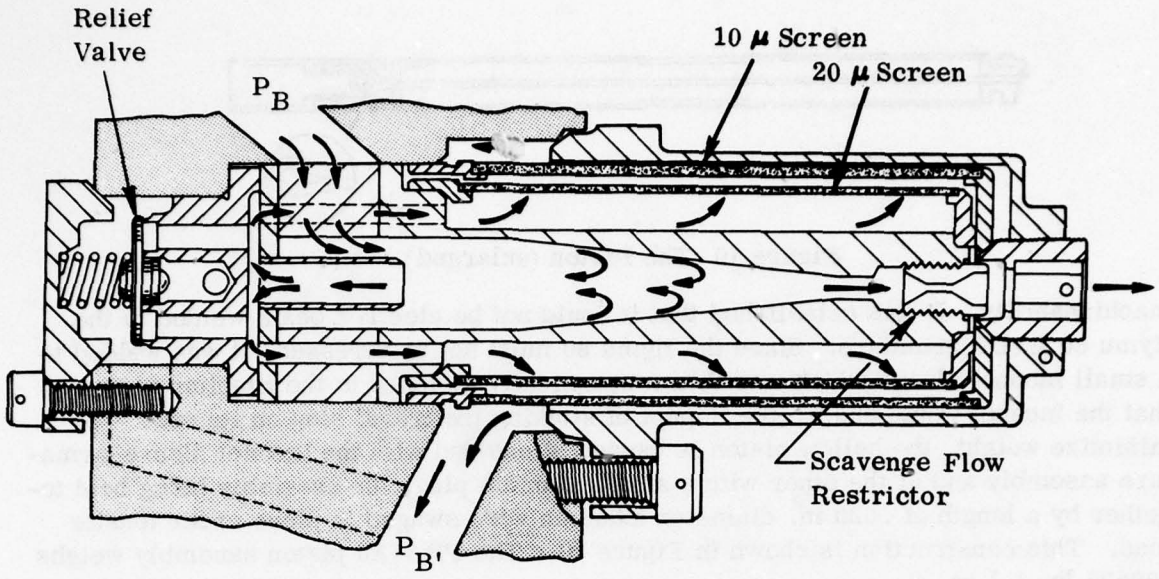

Figure 9 The Air Cleaning System (Enlarged)

the amplifier, a small P_B' air flow is bled into the P_s supply line through restrictor A_6 - enough to provide air for the primary computing circuit plus a slight flow exhausting into the engine P_s supply line. In addition, a very small P_B' flow is bled into the P_{C2} amplifier control pressure passage via restrictor R_2 so that a very slight flow exhausts into the auxiliary computing circuit.

Piston

The light weight piston with the attached LVDT armature is supported by air bearings. It is positioned by a fluidic amplifier as a function of $\Delta P/P$. The piston end chambers are supplied through laminar restrictors, causing the piston to move at a rate proportional to amplifier output pressure difference $P_{01} - P_{02}$ (Fig. 7). Loop gain is controlled by using appropriate amplifier spill restrictors. This approach makes use of the pressure gain of the amplifier, and allows the use of very small piston displacement without requiring, a correspondingly small amplifier. The required controlled radial clearance for air bearing piston support is also used to establish laminar restrictor thickness by feeding the piston end chambers from annuli spaced inward from the piston ends. The appendix outlines the analytical approach used to select piston diameter and shows that resonance of the piston mass with the compressible end chamber volumes can be managed. All the annular pressure regions for the piston are supplied from sleeves set in the drilled body. A small LVDT coil is fitted at the end of one of the sleeves. For the earlier design approach (Model PRA-A2) the piston was made of filled polyimide with a very small LVDT armature cemented to one end. The piston weighed only .005 lb. For the PRA-A3, the higher temperature requirement ruled out polyimide, which is useful only to about 500°F. Titanium was selected because it combines non magnetic properties with high electrical resistivity, low density, good corrosion resistance, good physical properties, and a reasonable

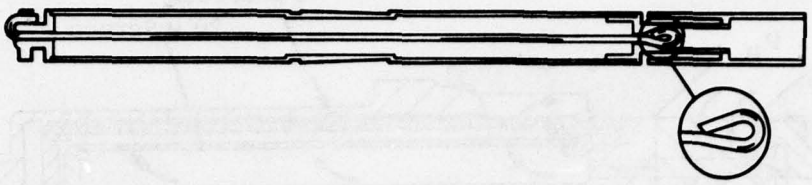

Figure 10 The Piston (enlarged)

machineability. It was established that it could not be electron beam welded to the Hymu 80 LVDT armature. Since the Hymu 80 must not be stressed, it was welded to a small Inconel sleeve which was then mechanically attached to the titanium piston so that the Inconel would absorb the impact of striking the travel stop on its end. To minimize weight, the hollow piston is capped at one end with the Inconel sleeve-armature assembly and at the other with a small titanium plug, the assembly being held together by a length of .020 in. diameter titanium wire swaged in place under tensile load. This construction is shown in Figure 10. The PRA-A3 piston assembly weighs .00625 lb. (.1 oz.)

Materials

The titanium piston material requires compatible sleeves having the same nonmagnetic, high resisivity requirements (for the LVDT). To insure absence of differential thermal expansion problems, titanium is also used for the sleeves. Since the piston floats on air bearings, use of the same material for both should not produce friction or wear difficulties. Again, to be sure the sleeves stay tightly in the machined body, it too is made of titanium, with the sleeves shrunk in place. The manifold and amplifier assemblies are made of austenitic stainless steel shims diffusion bonded together. The remaining parts are made of AMS 5613 or AMS 5640 stainless steel, except for the copper gaskets and the LVDT coil, the materials for which will be described on page 20. A number of "O" ring seals used in the Model PRA-A2 Sensor have been replaced by tapered seating surfaces with titanium or stainless steel mating materials.

Air Bearings

Each of the two air bearings supporting the piston consists of four .0135 in. diameter supply holes in the sleeve equally spaced in a plane normal to the piston and two vent annuli located .125" axially from the holes on each side. See Figure 7. The .001 nominal radial piston clearance is maintained by unbalanced pressure zones created between the annuli when the piston is radially displaced from the center of the sleeve bore. Tests on similar air bearings indicate that each bearing will support approximately one pound per 100 psi supply to vent pressure difference. It thus requires approximately 0.3 psi to support the net .0062 piston assembly weight. Surplus pressure assures that the piston will normally be centered, and cannot be displaced enough to contact its sleeves even with high manuvering or vibration "G 's".

Reference 2 provides background technology for this style of air bearing[2].

Fluidic Amplifier

The fluidic amplifier is a Bendix developed design of the Pavlin type[3] which has been used extensively in Bendix prototype fluidic devices. Its characteristics have been evaluated in detail through testing conducted over the last 10 years and are well defined for the pressure ratio sensor application.

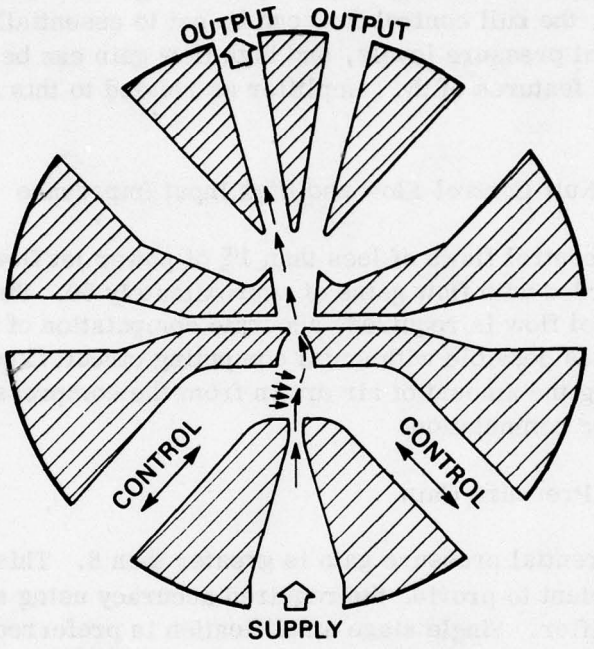

Figure 11 Schematic, Fluidic Amplifier

A schematic of the amplifier is shown in Figure 11. The supply, control, and output ports are identified. The four unlabeled internal vent regions are cross connected and isolated. Pressure in these regions is determined by the net output impedance. The action produced by raising the left control pressure above that on the right is shown. This causes the power jet to bend to the right. It is deflected by the concave wall between the control and the lower internal vent port, causing it to be redirected toward the left output leg. Unlike the conventional jet-on-jet amplifier, the

[2] S. K. Grinnell and H. H. Richardson, Design Study of a Hydrostatic Gas Bearing with Inherent Orifice Compensation, Transactions of the ASME, January 1957.

[3] Pavlin, Cyrille, Experimental Study of a Proportional Fluid Amplifier, Fluid Amplification Symposium, Harry Diamond Laboratories, Wash., D.C., Vol. III 1965, P.5

output pressure differential is in the same direction as the control pressure differential.

The amplifier may be operated push-pull as in this case by providing equal area output restrictors (R_{11} and R_{12} in Figure 7.) spilling to the P_V return, or with single leg output by opening one output directly to the vent pressure and providing a spill restrictor only for the loaded leg. By proper sizing of the geometry in the control interaction region, the null control flow can be set to essentially zero for a wide range of nominal control pressure levels, and high flow gain can be realized. The important performance features of the amplifier as related to this application are as follows:

- Low Null Control Flow and High Input Impedance

  Null control flows of less than 1% of power jet flow have been recorded with flow gains of approximately 50. Since very low control flow is required, accurate computation of pressure ratio is possible with small computing circuit flows-thus reducing the amount of air drawn from the compressor for this fluidic computation.

- High Pressure Gain

  Differential pressure gain is greater than 8. This gain is sufficient to provide the required accuracy using a single stage amplifier. Single stage amplification is preferred from the standpoint of reliability, cost, air consumption, and weight.

- Flat Saturation

  The flat saturation characteristic of the amplifier ensures positive holding forces on the piston above and below the modulation range without the need for a complex circuit design to achieve this result.

Linear Variable Differential Transformer (LVDT)

The electrical output signal indicating the position of the piston is provided by the LVDT. Typically, it consists of an AC transformer having a single primary coil, but dual opposed secondary coils in series and in axially spaced apart relationship as shown in Figure 12A. The output voltage generated in each secondary coil depends upon the relative position of the indicated highly permeable magnetic core or armature. Thus with the armature centered as shown, the coils cancel each other and net output voltage is very small. At each travel extreme for the armature a maximum AC output is generated. The phase relationship of the output AC voltage to the primary input excitation is different for the two secondary coils and is used to discriminate direction and permit a continuous nearly linear DC output signal indicating piston position, by appropriate signal processing in the electronic test module supplied with the sensor. To assure precise indication of piston position, the transformer must see no other magnetically permeable materials and must not have its output sapped by parasitic eddy currents. This requires that the rest of the piston (other than the armature), the piston sleeve, the piston sleeve closure plug, and the abutting region of the sensor body must not only be non-magnetic but have a high resistivity. In addition, of course, all materials (including those in the coil assembly) must withstand the rigorous engine mounted environment (estimated -65°F to 750°F plus significant vibration). The coil winding is ceramic coated nickel clad copper. It is wound on an Inconel X-750 bobbin spray coated with ceramic. The body is also made of Inconel X-750. The permeable material around the coil is Carpenter Hymu 80 (like the armature). The body is filled with aluminum oxide power. The cable assembly is welded to the body and consists of four type 304L stainless steel wires imbedded in ceramic powder and encased in a .125" O.D. type 347 stainless steel sheath.

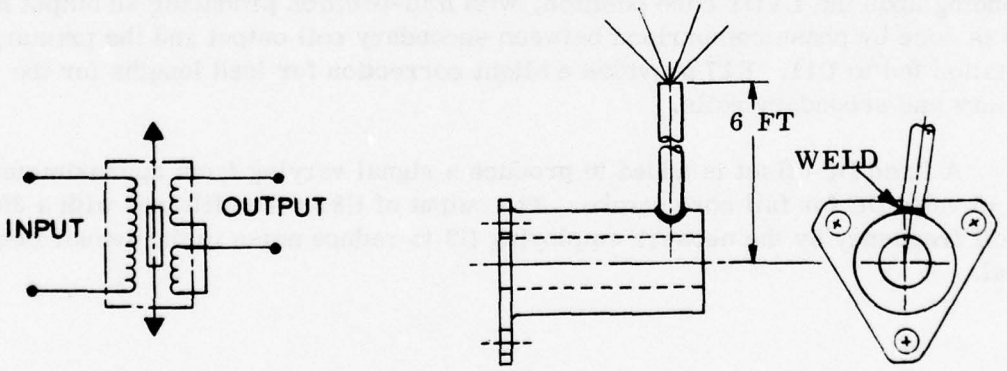

(A) Schematic (B) Coil Proportions (Actual Size)

Figure 12 Linear Variable Differential Transformer (LVDT)

A major factor in achieving the required accuracy is careful design to eliminate or compensate temperature effects on the output voltage. To offset the effect of temperature on the resistance in the primary winding, the test module is designed to supply constant input current rather than voltage.

Electronic Test Module

This unit provides excitation and output signal demodulation for the LVDT. Its functions would normally be included as a part of a main electronic engine control for an advanced technology engine application employing electronic computation. For this reason, the test module is considered as instrumentation rather than a part of the pressure ratio sensor development program. The test module is described as a part of the sensor design description to illustrate the needs of the LVDT for best operation. It is shown schematically in Figure 13. The excitation signal is produced by U1 and U2. U1 is used as a threshold detector that swings either positive or negative depending upon U2, which integrates the output of the threshold detector. Q1 and Q2 form a back to back diode and ensure a constant amplitude triangular wave. The LVDT primary is driven at 10 VAC nominal and 5K Hz frequency by power amplifier U4 with current sense resistor R9 providing feedback via U3's summing junction. The resulting constant current excitation reduces temperature affect on the LVDT. Its output is demodulated by sampling the secondary voltage and a phase shifted (+180°) secondary. These two signals are full wave rectified by U11, which produces either a positive or negative DC output depending upon the LVDT core position, with mid-position producing an output null. This is done by phase comparison between secondary coil output and the primary excitation fed to U11. R17 provides a slight correction for lead lengths for the primary and secondary coils.

A fixed DC offset is added to produce a signal varying from approximately 0 to +5 volts DC for full core stroke. The output of U8 is then filtered with a 30 Hz cut-off frequency by the network employing U9 to reduce noise in the sensor output signal.

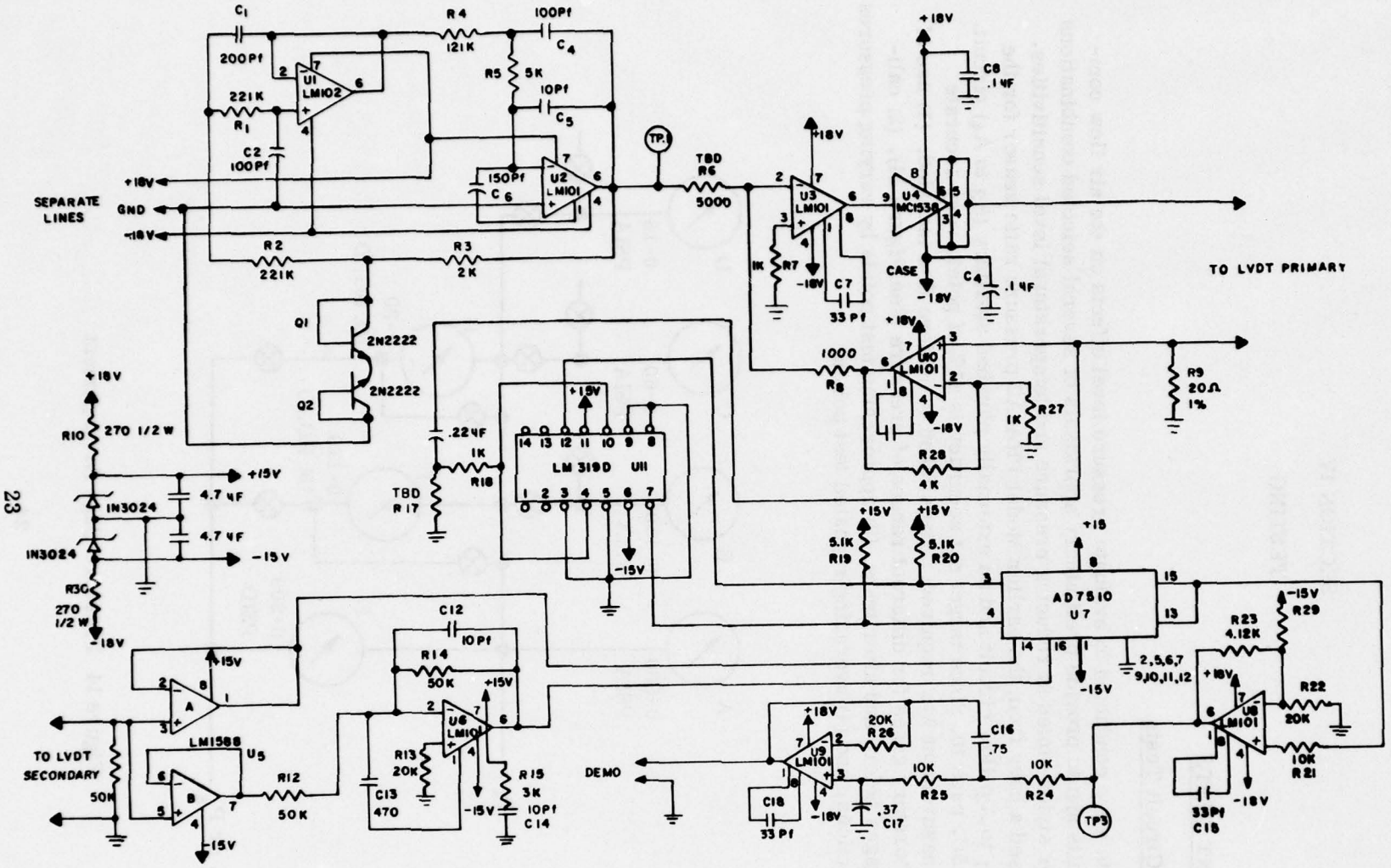

Figure 13 Schematic, Electronic Test Module

SECTION IV

TESTING

COMPONENT TESTS

Computing Circuit Tests

Tests were conducted to evaluate pressure level effects on the air flow computing circuits and to provide preliminary appraisals of several selected combinations of restrictor styles aimed at reducing pressure and temperatural level sensitivities. The tests used a body from the earlier Model PRA-A2 pressure ratio sensor for the primary (A_1 to A_2) flow circuit and an externally plumbed auxiliary (A_3 to A_4) circuit. See Figure 5C, page 10. Since target net accuracy is ±1% of point, very accurate pressure measurement was required. Steps taken to achieve this included: (1) use of different laboratory gages for different ranges of pressure (see Figure 14), (2) calibration of gages before and after tests, (3) approaching test points by varying pressures in both directions, and (4) averaging repeated test points.

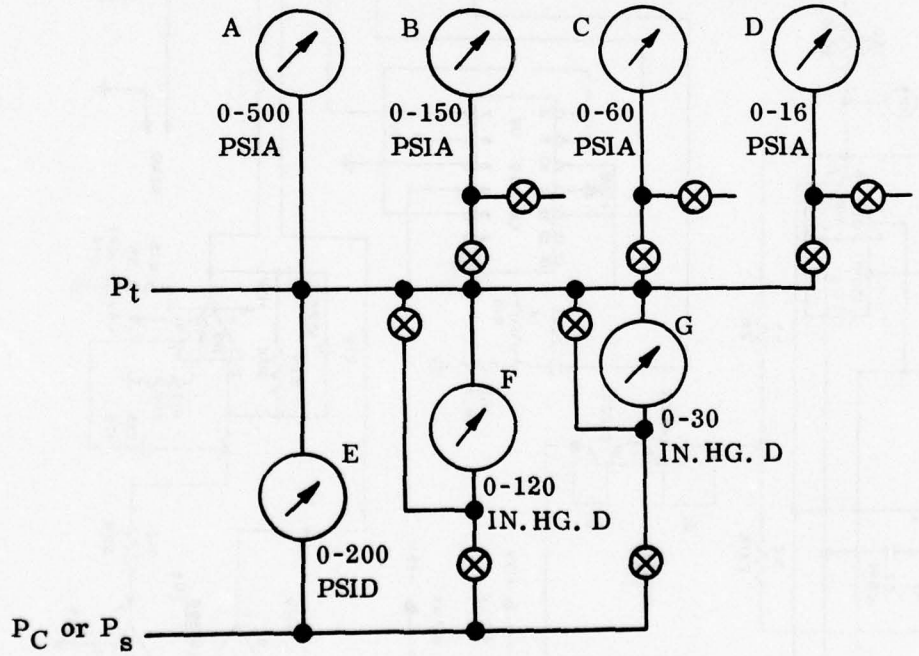

Figure 14 Pressure Gage Arrangement

Test conditions simulated mode "A" and mode "C" operation (Figure 5) for selected nominal values of $(P_t - P_s) / P_t$ and $(P_t - P_{C2}) / P_t$. Restrictors were adjusted for nominal balance of P_{C1} and P_{C2} for these values and for $P_t = 64$ psia. The effect of varying simulated P_t from 6.4 psia to 500 psia while maintaining $(P_t - P_s) / P_t$ was then determined by observing variations in the ratios of the upstream restrictor pressure drops in each circuit (ΔP_1 and ΔP_3) to P_t. As P_t is varied, any variation in $\Delta P_1 / P_t$ for mode "A" and in $(\Delta P_3 - \Delta P_1) / P_t$ for mode "C" (these ratios are nominally the same as $(P_t - P_s) / P_t$) is indicative of equivalent sensor error resulting from flow circuit characteristics.

Because circuit performance indicated a relatively high ratio of P_{C1} to P_{vac} for choked behavior at A_2 (i.e. about 4:1 instead of 2:1), data is plotted to include P_{C1} / P_{vac} as an independent parameter in addition to P_t level. Figure 15 shows that for $P_{C1} / P_{vac} \geq 3.5$ mode "A" exhibits an error band of about $\pm$ 4.77% for a shim type A_1 restrictor (Figure 8D) and about $\pm$ 2.94% for a nozzle and adjusting screw type A_1 restrictor (Figure 8A). Figure 16 shows the behavior of the primary circuit also with the nozzle and adjusting screw type A_1 restrictor, but for

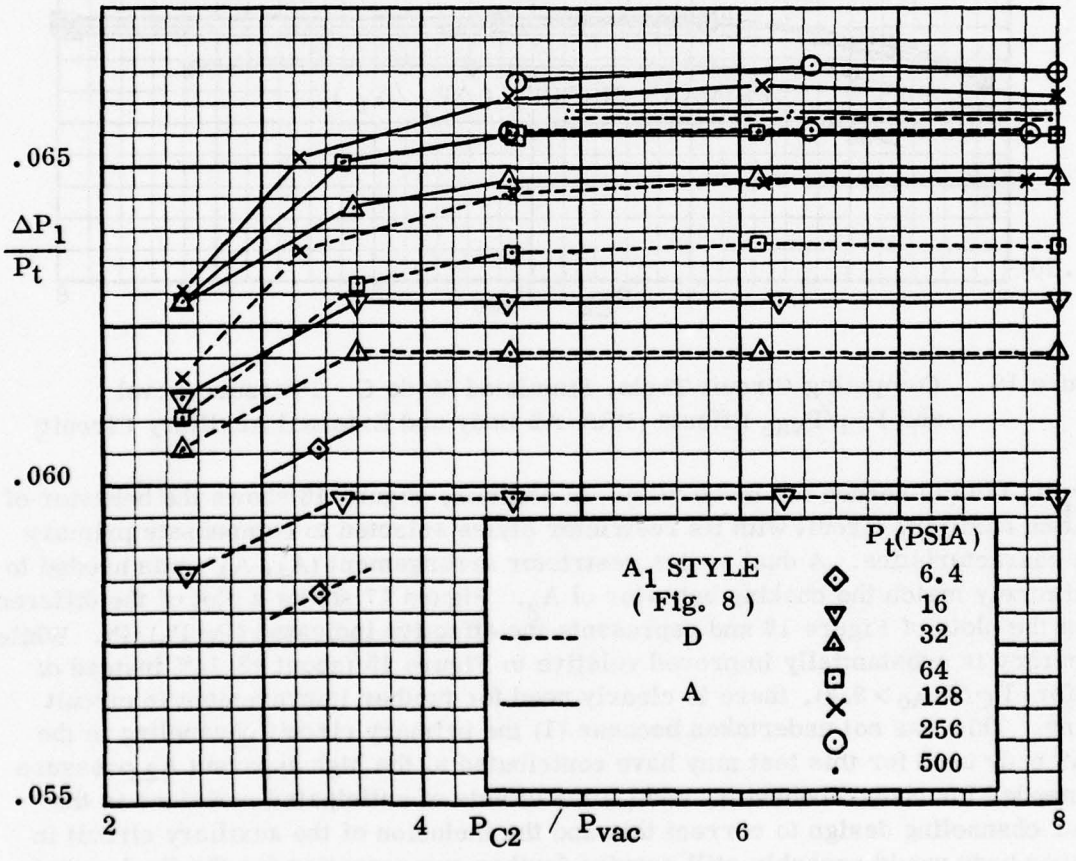

Figure 15 Computing Circuit Tests, Simulated Mode A. Pressure Level and P_{C1} / P_{vac} Effects (PRA-A2 Body)

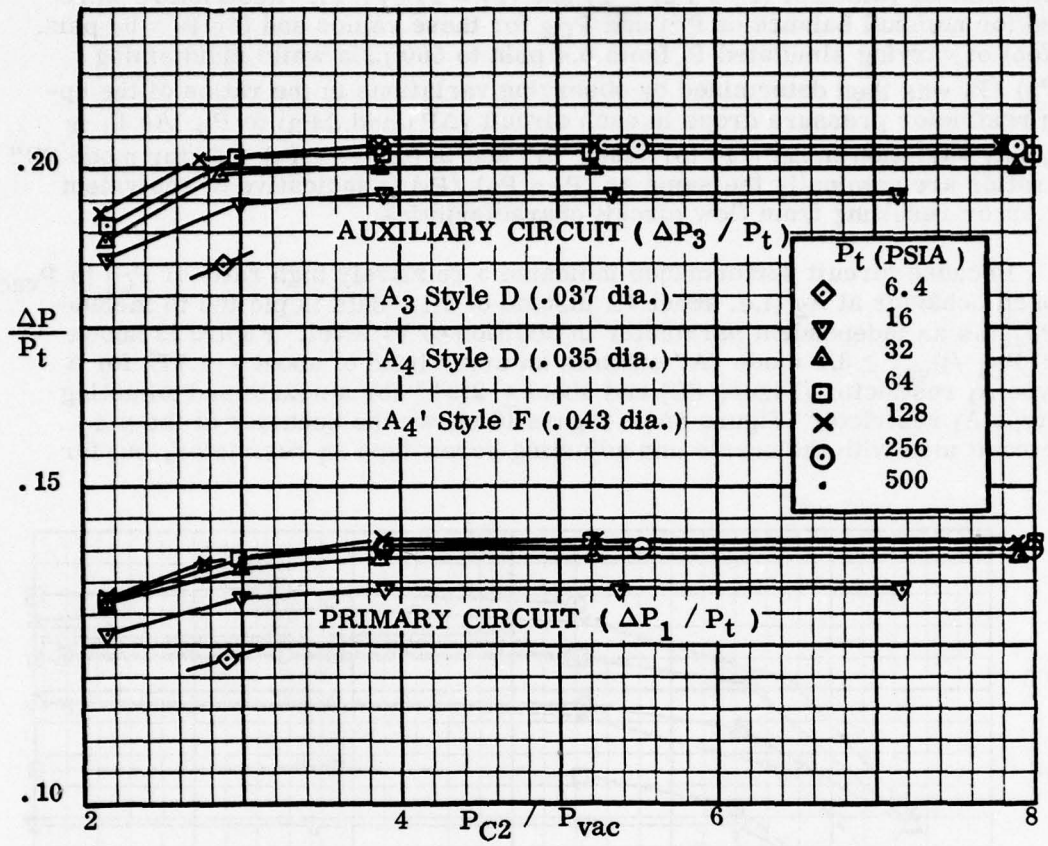

Figure 16 Computing Circuit Tests, Simulated Mode C - Pressure Level and P_{C1}/P_{vac} Effects (PRA-A2 Body and External Auxiliary Circuit)

$\Delta P_1/P_t = .140$ (as needed for mode "C"). In addition, Figure 16 shows the behavior of the mating auxiliary circuit with its restrictor styles selected to compensate primary circuit characteristics. A dual series restrictor arrangement (A_4, A_4') was needed to approximately match the choking behavior of A_2. Figure 17 shows a plot of the difference between the plots of Figure 16 and represents the effective indicated $(P_t-P_s)/Pt$. While the accuracy is substantially improved relative to Figure 15 (about ±2.14% instead of ±2.9% for $P_C/P_{vac} > 3.4$), there is clearly need for further improvement in circuit matching. This was not undertaken because (1) the primary circuit channeling in the PRA-A2 body used for this test may have contributed to the high apparent A_2 pressure ratios needed for choked behavior, and (2) the effects of anticipated revisions in the PRA-A3 channeling design to correct this and the inclusion of the auxiliary circuit in the sensor body would probably still require further compensation for the final restrictor selection. Also, the effects of amplifier and other system characteristics may require compensation by deliberate computing circuit bias in the final sensor design.

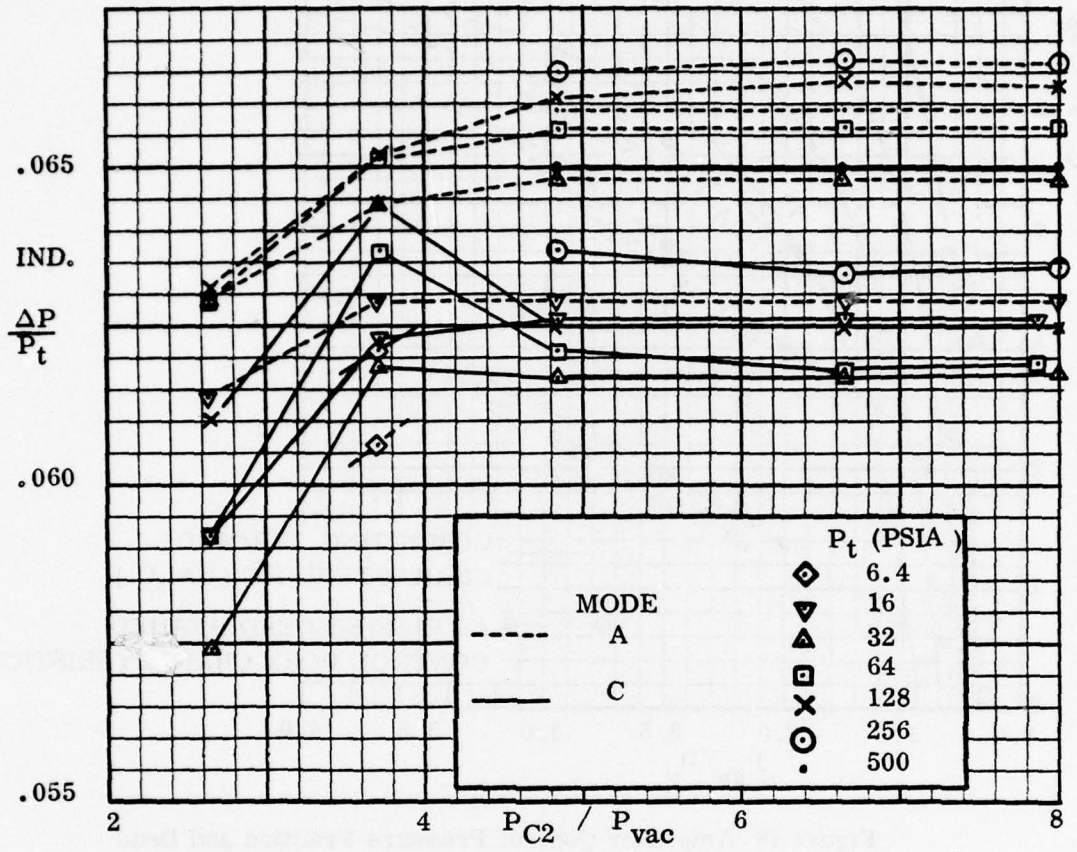

Figure 17 Net Computing Circuit Pressure Level and P_{C1}/P_{vac} Effects - Preliminary Tests

Amplifier Tests

A basic problem associated with burner inlet mach number sensing (Figure 5C) lies in the required relatively high ratio (about .8) of the amplifier control pressure P_{C2} to the amplifier supply pressure P_{as} (P_B' in Figure 7 and approximately equal to P_t). The subscript "as" is used to designate amplifier supply pressure to distinguish it from P_s, or static pressure (as used elsewhere in this report). The solid curves of Figure 18 show the calculated effect this ratio has on the required amplifier control pressure level factor $(P_C - P_v)/(P_{as} - P_v)$ as P_{as}/P_v is varied. To assure adequate amplifier saturated output at extreme altitude it is desirable to operate with a significant fraction of P_{as} available for the amplifier, i.e. with P_{as}/P_v significantly large. The curves indicate that increasing P_{as}/P_v also drastically increases the required control pressure level factor. See also Figure 6B.

The amplifier (see page 18) is designed to operate with zero control port flow at the null condition. The nominal design point control pressure level factor is then determined by blocking the control ports and measuring the dead headed

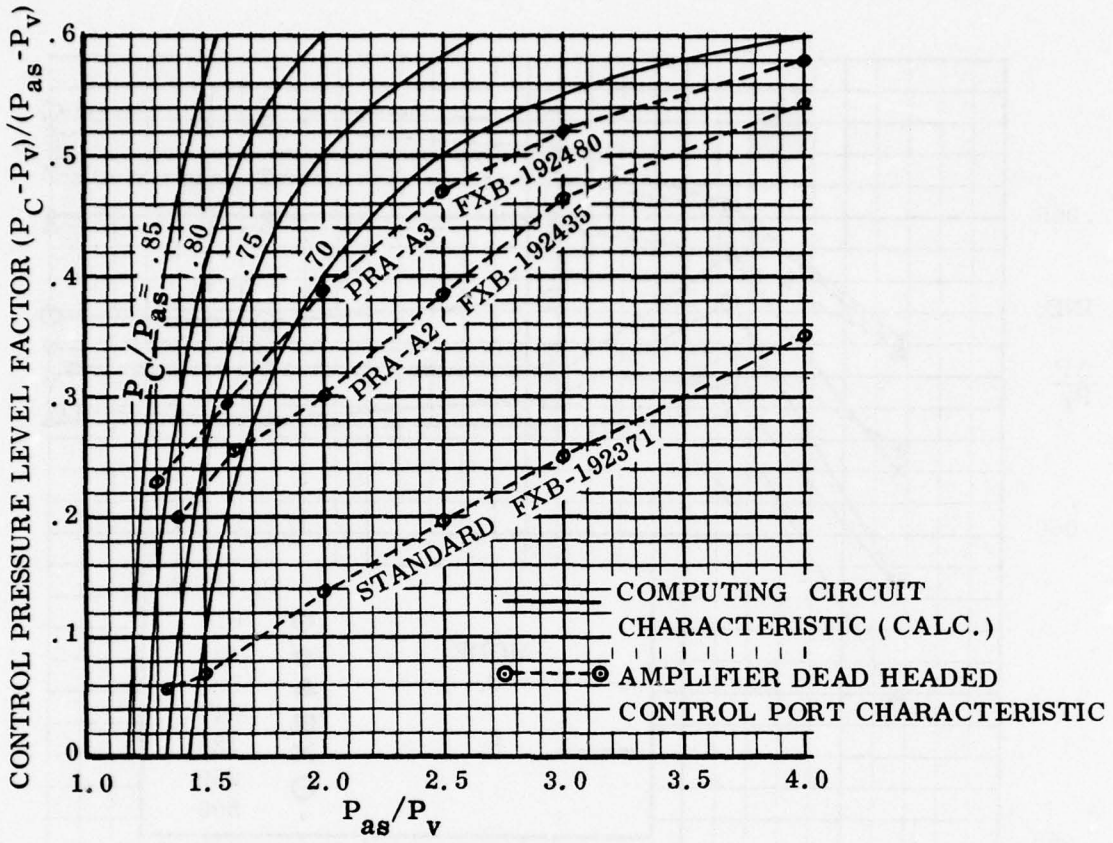

Figure 18 Amplifier Control Pressure Fraction and Dead Headed Control Pressure Level Factor vs. Amplifier Operating Pressure Ratio

pressures there (nominally equal). The lower broken line curve shows the relation of the measured dead headed control pressure level factor to supply to vent pressure ratio for the standard amplifier design. The intermediate broken line curve shows the relation for the modified amplifier used in the PRA-A2 $\Delta P/P$ sensor and the upper broken line curve is for the further modified amplifier used in the PRA-A3 sensor. Modifications essentially consisted in reducing the ratio of the gap between the deflector wall tips and the power jet width (Figure 11) to produce a throttling effect and raise the control pressure level. Intersection of the PRA-A3 amplifier curve with the $P_C = .8\ P_{as}$ computing circuit line occurs at a control pressure level factor of about .25 and a supply to vent pressure ratio of 1.36. Except for the low saturated amplifier pressure output this would be a desirable operating condition. If control pressure level could be reduced from .8 to .75 the amplifier curve would be intersected at a control pressure level factor of about .28 and $P_{as}/P_v = 1.53$.

Figure 19 shows the measured control flow characteristics of the standard amplifier. Note that for the zero control pressure level factor, the curves are nearly flat (infinite input impedance) and control flow is negative (out of the amplifier control port) and very small at low P_{as}/P_v ratios. As the control pressure level factor is increased to .25 and .5, a pronounced slope is developed (lower input impedance) and

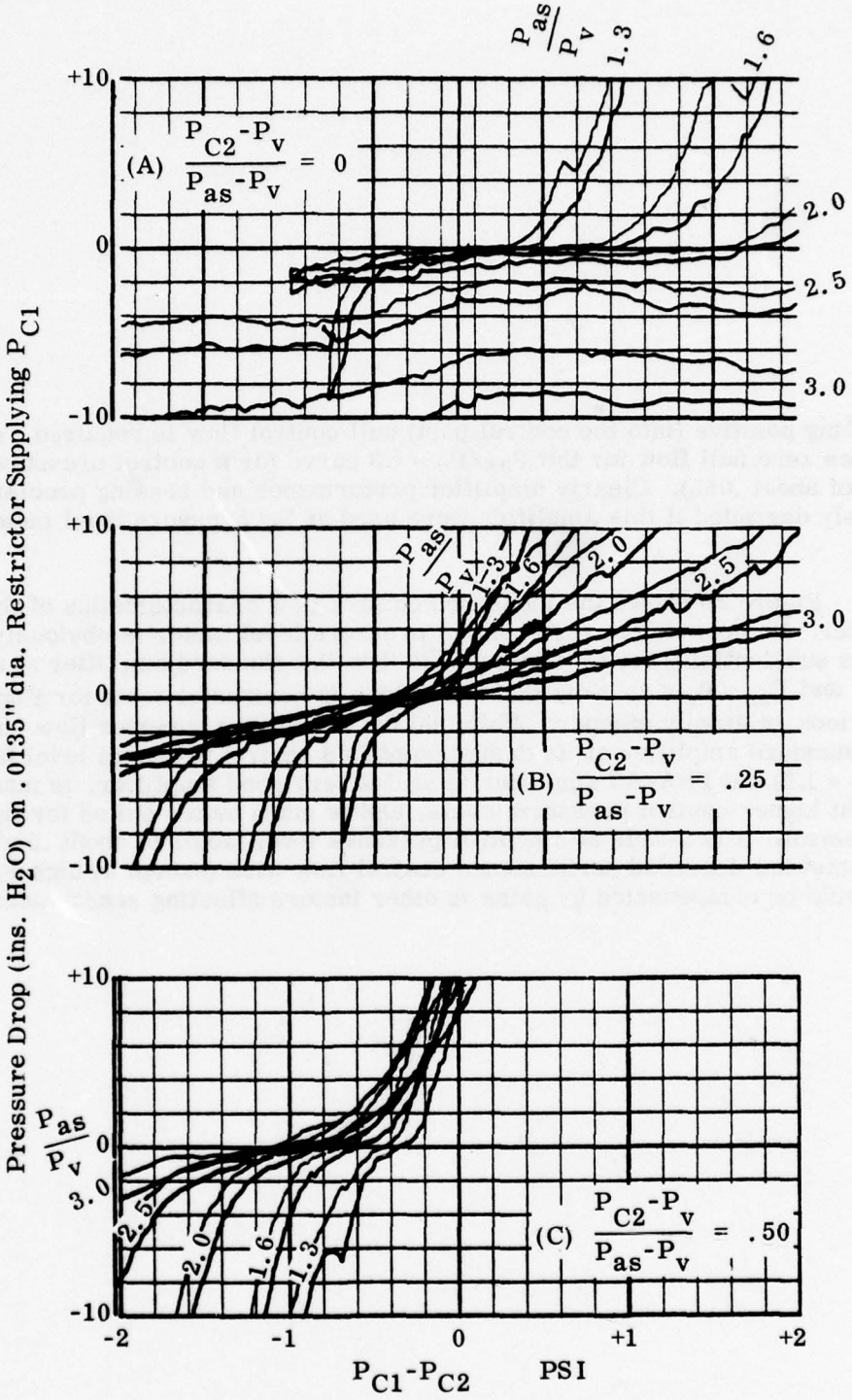

Figure 19 Flow Characteristics, Standard Amplifier (FXB-19237l), Atmospheric Vent

increasing positive (into the control port) null control flow is required. (Figure 18 indicates zero null flow for the $P_{as}/P_v = 1.3$ curve for a control pressure level factor of about .055). Clearly amplifier performance and sensing precision would be seriously degraded if this amplifier were used at P_C pressure level factors approaching .5.

Figure 20 shows the measured control flow characteristics of the PRA-A3 amplifier. Its behavior at zero control pressure level factor is obviously poor. It exhibits substantially better performance than the standard amplifier at a factor of .25, and $P_{as}/P_v \leq 2$. Note that the change in horizontal scale for Figure 20 makes *slopes look relatively steeper.* While not developing the superior flow characteristic of the standard amplifier at its design point (.08 control pressure level factor and $P_s/P_2 = 1.6$) the PRA-A3 amplifier is still a very good amplifier, is manifestly better at higher control pressure levels, and is much better suited for the PRA-A3 requirement. It is usable at a control pressure level factor of about .5 although with somewhat degraded performance control flow wise (except at high P_{as}/P_v). This could be compensated by gains in other factors affecting sensor accuracy.

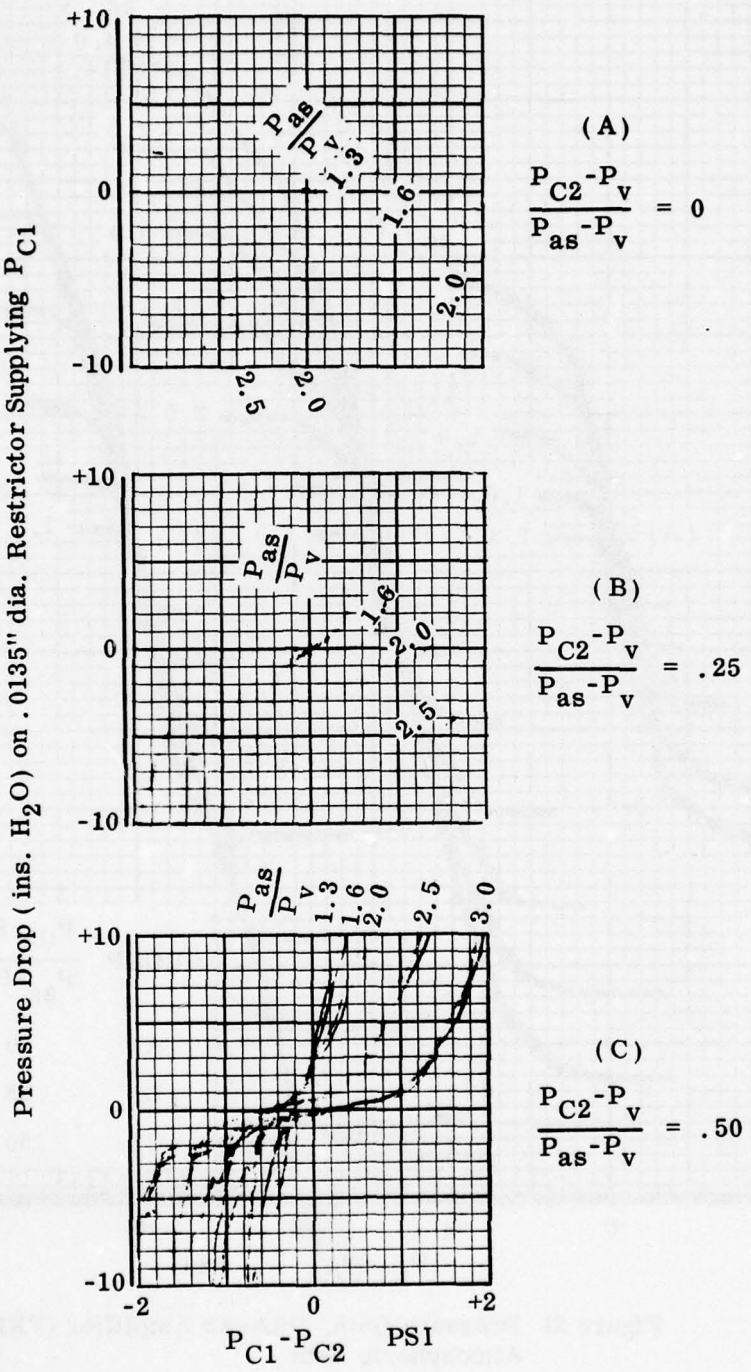

Figure 20 Flow Characteristics, PRA-A3 Amplifier (FXB-192480) Atmospheric Vent

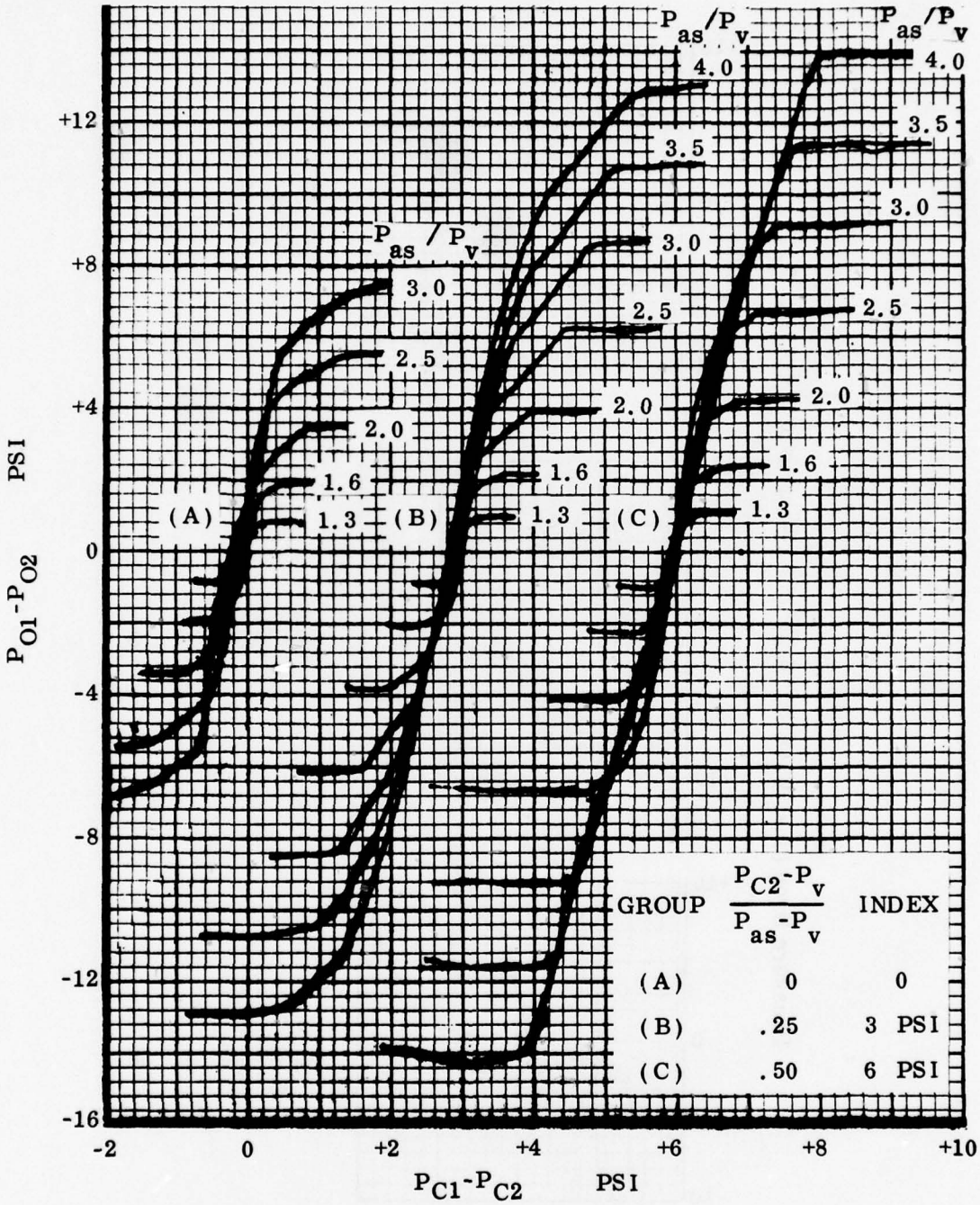

Figure 21 Pressure Gain, PRA-A3 Amplifier (FXB-192480), Atmospheric Vent

Figure 21 shows the pressure gain characteristics of the PRA-A3 amplifier at the same conditions (P_v = Atmos.) as for Figure 20. Gains are excellent even at a .5 control pressure level factor, and exceed 10 at low P_{as}/P_v ratios. Flat saturation is exhibited. Note that the horizontal scale is the same as for Figure 20 and shows that most of the flow excursions in that figure occur only after pressure

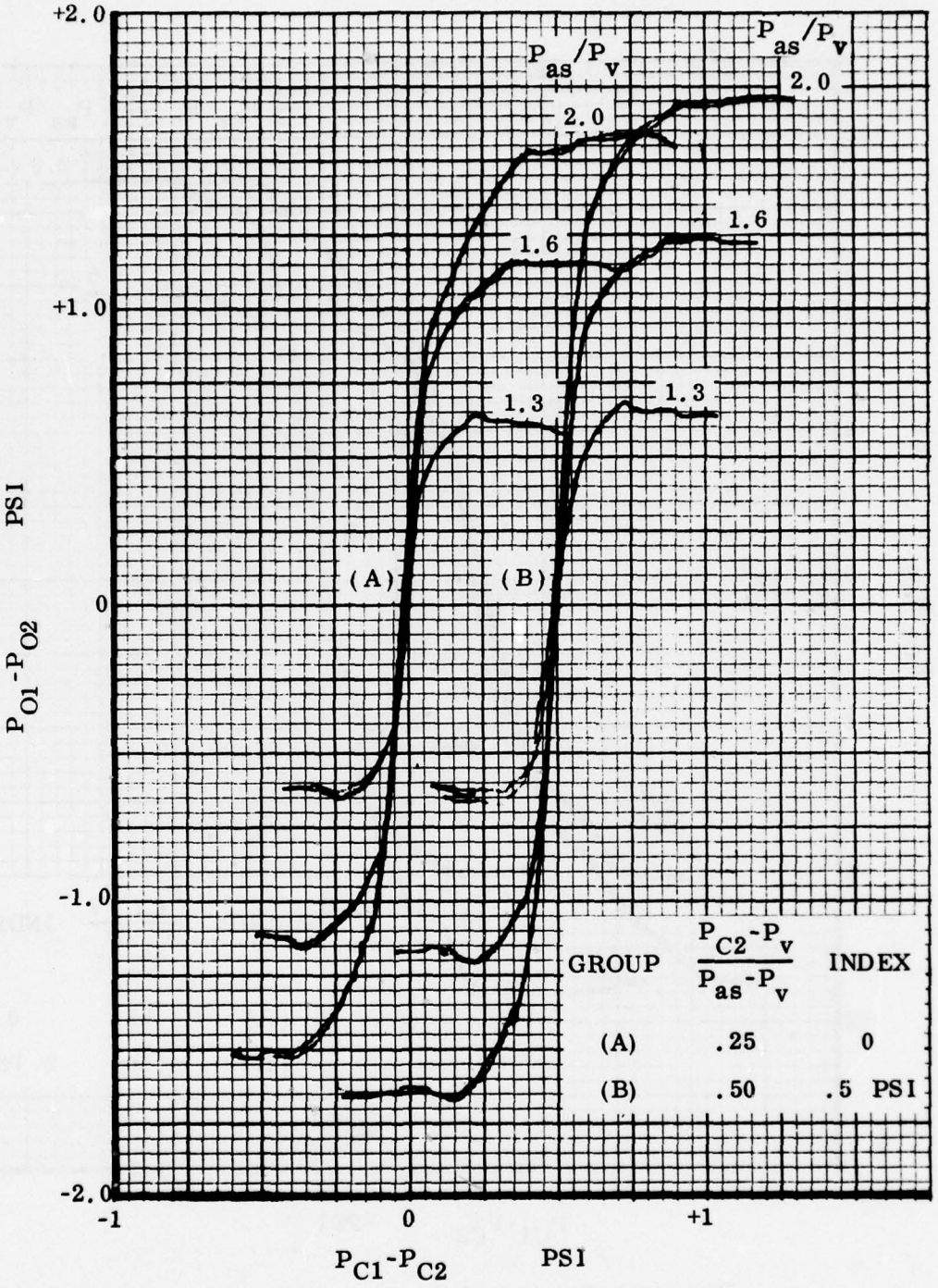

Figure 22 Pressure Gain, PRA-A3 Amplifier (FXB-192480), P_{as} = 12 psia

saturation has been reached. Figures 22, 23, and 24 show the effect of supply pressure level on the pressure gain curves. Although the shapes of the curves as saturation is approached vary, pressure gain is only slightly affected - falling off

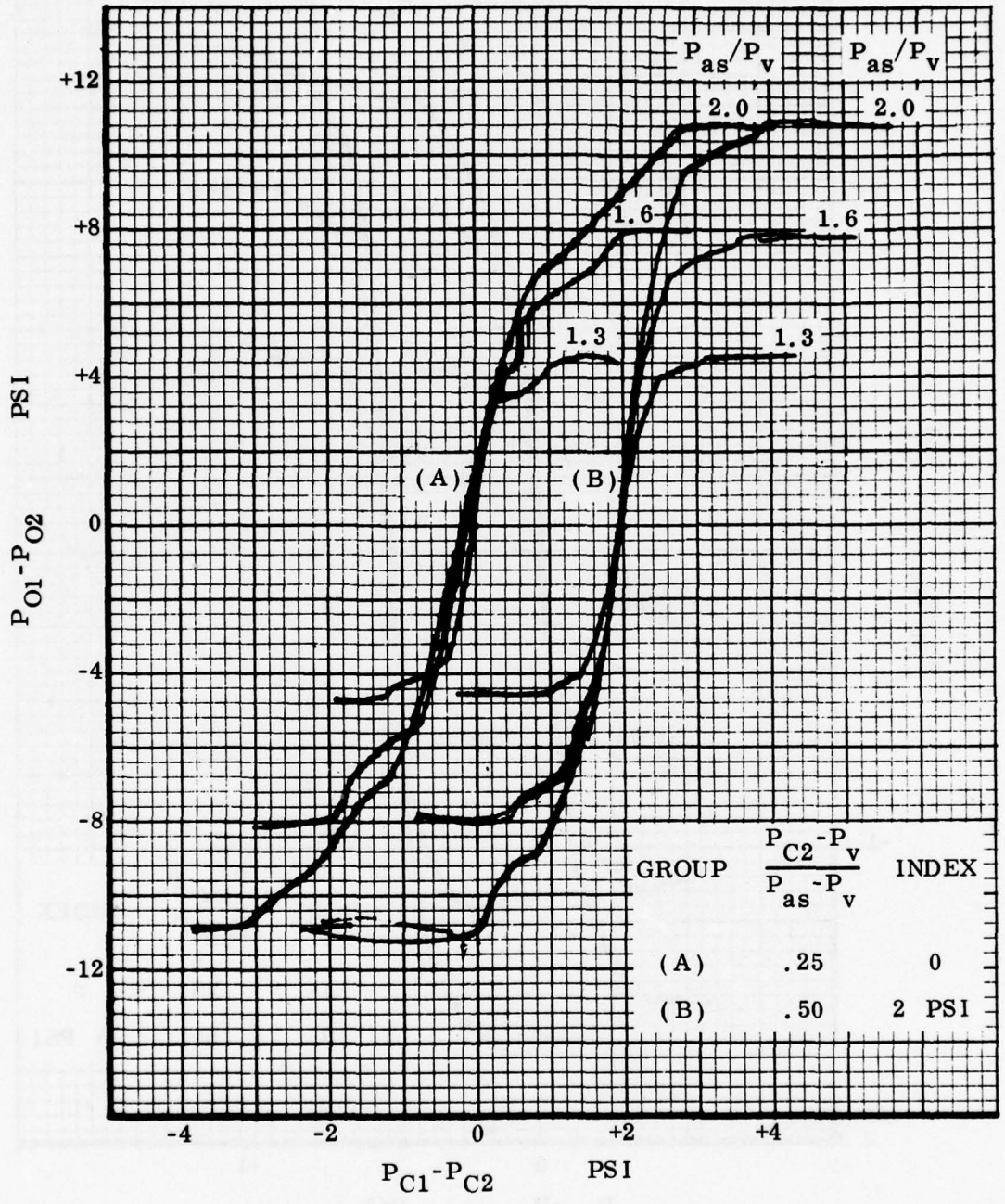

Figure 23 Pressure Gain, PRA-A3 Amplifier (FXB-192480), P_{as} = 64 psia

somewhat at higher pressures (which is desirable). The selected amplifier is eminently suitable for the PRA-A3. Final selection of control and vent pressure levels must be made in calibrating the complete sensor for best over-all accuracy.

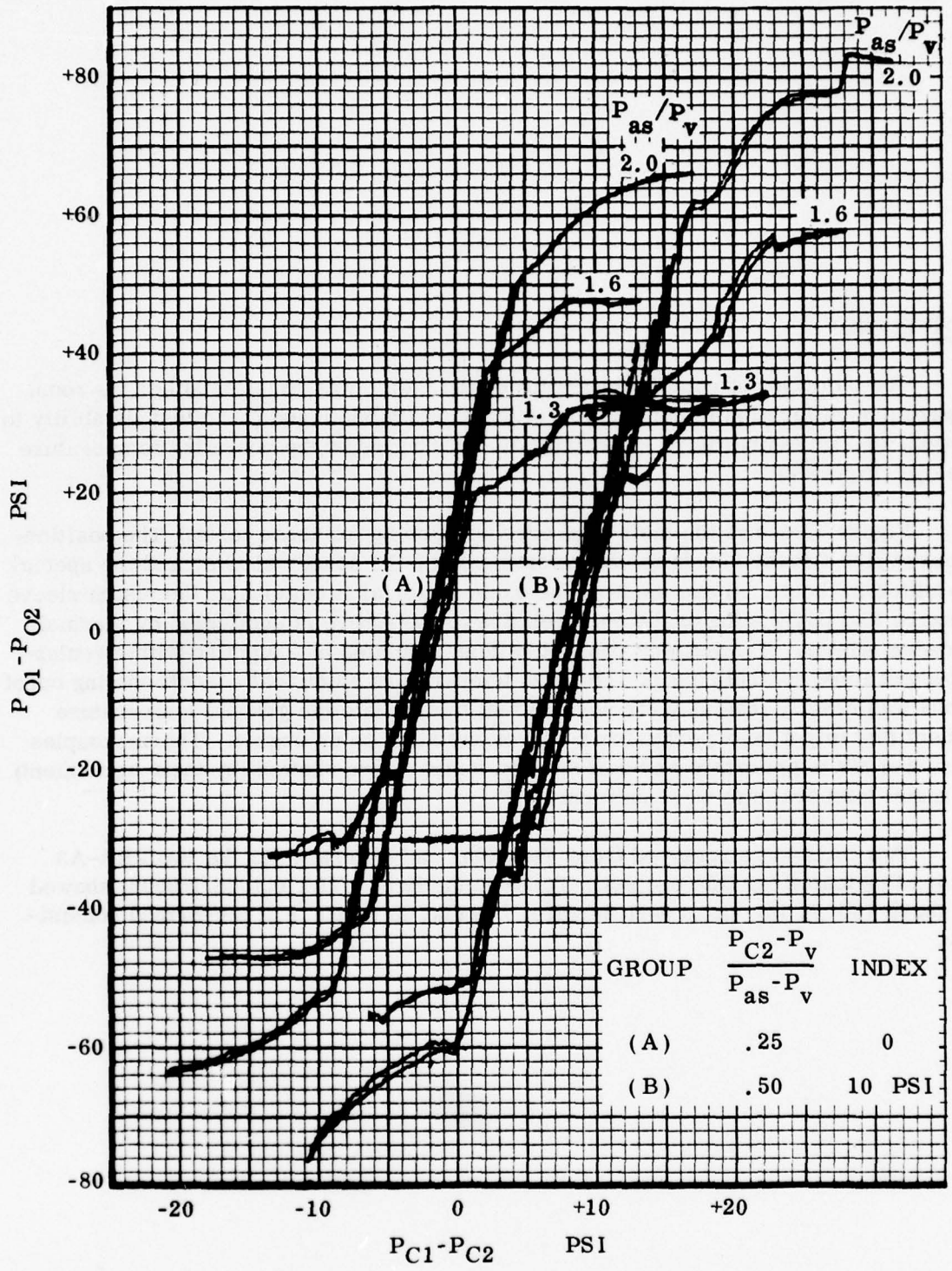

Figure 24 Pressure Gain, PRA-A3 Amplifier (FXB-192480), P_{as} = 500 psia

LVDT Tests

The objective of component testing of the LVDT was to (a) establish its room temperature calibration in conjunction with the test module and (b) to test its ability to function, and its temperature sensitivity over the range of the operating temperature envelope (Figure 2).

Figure 25 shows the method of core positioning for these tests. The positioning screw, its threaded bushing, the retaining pins, the spacer sleeve, and the special stop button in the piston are made of the same material (titanium) as the piston sleeve to ensure that positioning of the core relative to the sleeve is unaffected by thermal expansion effects. Testing was conducted in an insulated box supplied with circulating temperature controlled air. The high temperature electrical conduit coming out of the box was heavily insulated for several feet to simulate the gradual temperature gradient that might be expected for a sensor installed on an engine. Thermocouples measuring air temperature and coil surface temperature showed (by their agreement) that metal temperatures were uniform.

Two coils were received from Pickering and Company for the two PRA-A3 Sensors fabricated for this project. Tests on the first LVDT coil (S/N 0002) showed that above 700°F, its output went to zero, but that up to 675°F it performed consistently.

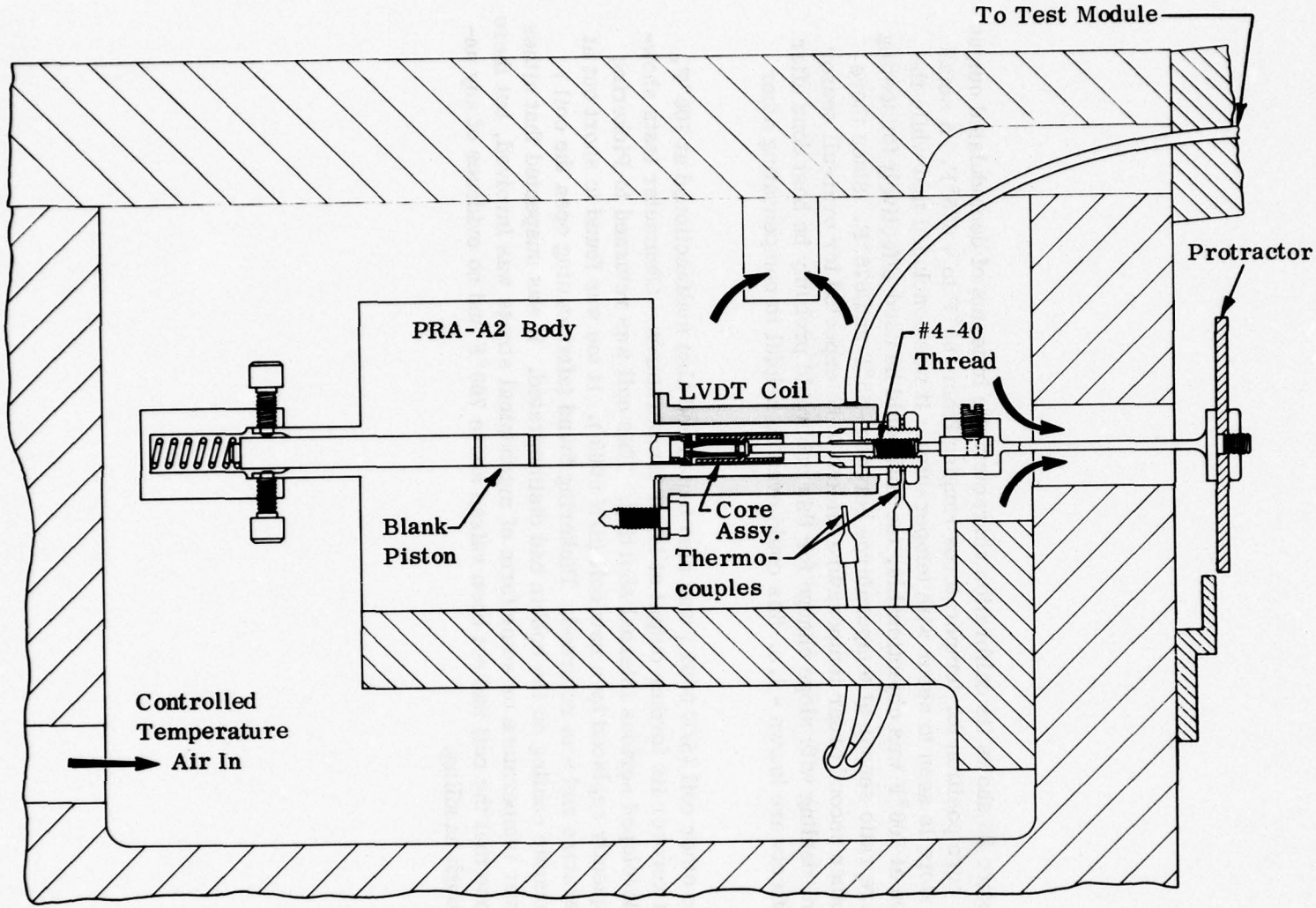

Figure 25 LVDT Test Arrangement

Figure 26 shows its calibration characteristic in terms of demodulated output voltage vs core position for temperatures ranging from -65°F to + 675°F. A small change in slope is seen to occur with temperature. It was concluded that while the malfunction at 700°F was objectionable, the coil could be used effectively for testing the pressure ratio sensor at temperatures between -65°F and 675°F. Since there would be other second order temperature effects to be expected for over-all sensor calibration, dealing with slope change for this one would probably be best done after over-all effects are known - i.e. this could even be helpful in compensating other effects.

The other coil (S/N 0001) was also tested and also malfunctioned at 700°F, but did not recover its former output at lower temperatures. Ohmmeter tests showed it had developed serious internal shorting. This coil was returned to Pickering and subsequently replaced by a new coil (S/N 0003). It too was found to short out at high temperature and was returned. Pickering found (after cutting open the coil) that the ceramic coating on the bobbin had disintegrated. It was suspected that either extreme over temperature or some form of mechanical stress was involved, but there was evidence that the coil had not been raised above 700°F and no evidence of any unusual or rough handling.

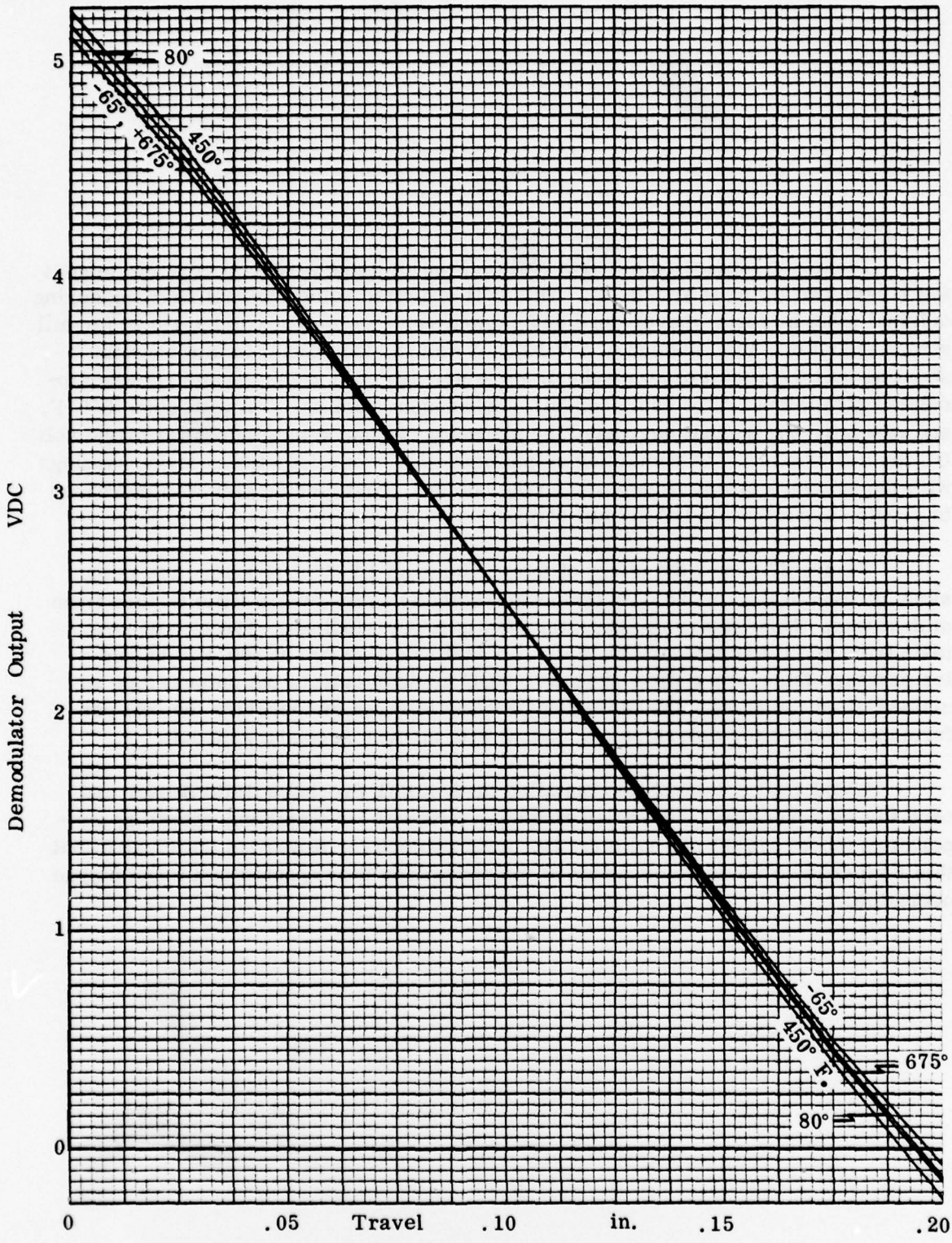

Figure 26 Temperature Effects, LVDT Coil S/N 0002

Pickering fabricated a fourth coil (S/N 0010) using a special ceramic to coat the bobbin and firing it at 1400°F. This coil exhibited some internal shorting during original tests at room temperature and showed very low output voltage range for full stroke (about 0.5 VDC instead of 5 VDC). It was suspected that in this case the shorting was the result of atmospheric moisture sealed into the ceramic powder insulated high temperature cable conduit. Subsequent opening, drying at about 350°F, and resealing the conduit corrected the shorting. Output range increased to one volt DC for full stroke. The remaining output reduction was attributed to fewer windings with the heavier ceramic insulation on the bobbin. Test module gain was increased to provide about 6 volts DC for full stroke.

Figure 27 shows the effect of temperature on LVDT S/N 0010. The output slope is seen to vary more with temperature and to cross over a little farther from mid-stroke. This change is also attributed to fewer windings. The curves cover tests from room temperature to 750°F. A test was also run at 800°F. At this temperature there was a drop of about 2 VDC in mean output, but output slope remained about the same. On subsequent cooling to room temperature the coil performance completely deteriorated, ending with an open secondary circuit.

LVDT Coil S/N 0002 was installed on S/N 001 Pressure Ratio Sensor and used for its bench tests and engine running. Although its maximum operating temperature (about 675°F) did not meet the design objective, it was not anticipated that this temperature would be exceeded at the sensor for the expected test stand engine operation.

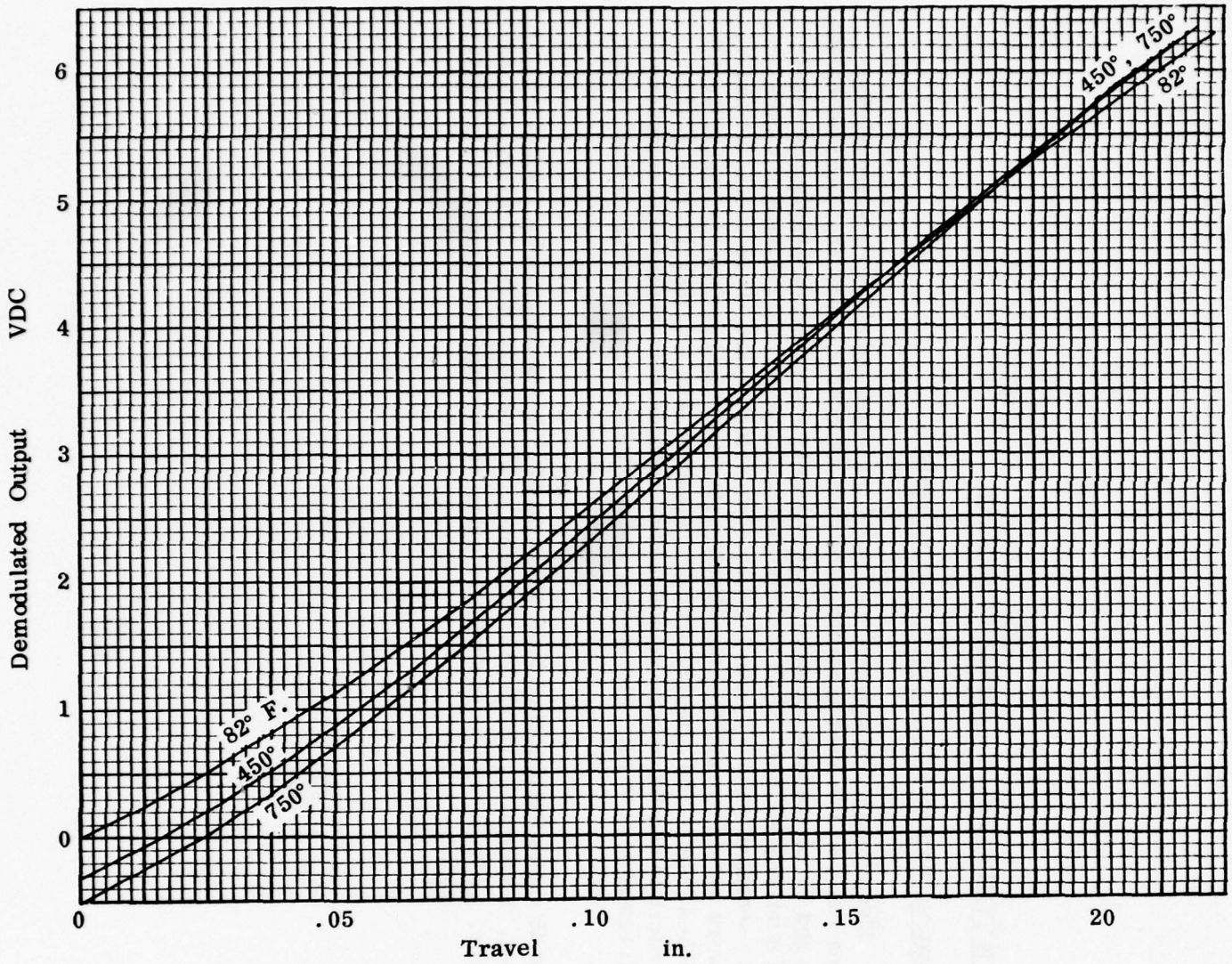

Figure 27 Temperature Effects, LVDT Coil S/N 0010

BENCH TESTS OF THE COMPLETE SENSOR

Calibration and Pressure Level Sensitivity Tests

The primary computing circuit was first optimized (A1 style selected-See Figures 7 and 8) for least pressure level sensitivity of P_{C1} with the amplifier blocked out and the piston held centered. The auxiliary computing circuit then was optimized similarly for best match of the pressure level and relative back pressure (P vac) sensitivities of P_{C2} and P_{C1}, by style selection and sizing of R3, R4 and A4. This work was an extension of the circuit tests, described earlier, but using the actual PRA-A3 unit. The complete functioning sensor then was tested for pressure level effect on sensing accuracy, and further changes were made in the computing circuit restrictors to adjust the setting and minimize over-all pressure level sensitivity.

Figure 28 shows the pressure level effect on $\Delta P_1/P_t$ and $\Delta P_3/P_t$ for fixed $(P_t-P_s)/P_t$ input. Note that A_2 requires a pressure ratio in excess of four to exhibit choked behavior. With R4 and A4 in series as a dual downstream restriction, the auxiliary

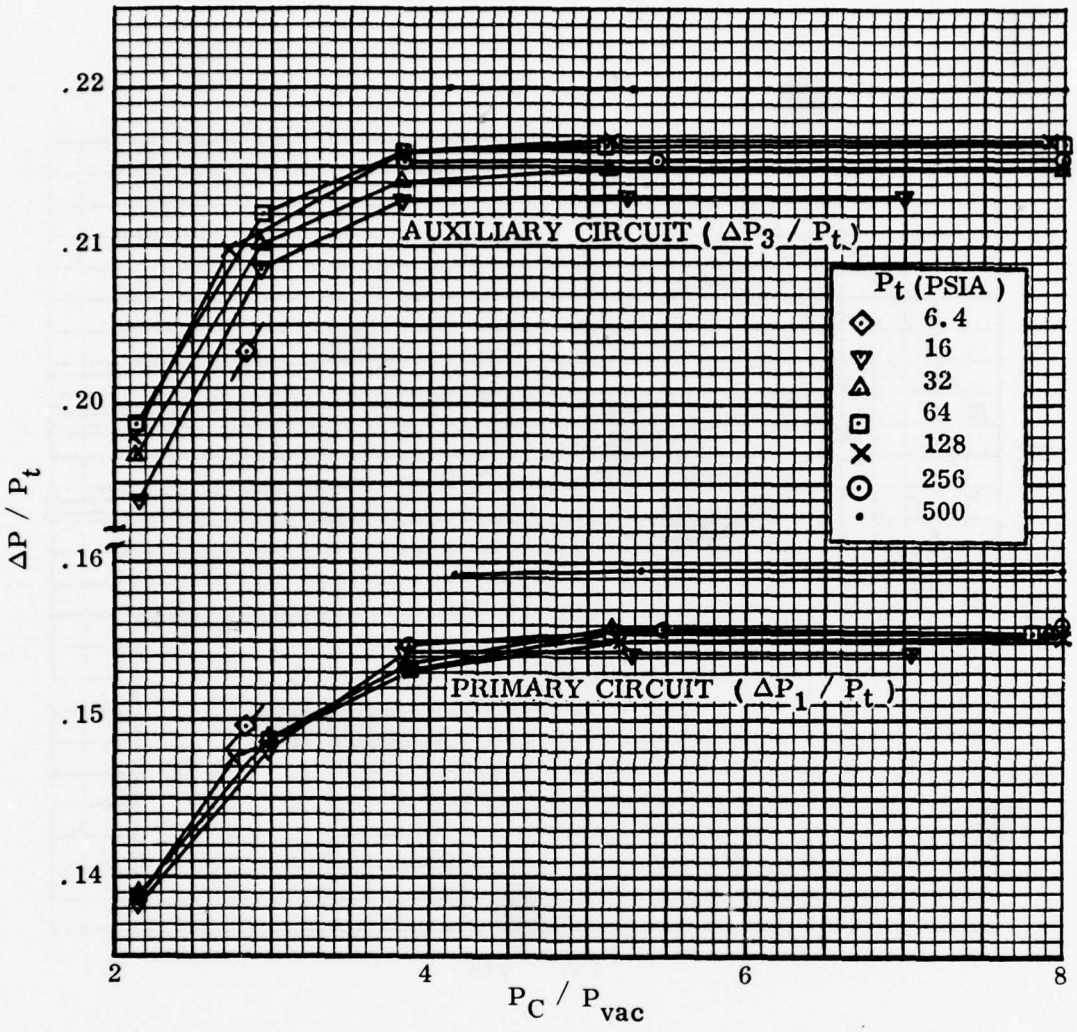

Figure 28 Pressure Level and P_{vac} Effects, Primary and Auxiliary PRA-A3 Computing Circuits.

circuit shows a similar characteristic. Figure 29 shows the effect of pressure level and downstream restrictor pressure ratio on the net indicated pressure ratio for computing circuits with fixed $(P_t - P_s)/ P_t$ input.

In Figures 30 and 31 plotting board traces of test module output DC voltage versus $P_t - P_s$ for several P_t levels illustrate pressure ratio sensing with the selected calibrating restrictors (Table 2). The traces are run in both directions to show any sensor hysteresis. The hysteresis is seen to be negligable. Figure 32 shows the room temperature calibration of the sensor by indicating the required ratio of $P_t - P_s$ to P_t to produce a fixed output voltage of 3 volts DC (approximately mid-stroke) for varying P_t levels.

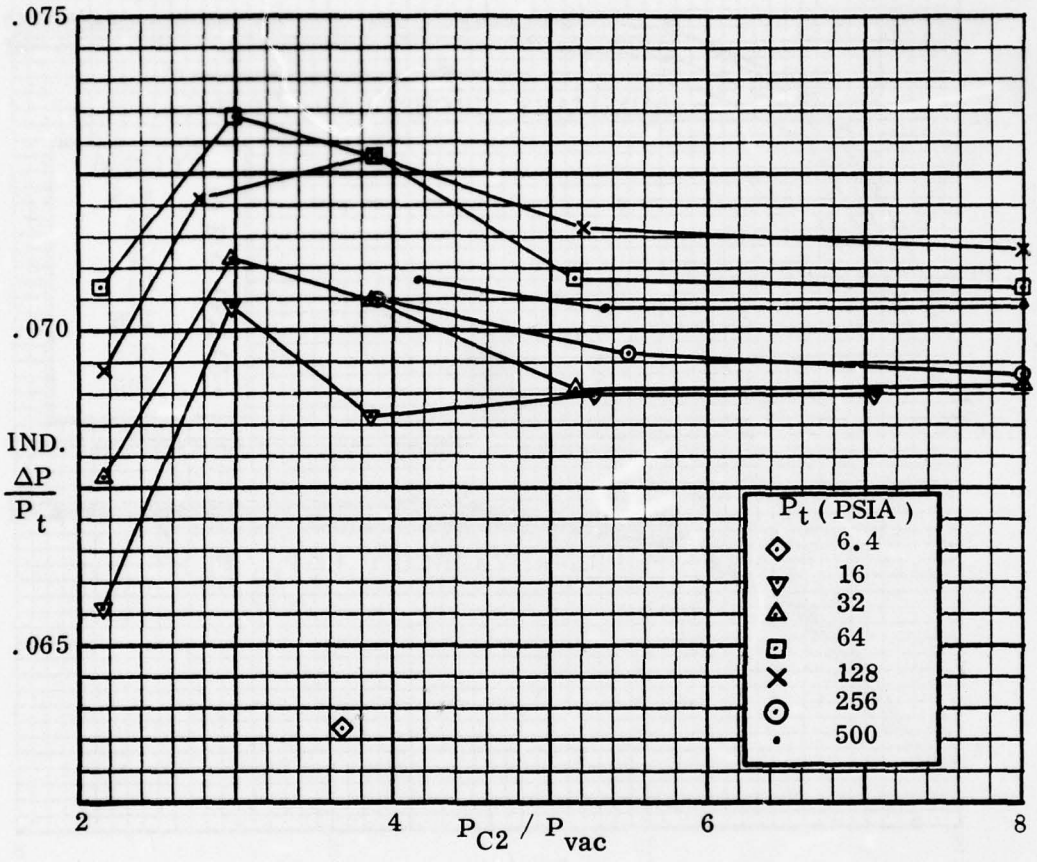

Figure 29 Pressure Level and P_{vac} Effects on Net Indicated $\Delta P/P$, PRA-A3 Computing Circuits

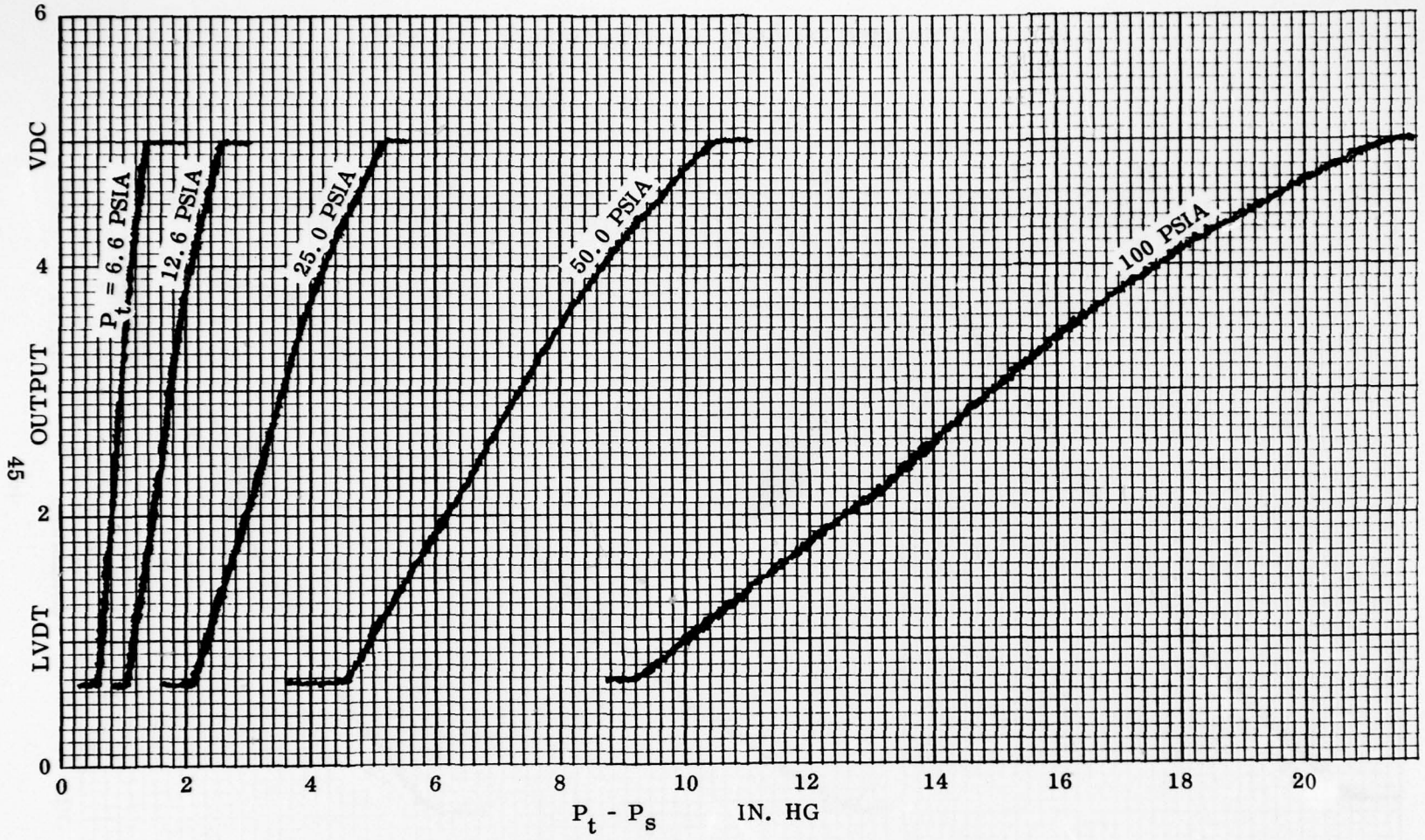

Figure 30 PRA-A3 Output vs P_t-P_s for Different P_t's

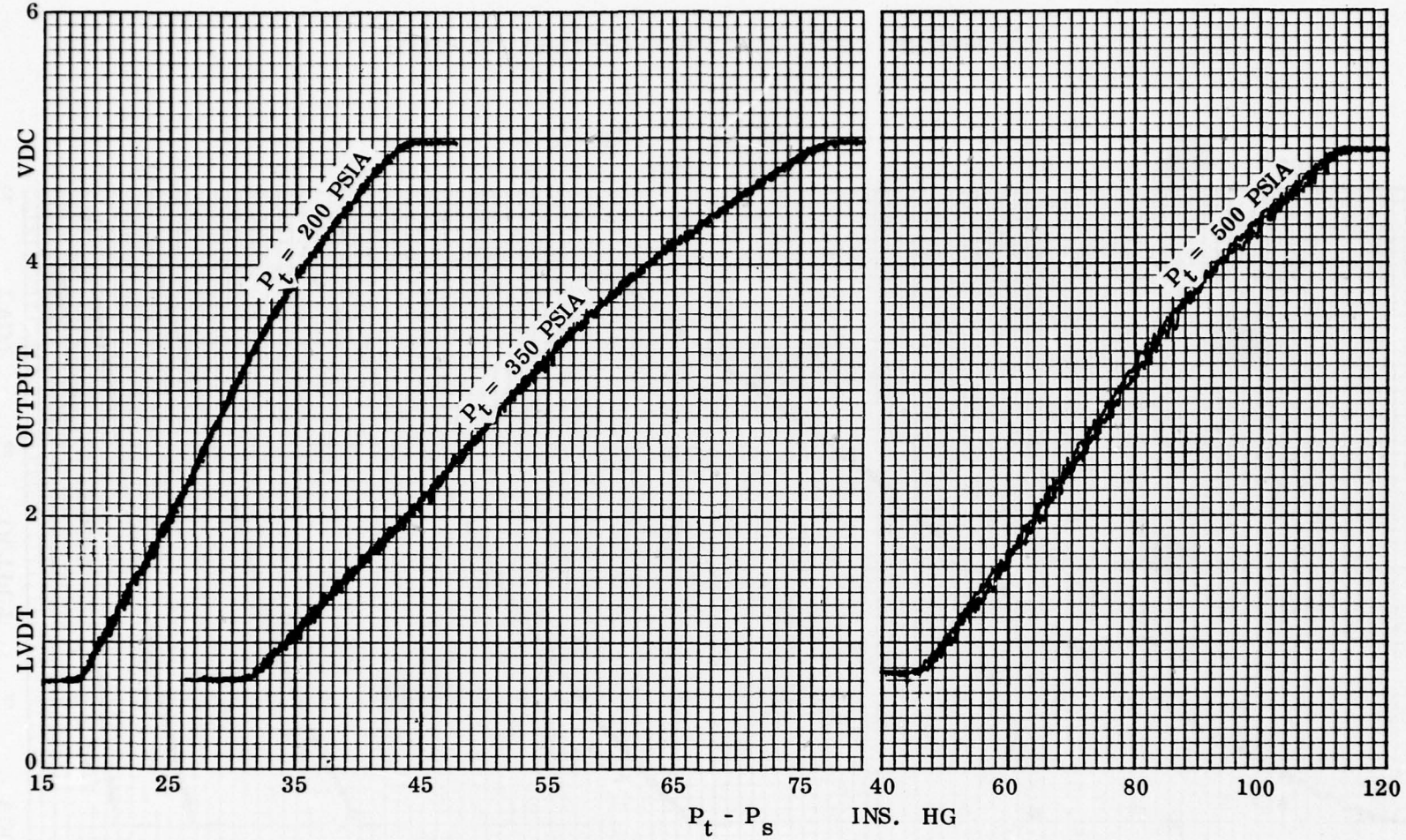

Figure 31 PRA-A3 Output vs P_t-P_s for Different P_t's (Cont'd.)

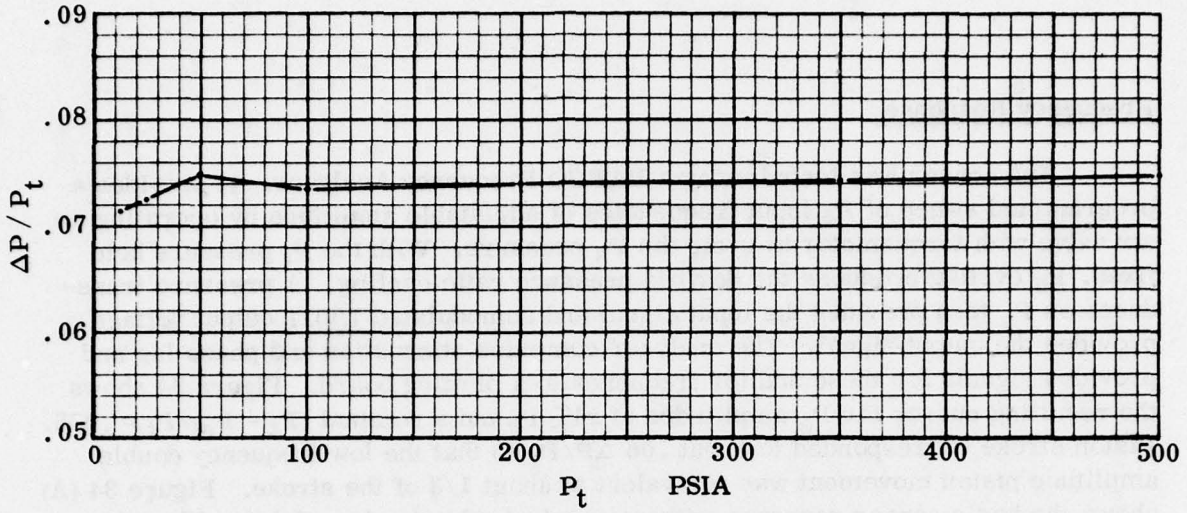

Figure 32 Required $(P_t - P_s) / P_t$ for 3VDC Output vs P_t

Temperature Tests

Figure 33 indicates the effects of both temperature and pressure on the pressure ratio needed to produce 3 volts DC output. These effects are seen to be small enough to make it feasible to accurately compensate for them in the electronic engine control.

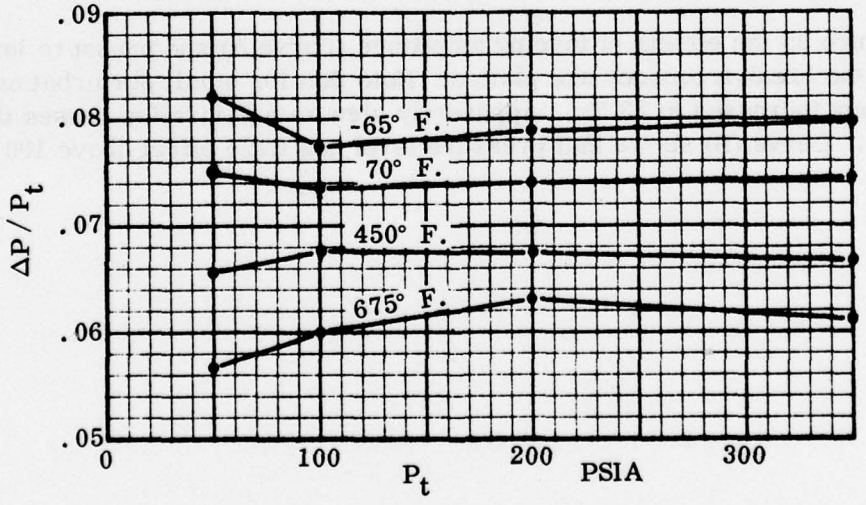

Figure 33 Required $(P_t - P_s) / P_t$ for 3 VDC Output vs P_t for Different Operating Temperatures.

Frequency Response

The sensor was tested using a BAFCO Frequency Analyzer. It provides a programmed sweep of P_S input frequencies of adjustable amplitude by operating an air valve with torquemotor to cycle the P_S pressure. With the P_t pressure held fixed, P_S cycling produces the desired pressure ratio cycling. A pressure transducer on P_S then provides the input signal and demodulated LVDT output voltage provides the output signal. The analyzer computes attenuation and phase lag and provides signals for these and for frequency to a plotting board. Figure 34 shows the resulting curves for P_S amplitudes of $\pm 1\%$ P_t and a nominal $(P_t - P_S)/P_t = .075$. Piston stroke corresponded to about $.06\ \Delta P/P_t$ so that the low frequency double amplitude piston movement was equivalent to about 1/3 of the stroke. Figure 34 (A) shows the basic sensor response without constraint by the demodulator filter for $P_t = 100$ psia. Response is seen to be well damped with a break frequency of about 30 Hz. In 34 (B) the demodulator filtering frequency was lowered to a nominal 30 Hz, resulting in a lowering of the net sensor response to a break frequency of about 20 Hz. It is considered impractical to attempt to use a higher response than this and, indeed, it may be necessary to filter the output to a lower frequency because of fluctuation in the P_t and P_S pressures supplied by the engine. Changes in engine response with altitude are expected to decay in a fashion similar to the sensor (Curve C). The slower sensor response at low P_t (high altitude) should be adequate for closed loop control.

In Figure 35 the effects of forcing amplitude (Curve A) and pressure level (Curve B) on the break frequency are plotted. Note that for small perturbations, break frequency increases to 23 Hz. Apparently slew rate saturation causes the sloping curve. Curve (B) shows that pressure level has little effect above 100 psia.

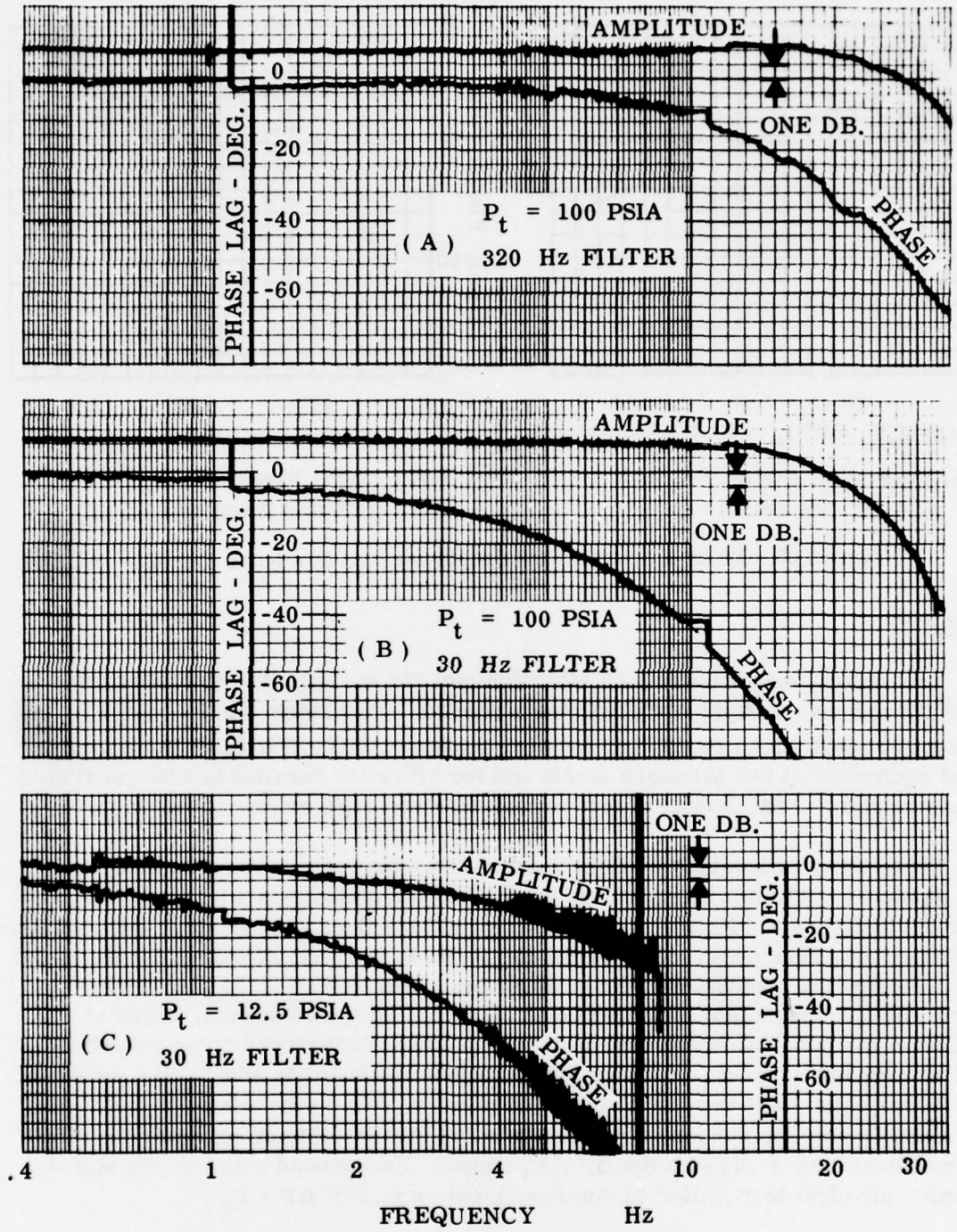

Figure 34 Frequency Response Characteristics

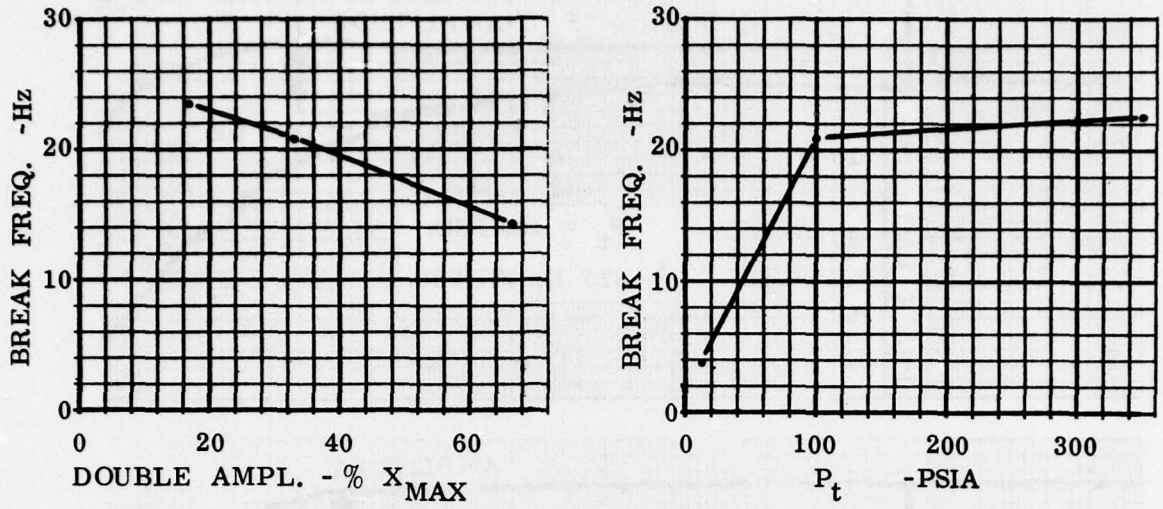

(A) Equivalent Piston Travel (P_t = 100 PSIA)

(B) Total Pressure (Double Ampl. = 33 % X_{max})

Figure 35 Break Frequency vs Amplitude and Pressure Level

Vibration

The sensor was mounted on a vibration test rig and supplied with air pressures that produce a normal centered piston position (mid range $\Delta P/P_t = .075$). Vibration sweeps from .5 Hz to 1000 Hz were made per MIL-STD-810C for engine mounted equipment at two pressure levels and for vibration parallel to and transverse to the piston axis. Test module output voltage was recorded on an oscillograph.

There was no discernible effect of vibration transverse to the piston axis. Figure 36 shows the effect for vibration parallel to the piston axis with P_B and P_t at 60 psia and at 200 psia. No effect was apparent at less than 5 Hz or more than 150 Hz. Maximum effects were observed at 14 Hz and 50 Hz in the form of output $\Delta P/P_t$ signal ripple at the forcing frequency. For 60 psia, the effect was as if the piston were making a relative sinusoidal movement of ± .0033" at both frequencies, which is equivalent to a sinusoidal error indication of ± 1.21%. Background noise was about equivalent to ± .0011" or ± .4% signal perturbation. At 200 psia and 14 Hz, the effect was as if the piston were moving ± .0024" or about ± .89% on the $\Delta P/P_t$ signal. At 200 psia and 50 Hz, the sensor output perturbation increased to an equivalent ± .0026" piston movement, or ± .95% on the $\Delta P / P_t$ signal. Background noise on the signal was about equivalent to ± .0016" piston movement or ± .57% $\Delta P / P_t$.

At low frequencies, the sensor is seen to be able to attenuate essentially all of the forcing amplitude by closed loop effect. At 14 Hz, it attenuates to about 7% of the effective .100" forcing amplitude for 60 psia and about 5% for 200 psia. At 50 Hz,

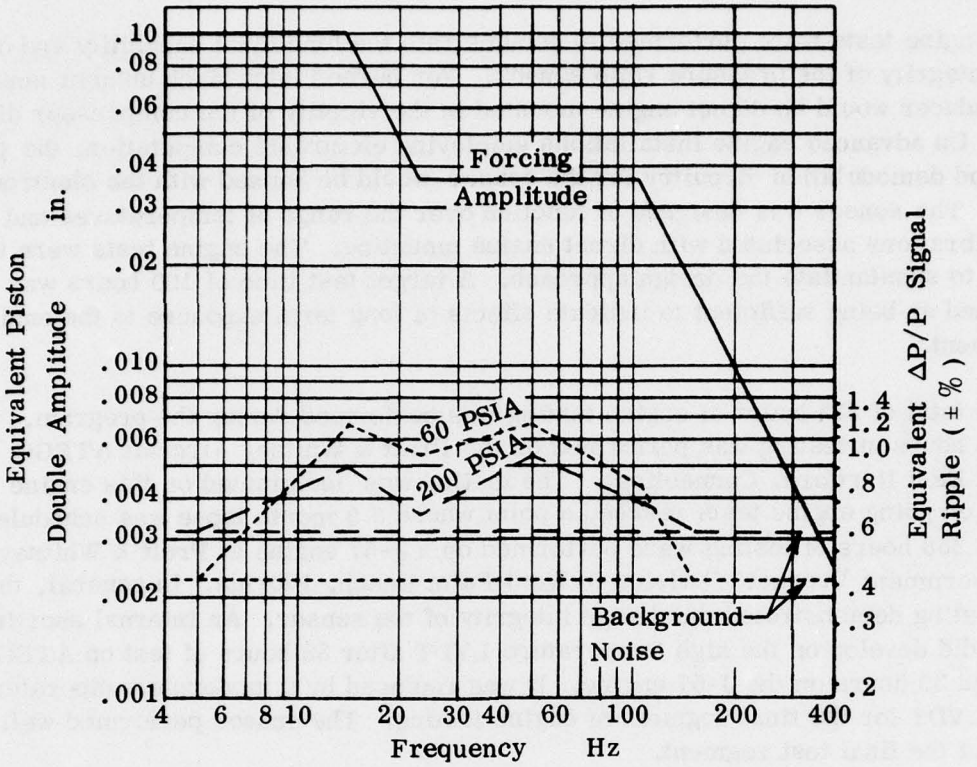

Figure 36 Vibration Effects (MIL-STD-810C Engine Mounted Equipment) P_t = 60 psia and 200 psia.

these figures are up to about 18% for 60 psia and 15% for 200 psia. At higher frequencies it is estimated that the snubbing action of the laminar restrictors formed at the piston ends, takes over from the closed loop action to reduce vibration effect.

If the sensor is mounted with its piston axis parallel to the engine axis, the vibration component parallel to the piston will be small enough to have little or no effect. Note that the sensor's closed loop behavior also demonstrates its ability to handle maneuvering "g's"

ENGINE TESTS

Engine tests were performed to demonstrate the functional capability and operational integrity of the pressure ratio sensor. For burner inlet Mach number sensing, the transducer would be direct engine mounted in the vicinity of the compressor discharge. On advanced engine installations employing electronic computation, the power supply and demodulation circuitry for the sensor would be housed with the electronic control. The sensor was designed to function over the range of temperatures and engine vibrations associated with direct engine mounting. The engine tests were thus intended to substantiate the design approach. A target test time of 100 hours was established as being sufficient to indicate effects of long term exposure to the engine environment.

A total of 313 hours of engine testing was performed during the program. The initial 55 hours of testing was performed on the Pratt & Whitney Aircraft ATEGG engine at East Hartford, Connecticut. The testing was terminated on this engine when the on going engine tests reached a point where a 9 month lapse was scheduled. The final 258 hours of testing were performed on a J-57 engine at Pratt & Whitney Aircraft Government Products Division in West Palm Beach, Florida. In general, the engine testing demonstrated the design integrity of the sensor. An internal shorting problem did develop on the high temperature LVDT after 55 hours of test on ATEGG engine and 30 hours on the J-57 engine. It was replaced by a moderate temperature (450°F) LVDT for the final segment of engine testing. The sensor performed well throughout the final test segment.

Detailed descriptions of the engine test program are contained in the following subsections. Engine installations, test results and post test analyses are described.

ATEGG Engine Tests - P&WA East Hartford Connecticut

All testing was performed in a sea level test cell. The sensor was mounted on the ATEGG engine in the vicinity of the compressor discharge as shown in Figure 37. For this series of tests, air could not be bled from the engine for the sensor, so high pressure facility air was used. A bleed down circuit manifold was used to generate a static pressure as a fixed fraction of total pressure. The fraction was selected to produce a $\Delta P/P_{t4}$ of approximately .075, which is nominally mid range for the sensor. Below about P_{t4} = 50 psia, unchoking causes variation in simulated $\Delta P/P_{t4}$. Thus for each shut down and re-start, the sensor produces a corresponding variation from its nominally fixed output indication.

The sensor was instrumented to record the input total and static pressures and the axial and radial vibration. The power supply and demodulator circuits were housed in an electronic test module which was mounted via vibration isolators to the engine hardback as shown in Figure 38. The remote digital readout module, Figure 39, provides a continuous display of output voltage of the sensor. This output was periodically monitored by P&WA test personnel to ensure functioning of the sensor.

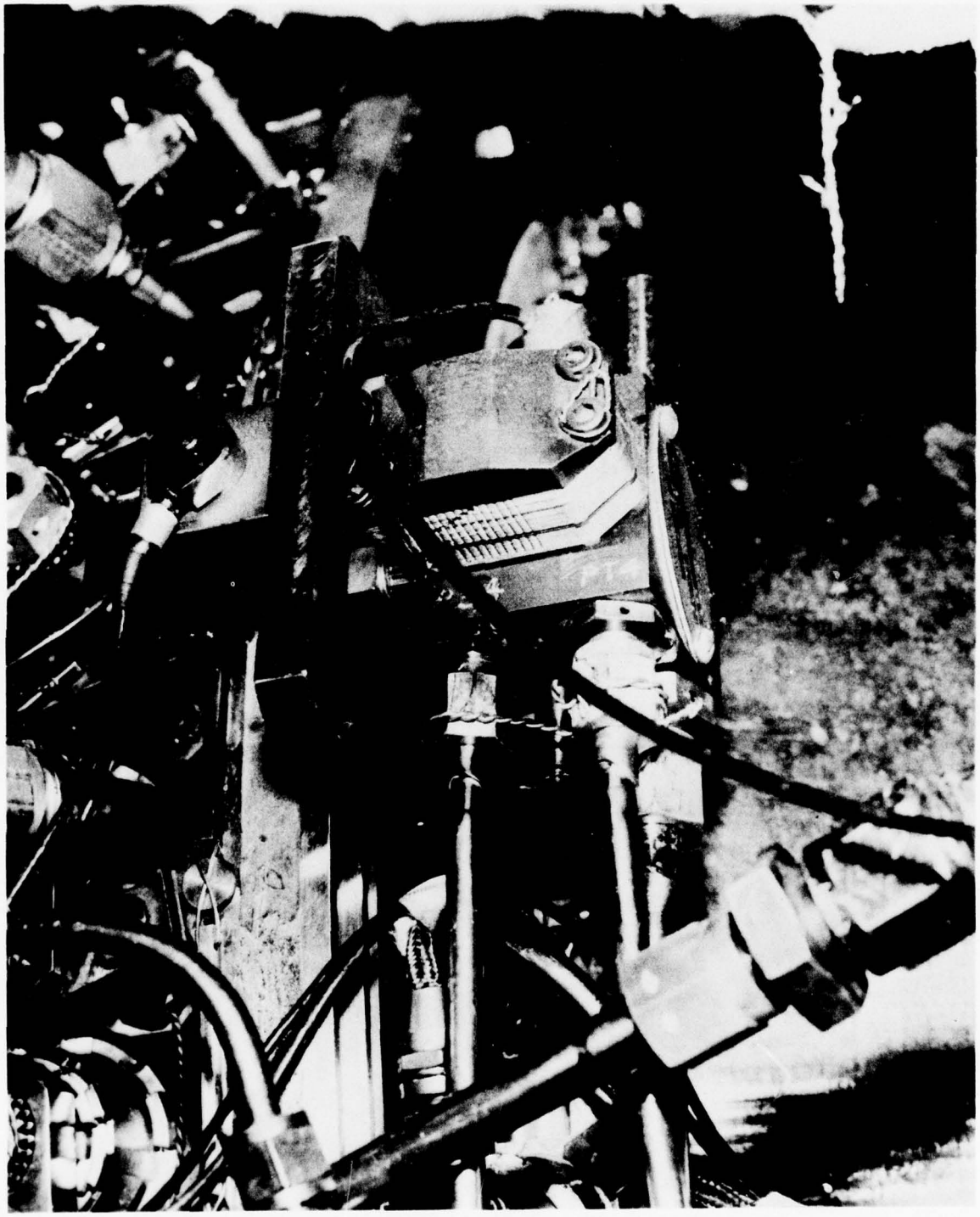

Figure 37 PRA-A3 Sensor Installed on P&WA ATEGG Engine

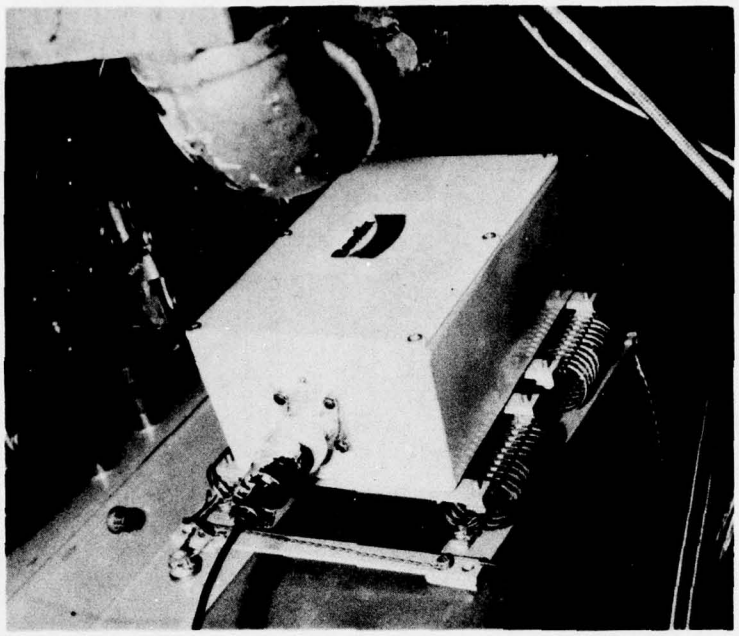

Figure 38 Electronic Test Module Mounted on the Test Cell Hardback for the ATEGG Engine

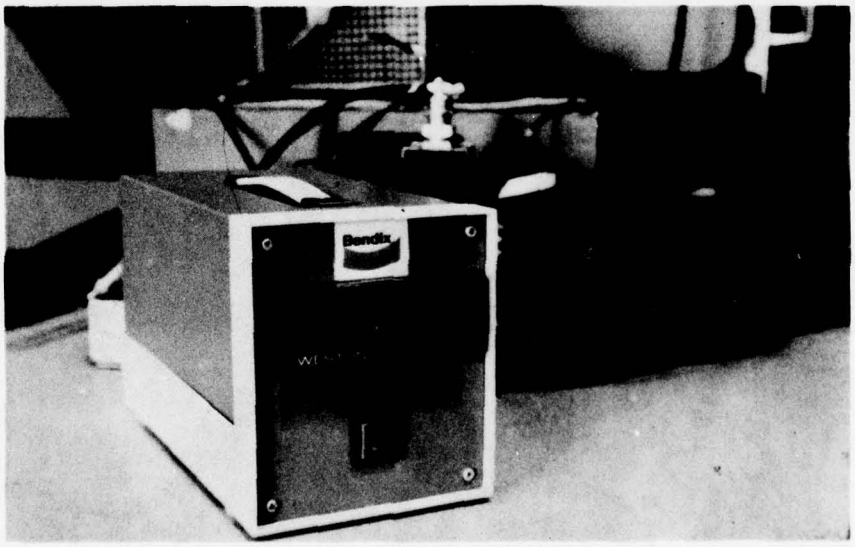

Figure 39 Digital Voltmeter for Indicating Sensor Output (VDC) in the Test Cell Control Room

The data recordings indicated that the sensor remained operational throughout the 55 hours of engine testing over an elapsed time of about one year. The sensor was removed from the engine and returned to Bendix when the on going engine test phase was completed.

The next series of engine testing was scheduled to begin 9 months later, so alternate engine test possibilities were considered in order to expedite the program.

Post Test Analysis - ATEGG Engine Tests The calibration of the sensor was rechecked when received at Bendix following the 55 hours of engine tests. This check showed that the output voltage had shifted upward by 4% as a result of the engine testing. Gasket leakage at the fluidic manifold and amplifier interfaces was observed. Replacement of the gaskets and refinishing of sealing surfaces reduced the leakage to an insignificant level but did not correct the setting shift. The unit was completely disassembled and inspected. The following items were noted :

1. Removal and inspection of the sensor piston showed slight wear (about the depth of the surface roughness pattern). See Figure 40. The rotational character of the wear shows that the piston was spinning and therefore was largely supported on its air bearings. Scuff marks could be from small particles passing through, or from occasional bottoming on high points or burrs in the sleeve. Note that both piston and sleeve are of titanium at about Rockwell 15-20 C hardness.

2. The P_B inlet screen was clean.

3. A small piece of dirt on the end flat of the primary bleed circuit A_1 adjusting screw.

4. A small piece of dirt was found deep in the piston sleeve bore.

5. Cyclone inlet parts were dirty and wet with light oil.

6. Oil and some fine dirt appeared to have leaked through the clearance regions at the ends of the 20 μ and 10 μ barrier screens surrounding the cyclone tube, but the screens were essentially clean and dry.

7. Oil and fine dirt were present on the ejector nozzle and seal ring.

8. The A_1 adjusting screw did not have the specified Everlube treatment (FI-1231) and was badly worn by the mid grip Rosan thread insert. Holding torque was less than one in. oz.

It was concluded that the most likely reason for the setting shift was movement of the loose A_1 adjustment screw due to engine vibrations. This adjustment has a very high gain and is thus very sensitive to the slightest movement. Dirt in the computing circuit restrictors could also contribute to the shift.

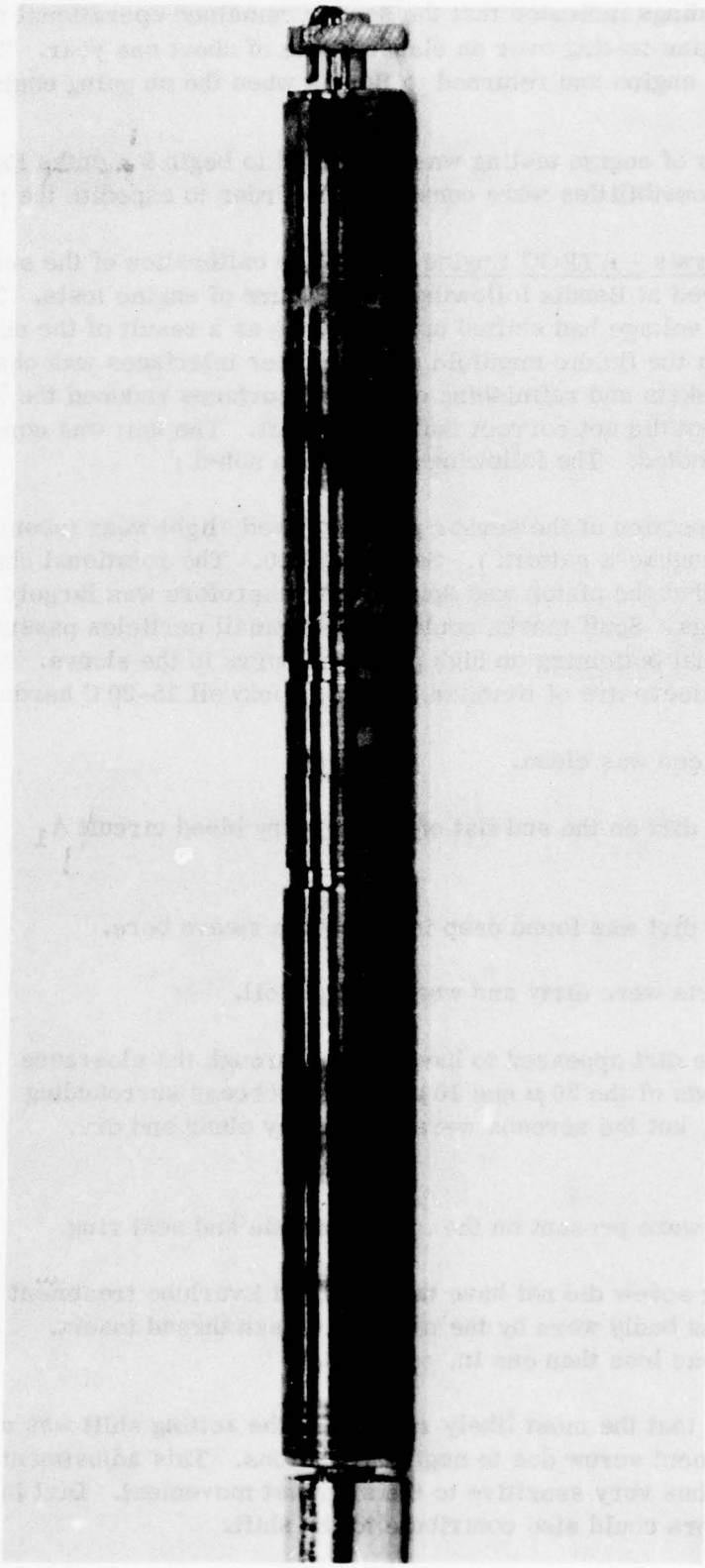

Figure 40 Enlarged View of the Piston Assembly After ATEGG Engine Running

The piston wear observed was very slight and not serious enough to affect performance. The large dirt particles found were probably in body crevices at assembly and migrated to areas at which they were found under the influence of vibration and flow forces. The filtration system should not have admitted particles as large as those found. The built-in dirt could also have caused the piston wear. Body cleaning procedures will have to be improved for future programs. The filtration system appeared to be very effective.

Air leakage around the copper fluidic gaskets was probably caused by deformation of the gaskets with prolonged vibration and cyclic temperature conditions. In a production version the fluidic inferfaces would be diffusion bonded to form a monolythic assembly in order to avoid such leakage problems.

After inspection, the parts were thoroughly cleaned, a new A_1 adjusting screw with the proper coating was installed and the unit was assembled and recalibrated.

Conclusions - ATEGG Engine Tests The engine testing of the sensor was judged to be a qualified success, in that even though a 4% shift is unacceptable, the cause and/or causes were clearly of a quality nature. The sensor concept and the design appear to be sound.

J-57 Engine Tests - P&WA, West Palm Beach Florida

All testing was performed in a fixed outside engine installation. The unit was engine mounted with air for the unit tapped off of the compressor discharge. The bleed down circuit was again used which produced a constant $\Delta P/P_t$ input to the sensor of approximately .075. A total of 258 hours on engine running running time was accumulated over a six month elapsed time. The running included engine accelerations, decelerations, steady state, starts and shut downs. The following data was recorded at intervals that averaged less than an hour thoughout the engine test program:

P_t	Total pressure
$(P_t - P_s)$	Total minus static pressure differental
$(P_t - P_s) / P_t$	Sensor digital readout
P_B	Compressor discharge pressure
T_{t4}	Compressor discharge temperature
T_{sen}	Sensor skin temperature
Axial G's	Sensor axial G level
Radial G's	Sensor radial G level
N_2	Rotor speed
TRT	Total run time

Test History - J-57 Engine Tests A chronological history of the sensor testing is as follows:

Initial operation	6-27-77	0 hours
Sensor Low reading	7-6-77	30 hours
Sensor returned to Bendix	7-14-77	33 hours
Sensor test resumption	9-2-77	0 hours
Sensor field repair	10-5-77	60 hours
End of test	11-11-77	225 hours

The sensor operated satisfactorly for the first 30 hours of engine testing but then indicated a much lower than normal output voltage reading. It was returned to Bendix where a bad connection on the high temperature LVDT cable was discovered and repaired. Bench testing showed the unit to be back in calibration after the repair so the sensor was returned to P&WA for resumption of engine testing. When installed on the engine, it again gave a low faulty output. On October 4th the sensor was checked on the engine by Bendix electronic personnel and it was found that the LVDT had an internal short. The high temperature LVDT was replaced with a moderate temperature (450°F) LVDT and engine testing again resumed on October 5th. The final 165 hours of engine test data indicated good performance of the sensor with the substituted LVDT. In evaluating contamination effects and vibration effects on all but the LVDT the total engine running time of 258 hrs is valid.

Test Data - J-57 Engine Tests The operational and environmental conditions imposed on the sensor during the 258 hours are as follows:

P_t Pressure - 60 psia Typical

$(P_t - P_s)$ Differential Pressure - 5.0 psid Typical

T_{t4} Temperature - 480°F Typical with peaks to 550 °F

T_{sensor} Temperature- 240 to 360 °F Typical wtih peaks to 404°F

Axial G's - 15 to 25 Typical with peaks to 55

Radial G's - 30 to 50 Typical with peaks to 82

The resolution of the P_t and $(P_t - P_s)$ gauges was insufficient to accurately indicate small shifts in the sensor setting during engine tests.

Within the resolution limits of these gauges, the test data indicated no shifts during the first 30 hours and the final 165 hours of engine running. The drastic shift (about 60%) in sensor output voltage that was experienced at the 60 hour total run was determined to be due to an internal short in the high temperature LVDT.

Post Test Analysis - J-57 Engine Tests The calibration of the sensor was rechecked when received at Bendix following the 258 hours of engine test. Stop to stop output voltage range for the 450°F LVDT coil is 2.97 as compared to 4.41 VDC for

the 750°F LVDT. Figure 41 shows LVDT output(in % of stop to stop VDC range) vs P_t level with the sensor connected to the bleed down circuit manifold for simulating P_s. Curves are shown for the sensor as last shipped to Pratt and Whitney Aircraft in West Palm Beach with the high temperature LVDT coil, and as received back with the low temperature coil. The difference between the curves is considered to be within the range of instrumentation and coil linearity error, and not significant. Note that curves are for sea level conditions.

Tear down and inspection showed the following :

1. There was no evidence of plugging of any screens. The 10 μ and 20 μ screen assemblies were clean and dry. See Figure 42.

2. The restrictors were all clean.

3. The piston moved freely over its full stroke.

4. A thin carbonaceous film was deposited on the piston in the A_2 nozzle (cone) region and in the region of the air bearing high pressure orifices. This carbon material apparently was carried to these regions by the engine air. Slight scuffing of the piston surface was evident. These changes were only apparent visually (See Figure 43), there being no detectable dimensional surface change.

5. No deposit or scuffing could be detected in the piston sleeve bore. See Figure 44. Note that the sleeve annuli are visible.

6. One spot on the cyclone body flange was slightly damp with a thin transparent oil film See Figure 45 at about 9:30 to 11:30 positions.

7. A thin oxide coating tended to cement close clearance parts together in a number of places:

   a). About 5 to 10 lbs force was needed to unstick the screen pressure drop relief valve from its seat. (Equivalent to 40 to 80 psi screen pressure drop).

   b). The screens were stuck at their pilot (and sealing) diameters and difficult to remove without damage.

8. The ejector diffuser required high torque to remove. The threads seized about half way out - causing the remaining threads to strip on subsequent extraction.

Figures 46 and 47 show the restrictor shim plate, the amplifier and the manifold with their gaskets and the body top flange as they appeared at disassembly.

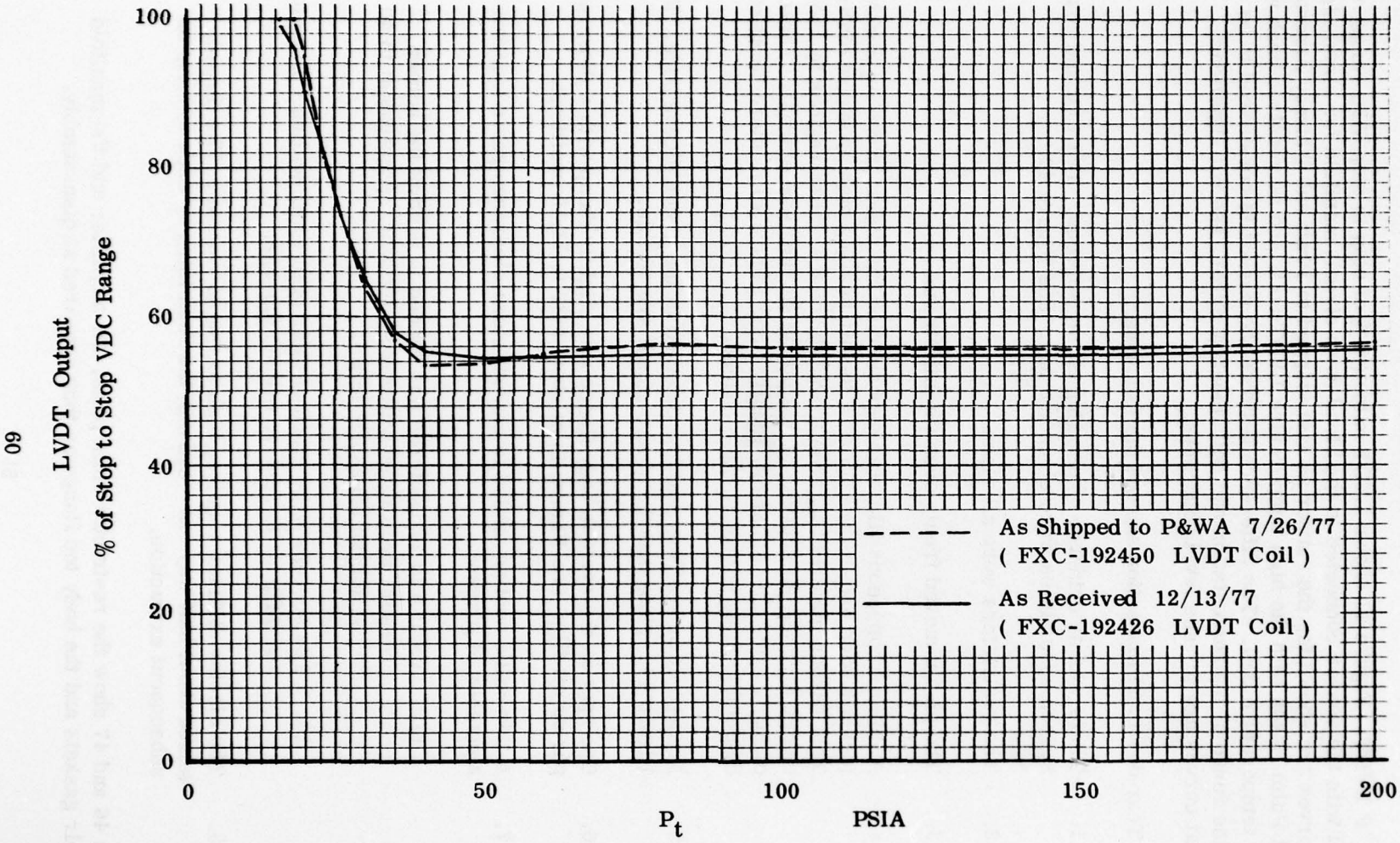

Figure 41 Sensor Output vs P_t with Bleed Down Circuit Manifold

Figure 42 The Screens after Operation on the J-57 Engine

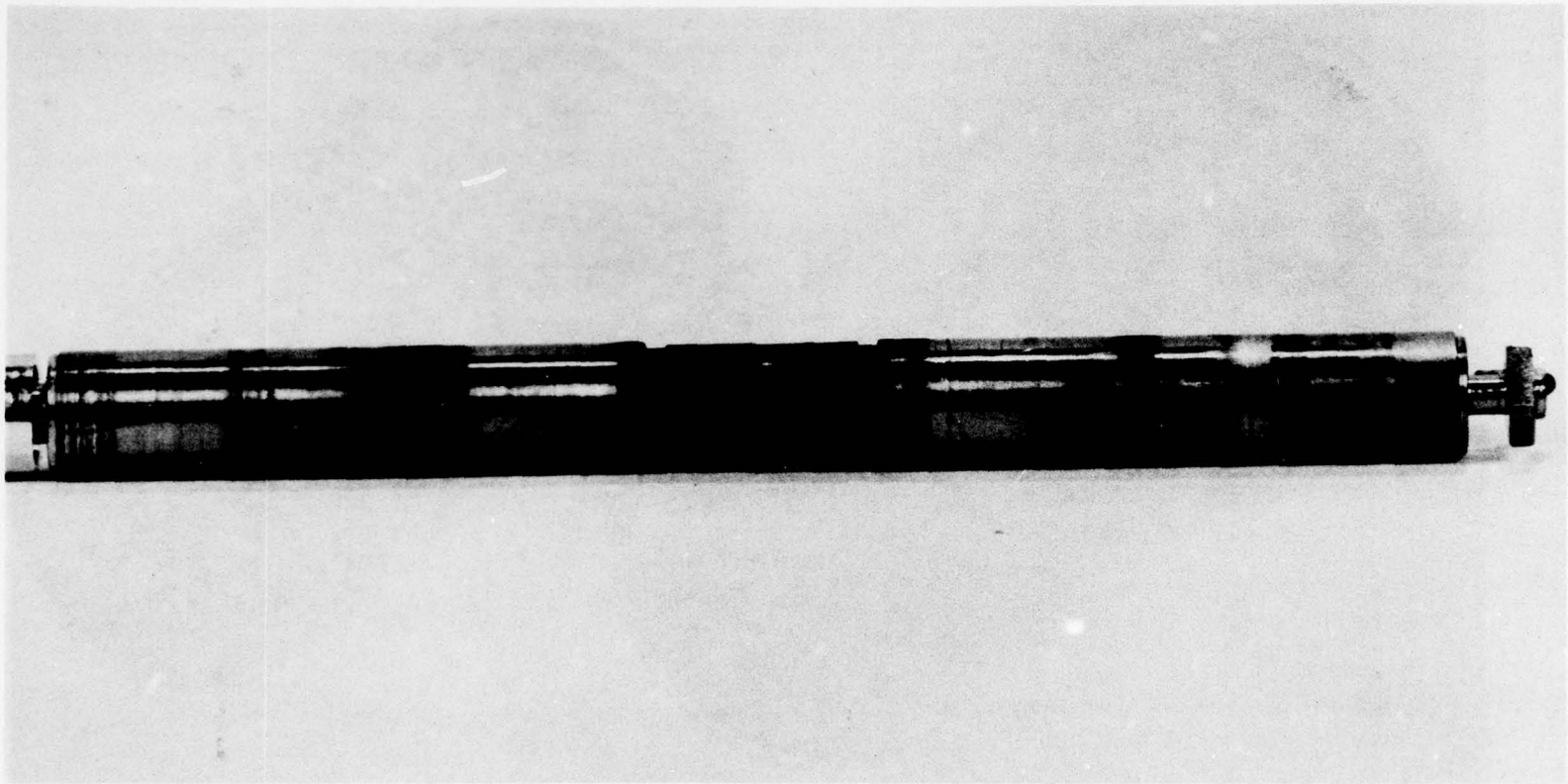

Figure 43 The Piston after Operation on the J-57 Engine

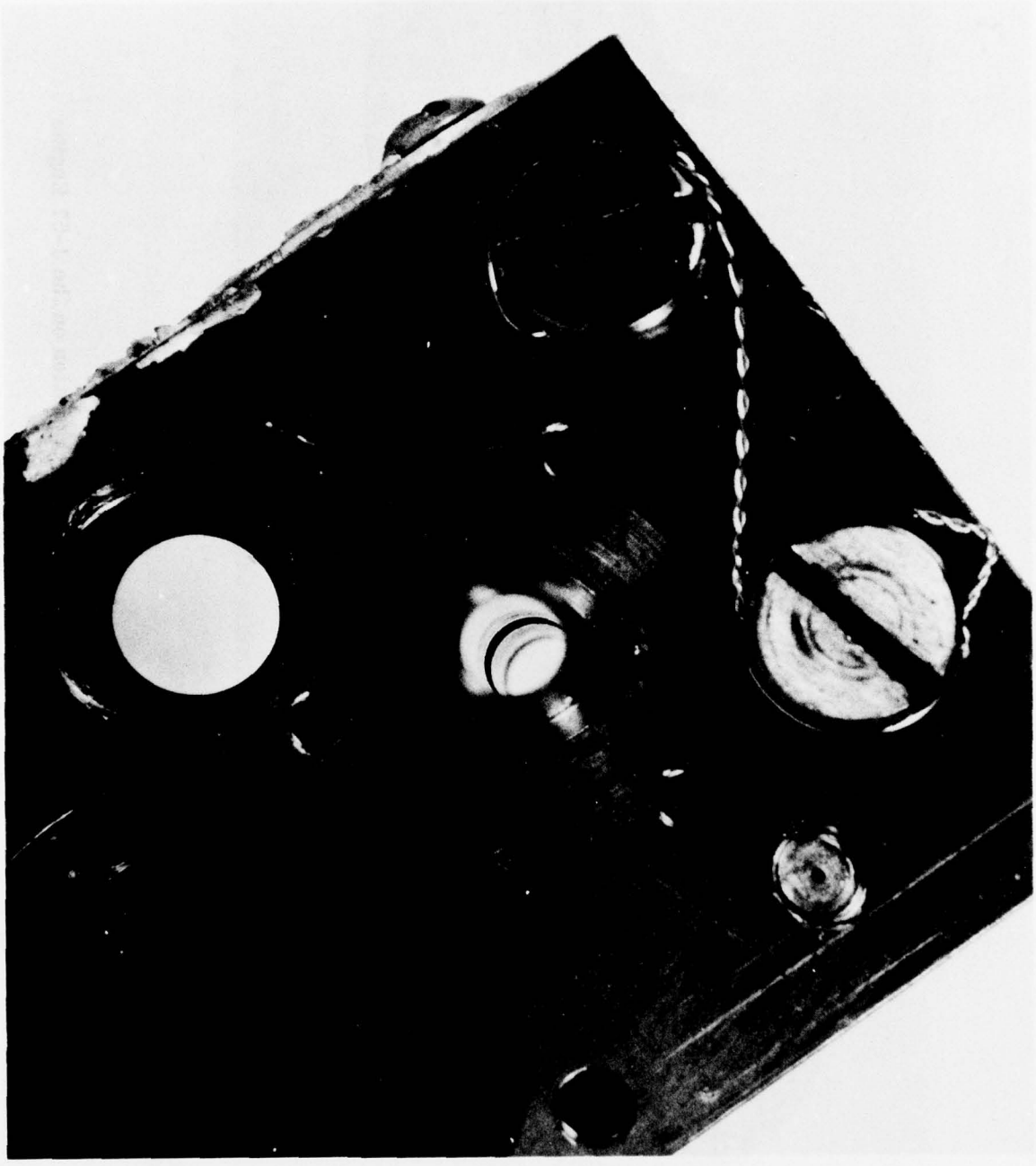

Figure 44 The Piston Sleeve Bore after Operation on the J-57 Engine

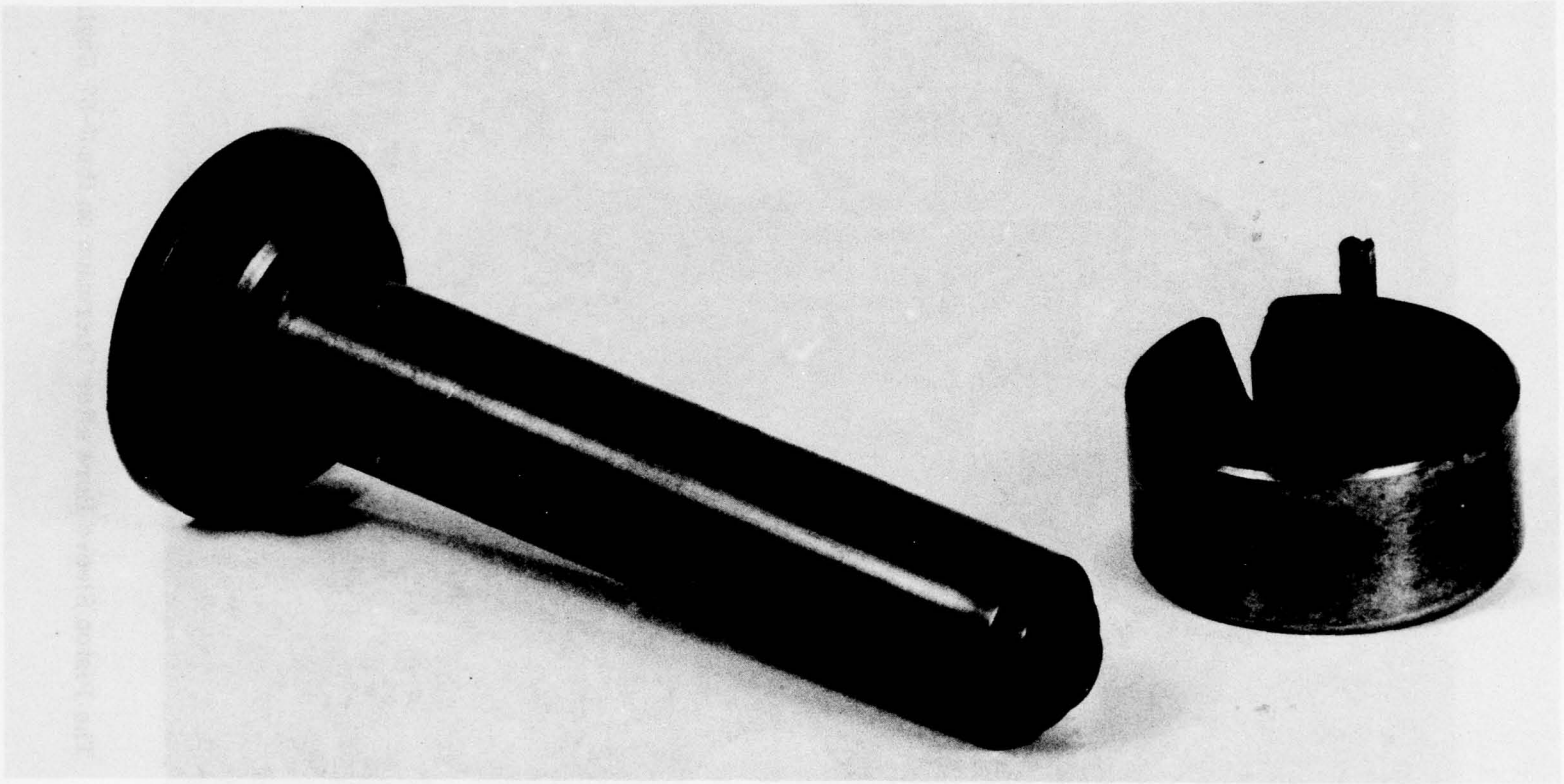

Figure 45 The Cyclone Chamber and Nozzle after Operation on the J-57 Engine

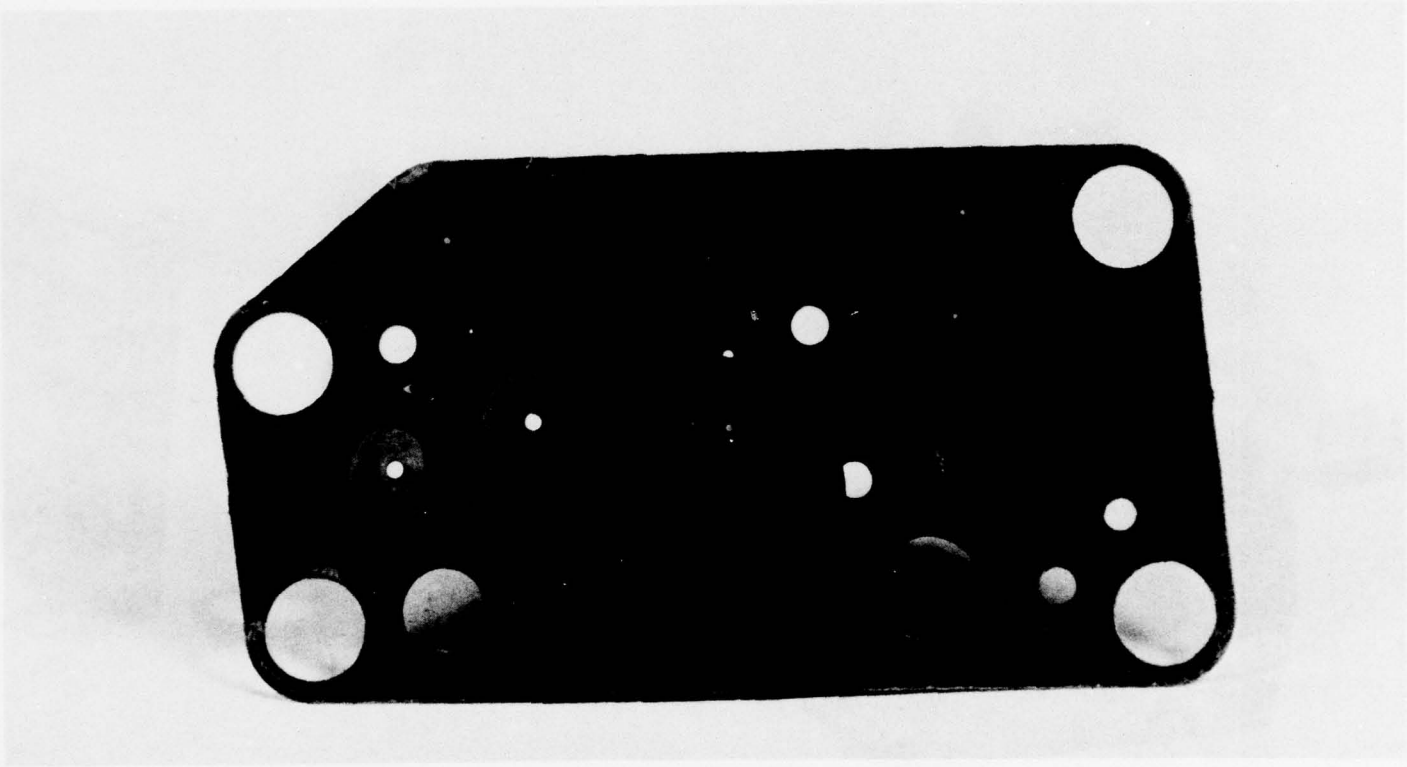

Figure 46 The Restrictor Shim Plate after Operation on the J-57 Engine

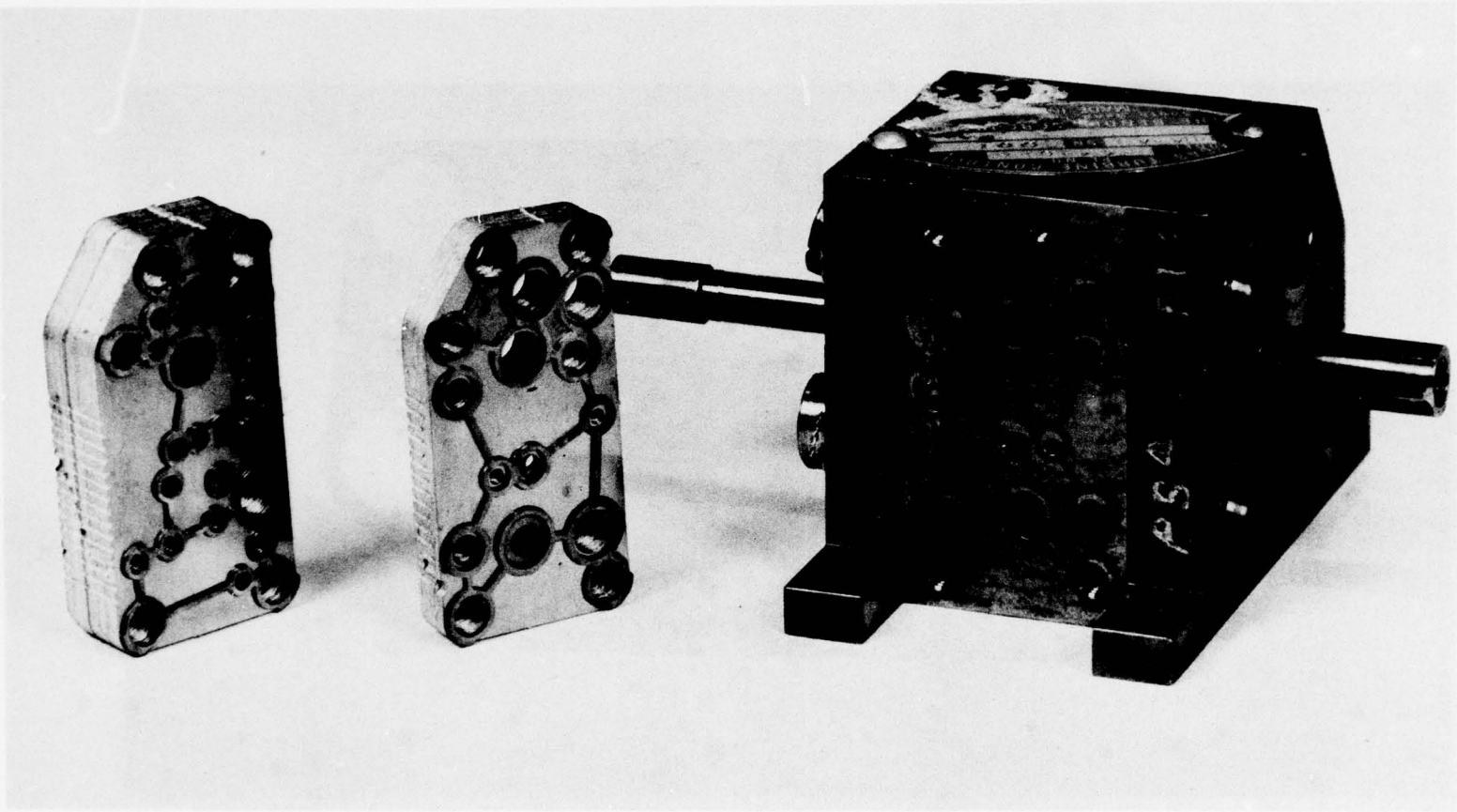

Figure 47 The Amplifier, Manifold, and Body Assemblies after Operation on the J-57 Engine

Conclusions - J-57 Engine Tests It is concluded that except for the LVDT failure, the entire sensor assembly functioned continuously with essentially no setting change for the 258 operating engine hours and that it would have continued to operate satisfactorily for many additional hours. Special surface treatments (e.g., chrome flash) should prevent seizing of faying titanium and stainless steel surfaces and reduce piston scuffing.

FAILURE ANALYSIS, LVDT COILS

A total of four LVDT coil failures were experienced during either bench temperature testing or engine testing. The first three coils, serial numbers 0001, 0002, 0003 had been fabricated using winding insulation rated to 1000° F and bobbin insulation rated to 1100° F. The fourth coil S/N 0010 had the same winding insulation but a new bobbin insulation rated to 1400° F.

Serial numbers 0001 and 0003 failed during bench testing to 700° F. S/N 0002 survived bench testing to 700° F but failed after 55 hours of engine testing on the ATEGG engine followed by 60 hours testing on the J-57 engine. S/N 0010 failed following bench testing to 800° F.

A failure analysis was performed by the coil manufacturer, Pickering and Co., on three of the coils, serial numbers 0002, 0003 and 0010. The winding insulation was found to have failed on serial numbers 0002 and 0010. The bobbin insulation on these two coils were found to be in good condition. On S/N 0003 the bobbin insulation had failed and the winding insulation was in good condition.

In summary, two 1000° F windings failed -- one at 800° F, and the other after 700° F plus extensive bench and engine testing. Another 1000° F winding survived 700° F. One 1100° F bobbin failed at 700° F. Another 1100° F bobbin survived 700° F plus bench and engine testing. A 1400° F bobbin survived 800° F.

It is concluded that the winding and bobbin insulations cannot be consistently relied on to hold up at temperatures even several hundred degrees below their rated values. This may be due to inconsistent quality and/or over-rating of these materials by their suppliers. The bobbin insulation was supplied by the Ceramco Corp. and the winding insulation by Gulton Industries.

The rating of the winding wire can be increased to 1200° F by use of a stainless steel clad copper or nickel clad silver with appropriate ceramic coating. This 1200° F rated winding with the 1400° F rated bobbin insulation should provide LVDT capabilities to 800° F. Temperature testing of the winding and bobbin materials to 900° F or 1000° F should be accomplished prior to any future coil fabrication.

CONCLUSIONS

Bench tests demonstrated that the sensor operates satisfactorily over the full range of operating pressures, temperatures and vibration except that the LVDT coil limited the maximum test temperature to 675°F instead of 750°F. Dynamic response exceeds requirements for closed loop engine control. It was indicated that accuracy to the desired ±1% of point could be acquired with a modest programmed electronic compensation of the output signal as a function of temperature and pressure. Engine tests showed a stable setting for over 250 operating hours with no appreciable piston wear or dirt in the flow circuits. The cyclone did an effective job of protecting the fine screens and the flow circuits. It appears that many more uninterrupted hours of satisfactory operation could have been attained. The program was marred by repeated failure of the high temperature LVDT coil. It is probable that changing to materials having higher rated temperatures for the windings and for the bobbin insulation will correct this. The sensor otherwise proved to be a highly reliable and rugged device able to meet the requirements for direct engine mounting on advanced high performance gas turbine engines.

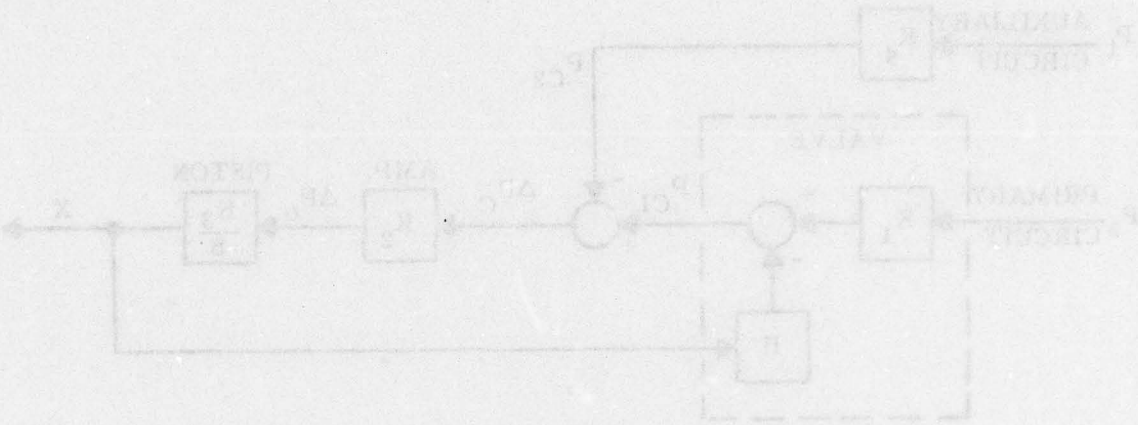

APPENDIX

DYNAMIC DESIGN ANALYSIS

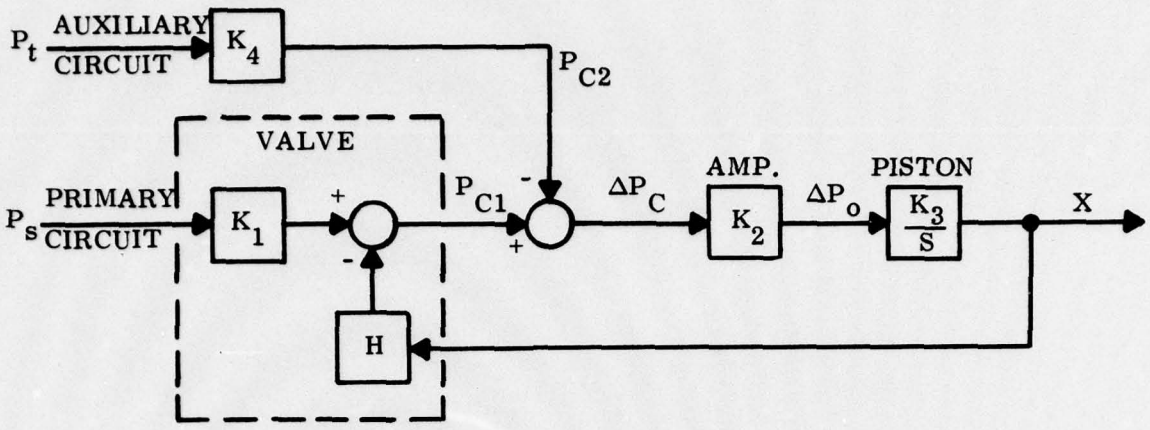

Figure 48 Dynamic Block Diagram

Selection of the Piston Diameter

From the approximate block diagram of Figure A-1, the transfer functions are:

$$\frac{X}{P_s}(S) = \frac{K_1}{H}\left(\frac{1}{1 + \frac{S}{K_2K_3H}}\right) = \frac{K_1}{H}\left(\frac{1}{1 + \tau S}\right)$$

and

$$\frac{X}{P_t}(S) = \frac{K_4}{H}\left(\frac{1}{1 + \frac{S}{K_2K_3H}}\right) = \frac{K_4}{H}\left(\frac{1}{1 + \tau S}\right)$$

Where: Kl and H are primary bleed circuit linearized constants having different values for different steady state conditions, and K4 is defined by the auxiliary circuit characteristic.

From these equations, the closed loop response time constant is:

$\tau = 1/K2K3H$

The computing flow circuit, amplifier, and piston response lags are all assumed to be negligible relative to τ. To give this assumption the greatest validity, these elements should be made as small as feasible, since their response times vary with size. By using a very small light piston and air bearings, ΔPo may be kept very small, enhancing accuracy, and minimizing compressibility effect.

It is a design objective to have the sensor response good to 30 Hz (at the 3db attenuation condition). The equivalant loop response time constant is $\tau = 1/30(2\pi)$ =. 0053 sec. If the sensor output is too noisy with this fast response, it may be filtered electronically.

The piston diameter will be calculated from the equation for τ using parameter values for mean operating conditions.

Assume:

τ = 0053 second = Loop Time Constant
Pt = 200 psia
T = 200°F
$\Delta P/Pt$ range = 05 to . 10 (or . 075 mean)
K4 = . 8 = auxiliary computing circuit characteristic
K2 = 8 = Amplifier pressure gain
Piston net stroke = Piston diameter D
L = 5D = Laminar restrictor length (2 1/2 D effective at each end of the piston.)

For null balance, $K_1 = K_4/(Ps/Pt) = .8/.925 = .865$

Loop Gain = $1/\tau = 188.7$ second$^{-1} = K_2K_3H$
Full valve stroke changes P_{C1} by H = 200 (. 10 - . 05)(. 865) = 8. 65 psi
Then K2H = 8(8. 65) = 69. 2 psi/stroke
And $K3 = 1/\tau K2H = 1/.0053(69.2) = 2.727$ piston strokes/sec.-psi

The value of K_3 is essentially established by the total laminar restrictor length imposed between the piston ends and the piston pressure supply annuli. The radial clearance is . 001 (the same as for the air bearing).

Now:

$$Q = \frac{\Delta P_o b^3 c}{12 \mu L}$$

Where:

ΔP_o = net amplifier pressure differential output, psi.
Q = piston displacement rate in^3/sec.
b = radial piston clearance = . 001 in.
c = piston circumference = π D in.
μ = absolute viscosity = 3. 65 (10)$^{-9}$ Lb_{wt}-sec/in.^{2} @ 200°F
L = net laminar restrictor length, ins.

The piston displacement is $D(\pi D^2/4) = \pi D^3/4$ in.^{3}
Then $Q = K_3 \Delta P_o \pi D^3/4$ and from the above equation:

$$K3\pi D^3/4 = \frac{b^3 c}{12 \mu L}$$

or

$$D = \sqrt[3]{\frac{4b^3c}{12\mu LK_3\pi}} = \sqrt[3]{\frac{4(.001)^3\pi D}{12(3.12 \times 10^{-9})(5D)(2.727\pi)}}$$

and

$D = .199$ in. Piston Diameter

This computation is based on simplified assumptions and linearizations, but provides a rationale for the preliminary choice of piston diameter. Tests have shown the choice to be a good one.

The Piston as a Sprung Mass

Consider the effect of compressibility in the piston chambers on the piston response. Looking at one end of the piston:

$$PV^k = Constant = P_oV_o^k \text{ and } P = P_oV_o^kV^{-k}$$

Then:

$$\frac{dP}{dV} = -k\,P_o\,V_o^k V^{-(k+1)}$$

and:

$$\frac{dF}{dX} = \frac{AdP}{dV/A} = A^2\frac{dP}{dV} = kA^2P_oV_o^k\,V^{-(k+1)}$$

Assume:

$P_o = .6Pt = 120$ psia

$V_o = 1.33$ times piston displacement

$= 1.33\,\pi\,D^3/4$

$V = V_o$

$k = 1.4$ (adiabatic specific heat ratio)

The piston is 15 diameters long and made of titanium with 50% of its cross section hollowed out. Then from the above:

$$\frac{dF}{dX} = -1.4\,(\pi D^2/4)^2\,P_o(1.33\pi D^3/4)^{1.4}\,(1.33\pi D^3/4)^{-2.4} = -.825DPo$$

$$= -.825\,(.199)(120) = 19.7 \text{ lb./in.}$$

Net pnumatic spring rate for both piston ends is then:

$$2(19.7) = 39.4 \text{ lb./in.}$$

The piston mass is:

$$m = \pi/4\,(.199)^2(15)(.199)(.16)(.5)/386 = 1.924\text{x}10^{-5} \text{ lb. sec}^2/\text{in.}$$

Noting that the piston stroke equals its diameter, viscous force on the piston is:

$$(\pi D^2/4)\ (\dot{X}/K_3 D) = \frac{\pi\ (.199)}{4\ (3.08)}\ \dot{X} = .0507\ \dot{X}$$

Then:

$$(1.924 \times 10^{-5})\ \ddot{X} + .0507\ \dot{X} + 39.4\ X = 0$$

or $$\ddot{X} + 2635\ \dot{X} + 2{,}048{,}000\ X = 0$$

The natural frequency is:

$$\omega_n = \sqrt{2{,}048{,}000} = 1430 \text{ rad/sec or } 227 \text{ Hz}$$

and the damping ratio is:

$$\zeta = \frac{2635}{2(1430)} = .921$$

Though ω_n and ζ will vary with departure from the assumed mean operating condition, clearly no significant dynamic error can be expected from compressibility effect in the piston end chambers. Again, tests have verified this preliminary conclusion that piston bounciness would not cause a resonance problem in the sensor response.

REFERENCES

1. Advanced Turbine Engine Control Components, Bendix Proposal No. ECD 863-591 P

2. S. K. Grinnell and H. H. Richardson, Design Study of a Hydrostatic Gas Bearing with Inherent Orifice Compensation, Transactions of the ASME, January 1957.

3. Pavlin, Cyrille, Experimental Study of a Proportional Fluid Amplifier, Fluid Amplification Symposium, Harry Diamond Laboratories, Washington, D. C., Vol. III 1965.

☆U.S.Government Printing Office: 1978 — 757-080/468